MAGNETOM Flash

Issue Number 93 · 4/2025
ISS Edition

magnetomworld.siemens-healthineers.com

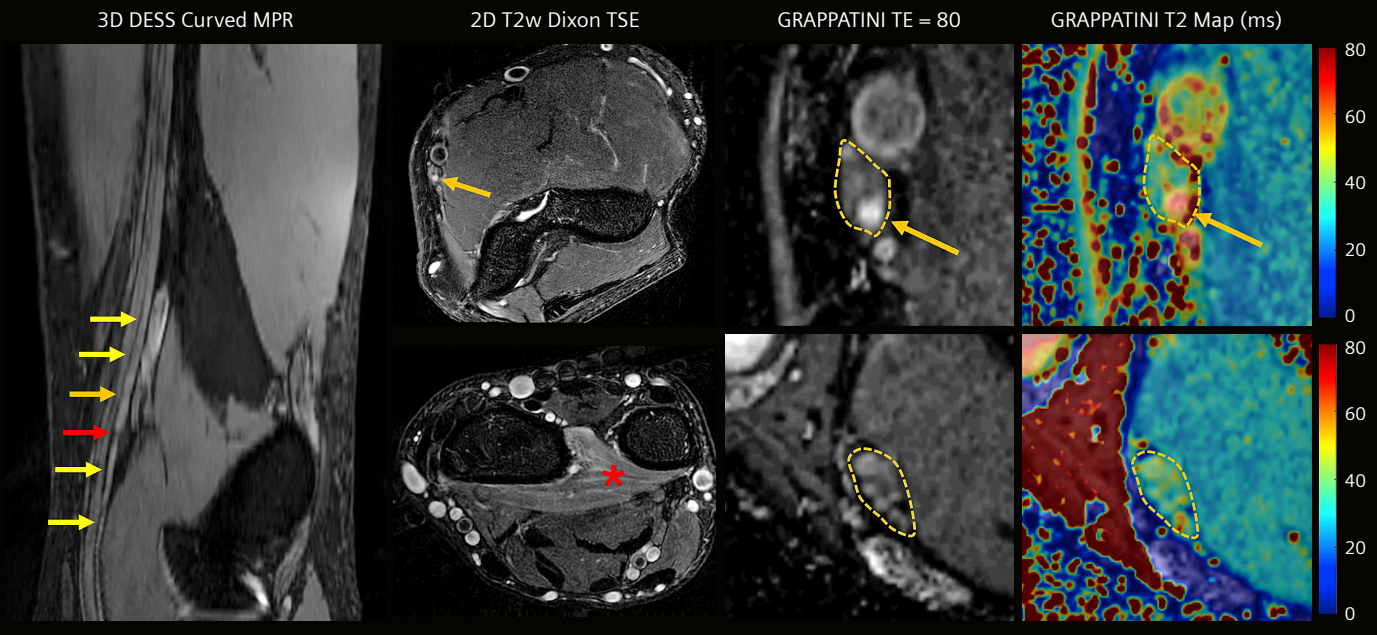

SIEMENS Healthineers

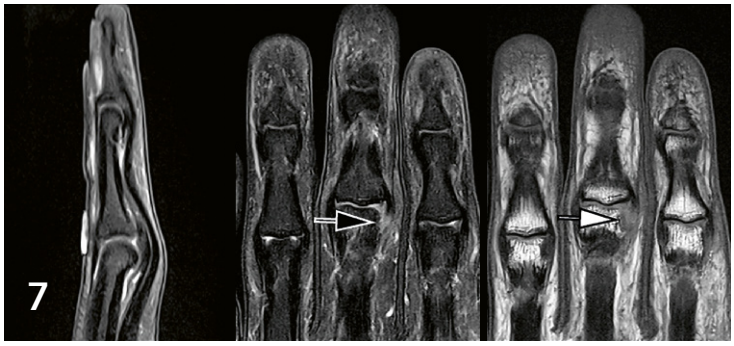

Deep learning-enhanced MSK MRI

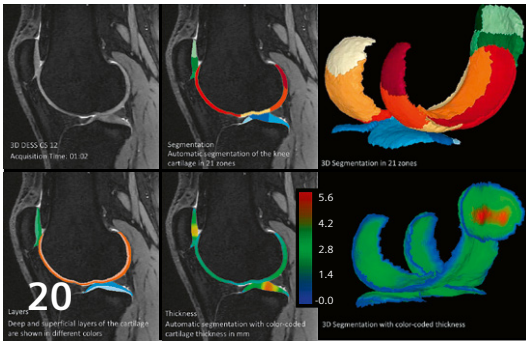

Automatic segmentation of the knee cartilage

Editorial Comment

AI / DL-based Image Reconstruction

Sports Medicine

MR Neurography

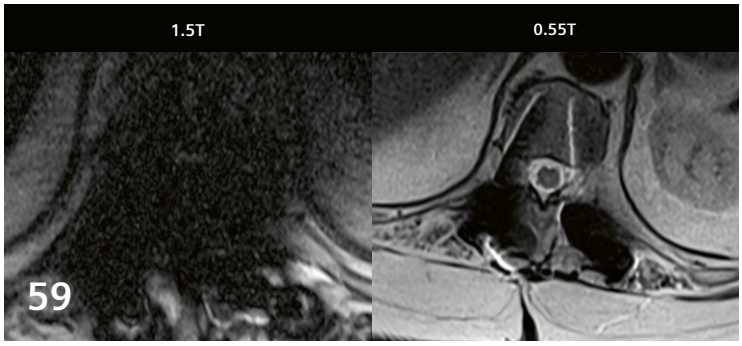

The potential of 0.55T MSK MRI

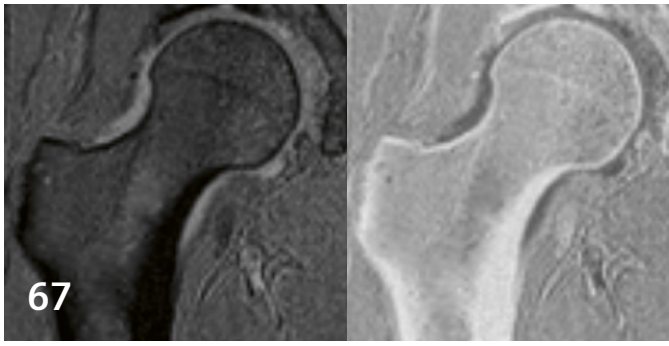

StarVIBE for bone imaging

Quantitative Imaging

Metal Implant Imaging

Bone Imaging

Meet Siemens Healthineers

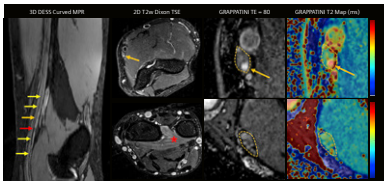

Cover images from *Exploring the T2-Mapping GRAPPATINI[1] Technique for Qualitative and Quantitative Assessment of Orthopedic and Neuromuscular Conditions* by Ek T. Tan, Darryl B. Sneag, et al. (Hospital for Special Surgery, New York, NY, USA).

[1] *Work in progress. The product is still under development and not commercially available. Its future availability cannot be ensured.*

[2] *The MRI restrictions (if any) of the metal implant must be considered prior to patient undergoing MRI exam. MR imaging of patients with metallic implants brings specific risks. However, certain implants are approved by the governing regulatory bodies to be MR conditionally safe. For such implants, the previously mentioned warning may not be applicable. Please contact the implant manufacturer for the specific conditional information. The conditions for MR safety are the responsibility of the implant manufacturer, not of Siemens Healthineers.*

Dr James Linklater OAM
MB BS (Hons), B Med Sci, DDU (1), FRANZCR
Musculoskeletal Radiologist and CEO, Castlereagh Imaging and Illawarra Radiology Group

James is a musculoskeletal radiologist working with Castlereagh Imaging since 1999 and is currently the CEO. He is a consultant radiologist for a number of professional sporting teams, has an active research program, and is director of the musculoskeletal radiology fellowship program. James has 100 publications to his name and regularly presents at national and international meetings. He has been an examiner for the Royal Australian and New Zealand College of Radiologists, is a past president of the Australasian Musculoskeletal Imaging Group, serves on the editorial board of *Sports Health*, and is an active reviewer for several journals. In 2019, he was awarded a Medal of the Order of Australia for services to medicine in the field of radiology.

The Future of Musculoskeletal MRI has Arrived

Musculoskeletal MRI stands at a remarkable inflection point, where AI, ultra-fast sequences, low-field reinvention, and 7T explorations are converging to deliver a leap in imaging capabilities that was previously unimaginable.

Welcome to the first-ever International Skeletal Society (ISS) edition of *MAGNETOM Flash*, a special issue that brings together global experts to share advances that are reshaping musculoskeletal imaging. From accelerated protocols to super-resolution AI, the innovations captured here are opening new diagnostic frontiers.

MSK MRI is moving fast. Really fast. Whether it's pushing the limits of acquisition speed, unlocking the power of ultra-high-field imaging, or harnessing AI to enhance both image quality and workflow, one thing is clear: The tools and techniques we use are evolving – and so are the questions we ask.

This special issue is your panoramic view of that evolution. It's a curated journey through what's new, what's promising, and what's possible.

We kick off with Vosshenrich and Fritz [1], who show us how "fast" doesn't have to mean "compromise." Their deep dive into the acceleration toolbox, which consists of Simultaneous Multi-Slice, Compressed Sensing, and deep learning, makes a strong case for smarter imaging that's also quicker and more comfortable for patients.

What makes this speed possible? It's not just software magic. Hardware advancements and how we leverage them matter greatly. The synergy of high-performance gradients, rapid RF pulses, and wide receiver bandwidths is reshaping the turbo spin-echo frontier. Echo-train compaction plays a pivotal role here, allowing for shorter echo spacing and longer echo trains. In turn, these enable greater acceleration utilizing a synergistic combination of parallel imaging (SENSE/GRAPPA) and simultaneous multislice acquisition (SMS) with multi-channel surface coils, allowing multiplicative acceleration benefits whilst maintaining image quality through the use of AI-based denoising (Deep Resolve). Whether at 0.55T, 1.5T, 3T, or 7T these innovations deliver scan times once thought to be unattainable, without sacrificing diagnostic value. Deep neural networks are now capable of reconstructing SMS2-PAT3, SMS3-PAT3, and even SMS3-PAT4 datasets, potentially accelerating scan protocols beyond a factor of 10. These AI-powered gains redefine our ceiling for what's achievable in routine MSK MRI.

Feuerriegel and colleagues [2] continue the momentum, documenting their validation of a diagnostically equivalent alternative to contrast-enhanced imaging for demonstrating knee joint synovitis: a deep-learning-accelerated fat-suppressed T1 FLAIR sequence[1] that

[1] *The application is currently under development and not commercially available. It is for research use only. Not for clinical use. It is not for sale in the USA and its future availability cannot be ensured.*

demonstrates synovial thickening without gadolinium, in scan times under 2 minutes, with direct application in knee osteoarthritis research and in some clinical applications. Boudabbous and team [3] give us a sneak peek at what 7T imaging could mean for MSK radiology, showing impressive improvements in image quality over lower field strengths whilst not yet demonstrating a clear use case in clinical musculoskeletal MR imaging.

Meanwhile, Hallinan and Makmur [4] selectively address a different kind of challenge: the reporting bottleneck. Their work on AI-based grading of lumbar central canal and foraminal stenosis documents its accuracy and ability to significantly reduce reporting times, particularly amongst general radiologists and trainees, whilst not yet providing a comprehensive AI tool for diagnostic assessment of MRI lumbar spine. The lumbar spine AI application[1] is now available as a research prototype on *syngo*.via Frontier.

For sports imaging fans, Kassarjian [5] shares an update on hamstring imaging that's both practical and precise, with a focus on the biceps femoris. His insights are grounded in experience and guided by anatomy, providing some important tips in reporting progress MR scans of hamstring injuries where guidance on re-tear risk is sought by the team managing the rehabilitation of the athlete.

Sneag and colleagues [6] share their experience in optimizing brachial plexus MR imaging on a 3T MAGNETOM Vida, documenting their high-resolution approach. They dispense with the traditional approach of bilateral imaging, moving instead to a dedicated multi-coil, unilateral approach, harnessing prospective respiratory gating to minimize respiratory artifact. The use of optimally angled oblique sagittal respiratory-gated 2D Dixon fat-suppressed T2 sequencing affords high signal-to-noise ratio, high in-plane spatial resolution, and anatomic imaging of the individual constituents of the brachial plexus, providing evaluation of individual nerve fascicle signal and morphology. Constrained field of view volumetric SPACE STIR sequencing, optimally angled for unilateral plexus imaging provides higher through-plane spatial resolution imaging of the plexus, with specific modifications including: a C-shaped frequency offset corrected inversion (C-FOCI) pulse to provide more uniform fat suppression; a variable flip angle echo train tailored to B_1 inhomogeneity; and a deep-learning-based 3D reconstruction algorithm[1] tailored for CAIPIRINHA sampling, allowing reduction of slice thickness from 1 mm to 0.8 mm. Selective use of IV contrast to improve vascular suppression reduces venous contamination obscuration of small branch nerves of the plexus and allows oblique or curved multi-planar reconstructions along individual nerves of interest. The authors elegantly present the utility of this approach by demonstrating fibrous constrictions in the suprascapular nerve in a patient with Parsonage-Turner syndrome.

Quantitative imaging in routine clinical musculoskeletal MRI has historically imposed significant acquisition and post processing time constraints, limiting its uptake in clinical practice. In their article, Tan, Lu, and Sneag present a compelling overview of GRAPPATINI[1], a hybrid acceleration technique that integrates GRAPPA and MARTINI, offering the potential for fast, high-resolution T2 mapping in musculoskeletal and neuromuscular MRI. The authors detail its dual capacity to generate quantitative T2 maps alongside synthetic T2-weighted images within clinically feasible scan times, significantly enhancing both diagnostic efficiency and image quality. Through case-based applications in foot drop, Parsonage-Turner syndrome, lumbar disc degeneration, and cartilage imaging, they demonstate GRAPPATINI provides strong agreement with conventional techniques while offering additional biomarker quantification. These early clinical experiences underscore GRAPPATINI's potential to streamline imaging workflows and enable more precise assessment of nerve and musculoskeletal pathology, paving the way for broader adoption in both research and routine practice.

And what about patients with metal implants? Breit et al. [7] remind us that lower is sometimes better. Their work at 0.55T reveals how low-field imaging can rise to the occasion when high-field scanners fall short in imaging patients with metal[2] hardware.

Finally, Moran and Song [8, 9] describe the 3D bone imaging application of a sequence primarily designed for free-breathing body and pediatric imaging. The VIBE sequence has become a cornerstone of MR imaging of pars bone stress injuries, providing a CT-equivalent level of accuracy in demonstrating incomplete pars interarticularis stress fracture lines that would otherwise remain occult on conventional 2D spinal MR sequences. StarVIBE is a modified version of VIBE that uses radial sampling for in-plane imaging, and Cartesian sampling for through-plane imaging. The center of k-space is sampled multiple times due to the radial trajectory, making StarVIBE relatively motion-insensitive and thus of potential utility in situations where motion degradation of image quality would otherwise render a routine VIBE sequence non-diagnostic.

[2]The MRI restrictions (if any) of the metal implant must be considered prior to patient undergoing MRI exam. MR imaging of patients with metallic implants brings specific risks. However, certain implants are approved by the governing regulatory bodies to be MR conditionally safe. For such implants, the previously mentioned warning may not be applicable. Please contact the implant manufacturer for the specific conditional information. The conditions for MR safety are the responsibility of the implant manufacturer, not of Siemens Healthineers.

This issue of *MAGNETOM Flash* is a reflection of where musculoskeletal MRI is today – and, more importantly, where it is heading. It is appropriate that this edition is being published to coincide with the Annual Meeting of the International Skeletal Society – one of the leading international societies in the musculoskeletal MR imaging space. Recognition should go to the authors, the reviewers, and the team at Siemens Healthineers who made it possible.

Whether you're a radiologist, technologist, physicist, or engineer, I am sure you will find something in these pages that sparks your curiosity and propels your practice forward.

Sincerely,

Dr James Linklater, FRANZCR, OAM

University of Sydney
Castlereagh Imaging
Guest Editor
International Skeletal Society Special Edition
MAGNETOM Flash

References

1 Vosshenrich J, Fritz J. Flash Forward: Deep Learning-Enhanced Musculoskeletal MRI at the Speed of Thought. MAGNETOM Flash. 2025;93(4). On page 7 of this edition.
2 Feuerriegel GC, Goller SS, von Deuster C, Sutter R. Deep Learning-Accelerated FLAIR Imaging: A Non-Contrast Alternative for Knee Synovitis Assessment. MAGNETOM Flash. 2025;93(4). On page 16 of this edition.
3 Delattre B, Piredda GF, Klauser A, Mattera L, Garcia C, Martuzzi R, et al. Beyond Limits: Unveiling Clinical Precision in Knee Imaging with 7 Tesla MRI. MAGNETOM Flash. 2025;93(4). On page 24 of this edition.
4 Hallinan J, Ooi BC, Tan JJH, Huwer S, Hakeen SS, Schmitt B, et al. From Concept to Deployment: A Deep Learning Model for Lumbar Spinal Stenosis at National University Hospital in Singapore. MAGNETOM Flash. 2025;93(4). On page 33 of this edition.
5 Kassarjian A. Update on Imaging Hamstring Injuries with a Focus on the Biceps Femoris. MAGNETOM Flash. 2025;93(4). On page 40 of this edition.
6 Lin Y, Tan ET, Cai X, Kollasch P, Stemmer A, Nickel MD, et al. Optimizing Brachial Plexus Magnetic Resonance Neurography at 3 Tesla. MAGNETOM Flash. 2025;93(4). On page 46 of this edition.
7 Breit HC, Vosshenrich J, Clauss M, Obmann MM, Bach M, Harder D, et al. Exploring the Potential of Low-Field Musculoskeletal MRI at 0.55T: Preliminary Results in Patients with Large Metal Implants. MAGNETOM Flash. 2025;93(4). On page 59 of this edition.
8 Song E. StarVIBE for Bone Imaging. MAGNETOM Flash. 2025;93(4). On page 64 of this edition.
9 Moran E. Pictorial Essay: Clinical Application of StarVIBE for Bone Imaging. MAGNETOM Flash. 2025;93(4). On page 67 of this edition.

We appreciate your comments.
Please contact us at magnetomworld.team@siemens-healthineers.com

Editorial Board

Review Board

Flash Forward: Deep Learning-Enhanced Musculoskeletal MRI at the Speed of Thought

Jan Vosshenrich, M.D.[1,2]; Jan Fritz, M.D.[1]

[1]Department of Radiology, Grossman School of Medicine, New York University, New York, NY, USA
[2]Department of Radiology, University Hospital Basel, Switzerland

Musculoskeletal MRI represents the standard of care for the noninvasive diagnostic work-up and surveillance of a wide range of musculoskeletal conditions, offering unparalleled soft tissue contrast and anatomic detail. Over the past two decades, hardware and sequence design advancements have pushed the boundaries of image quality and diagnostic accuracy. But it is only recently that musculoskeletal MRI has entered a new era. Advanced acceleration techniques and deep learning-based image reconstruction methods have enabled us to trim minutes off lengthy image acquisition times and have redefined what is possible, much like Barry Allen gaining superhuman speed and becoming *The Flash*. Deep learning-enhanced rapid musculoskeletal MRI transforms clinical practice by providing shorter scan times, enhanced patient comfort, and better image quality than would ever be achievable with conventional MRI, while maintaining the diagnostic performance of established comprehensive imaging protocols. By exploring this evolving landscape and showcasing how these innovations can be gainfully applied in clinical practice, we aim to provide practical insights and spark excitement for this thrilling new chapter in musculoskeletal MRI.

Echo train compaction: The speed force of musculoskeletal MRI

In the race toward ultra-fast high-resolution musculoskeletal MRI, even the most advanced acceleration strategies rely on one critical foundation: a finely tuned pulse sequence. Just as *The Flash* channels the *Speed Force* to unlock his full potential, the performance of musculoskeletal MRI hinges on pulse sequence parameter optimization to maximize efficiency even before advanced acceleration techniques come into play. With meticulously designed pulse sequences, seemingly small time savings at the echo train level scale substantially through advanced acceleration techniques. Consider a modest 10-second gain from optimizing an echo train. Combined with a six-fold acceleration method, this can translate into a blazing 60-second reduction in acquisition time. Time savings further multiply with the number of acquired pulse sequences, for example, to five minutes for a five-sequence knee MRI protocol. Therefore, prepping and priming turbo spin-echo (TSE) pulse sequences like a speedster ready to sprint is key to realizing exponential speed gains.

Compact echo trains are crucial to optimizing TSE pulse sequences for peak performance. This involves configuring pulse-sequence parameters to fit the highest number of strong refocusing echoes into the shortest possible time window, minimizing image blur and maximizing signal. The shorter the echo spacing, the more echoes can be captured per unit of time. The three core elements enabling this compression are fast radiofrequency (RF) pulses, high-performance gradients, and high receiver bandwidth. Though not always mentioned in commonly cited pulse-sequence time equations, these factors are the hidden forces that drive image acceleration.

Modern clinical MRI systems allow the user to select fast RF pulses that occupy less time in the echo train, thereby shortening echo spacing and accelerating image acquisition. Though these rapid RF pulses do increase the specific absorption rate (SAR), they are key to unleashing the full potential of TSE pulse sequences. The "Performance" gradient mode lets users access the strongest and fastest gradients to further expedite the completion of an echo train by minimizing temporal gaps between RF pulses. Although strong gradients can occasionally induce peripheral nerve stimulation, this is generally well tolerated during musculoskeletal MRI. Finally, high receiver bandwidth also contributes to shorter echo spacing by minimizing individual echo length. While increased bandwidth may lower the signal-to-noise ratio (SNR), it brings crucial benefits for musculoskeletal imaging, including reduced chemical shift artifacts and sharper anatomical detail. Also, signal losses are limited through earlier sampling of stronger MR signals [1].

Combining fast RF pulses, high-performance gradients, and high receiver bandwidths shrinks echo spacing, shortens repetition times, and lengthens echo trains, thereby setting the stage for multiplicative time gains with advanced acceleration techniques.

Deep learning-enhanced parallel imaging: Shattering the speed limit

Parallel imaging represents the most effective and widely adopted method to accelerate TSE pulse sequences in musculoskeletal MRI. By leveraging the spatial sensitivity profiles of multi-element receiver coils, parallel imaging enables undersampling of phase-encoding data, historically the most time-intensive component of image acquisition. Time savings result from sampling only every second, third, or fourth line in *k*-space for twofold, threefold, or fourfold acceleration, respectively, while keeping the field of view, matrix size, and spatial resolution constant [2]. The relationship between the acceleration factor and acquisition time is direct: Omitting more phase-encoding steps reduces the scan duration proportionally. However, a predictable trade-off in SNR (proportional to the square root of the acceleration factor), as well as *g*-factor-related penalties (arising from coil geometry and spatial encoding limitations), have traditionally prevented the clinical use of acceleration factors higher than two to three for 2D TSE imaging, and four for 3D TSE imaging [2]. Faster acceleration typically introduces inhomogeneous noise amplification and aliasing artifacts, particularly when surpassing the effective number of available receive coil elements in the phase-encoding direction [3]. For example, a knee coil comprised of 18 individual coil elements may have the geometry of three longitudinal coil rings of six coil elements each, usually leading to uncorrectable aliasing artifacts when fourfold acceleration is applied across the three rings.

Recent developments in deep learning (DL)-based image reconstruction methods now allow us to overcome these longstanding limitations. Deep Resolve Boost enhances parallel imaging accelerated TSE pulse sequences and requires fewer sampled raw data to form diagnostic-quality images. Image reconstruction combines a physical MRI model with neural network-based regularization, incorporating *k*-space data and coil sensitivity maps to adaptively address heterogeneous noise patterns and aliasing artifacts while ensuring data consistency. [4]. The resulting ability of DL reconstruction methods to produce images from fourfold parallel imaging accelerated 2D TSE datasets, rivaling or even outperforming conventional image reconstruction from twofold accelerated data, is paradigm-shifting [5]. By mitigating SNR losses and correcting aliasing artifacts, these tools allow for greater acceleration flexibility without compromising diagnostic image quality, thereby redefining the speed and efficiency thresholds of modern musculoskeletal MRI [6]. Deep Resolve Boost for TSE imaging is clinically available at field strengths from 0.55T to 7T and offers unprecedented speed gains in musculoskeletal MRI while preserving image quality.

Deep learning-enhanced simultaneous multislice imaging: Breaking the slice barrier

Simultaneous multislice (SMS) is a key enabler of next-generation ultra-fast musculoskeletal MRI. Combined with parallel imaging and elliptical *k*-space scanning, it substantially amplifies acceleration, laying the foundation for DL-driven MRI at unprecedented speeds [7].

In contrast to traditional sequential slice acquisition patterns of TSE pulse sequences, SMS simultaneously excites and captures MR signals from more than one slice. Like parallel imaging acceleration, SMS relies on deconvolution algorithms such as CAIPIRINHA (Controlled Aliasing in Parallel Imaging Results in Higher Acceleration) to separate mixed MR signals for accurate reconstruction of slice-specific image data using coil sensitivity maps, field-of-view shifts, and gradient encoding [8, 9]. The SMS approach reduces the effective repetition time of a TSE pulse sequence, which can translate into both direct and indirect time savings. Direct benefits include reductions in repetition time, the obviation of concatenations, the ability to lengthen echo trains, and the simultaneous acquisition of in-phase and opposed-phase echoes for Dixon-based imaging. Indirect gains comprise time-neutral increases in slice coverage, reduced interslice gaps and slice thickness, and the incorporation of otherwise time-intensive fat suppression methods like SPAIR.

Perhaps most importantly, SMS synergizes particularly effectively with parallel imaging. While parallel imaging reduces scan time at the cost of both acceleration-factor-proportional and *g*-factor-related SNR losses, SMS introduces only minor *g*-factor-dependent reductions in SNR. However, simultaneously imparted RF pulses to excite more than one slice at a time increase energy deposition and SAR. In peripheral joint MRI, concerns regarding SAR can be mitigated using local transmit coils, optimized RF pulse designs, and moderate flip angles between 125° and 150° [3].

When applied in concert, SMS and parallel imaging yield multiplicative acceleration benefits. For example, combining twofold SMS acquisition with twofold parallel imaging of TSE pulse sequences enables fourfold TSE acceleration. Even without integrating DL reconstruction methods, this has enabled clinical five-minute, five-sequence knee MRI protocols at 1.5T and 3T with unchanged diagnostic performance compared with conventional twofold parallel imaging acceleration since 2020 [10].

In contrast, standalone fourfold parallel imaging in the knee exceeds the capabilities of conventional image reconstruction and leads to substantially degraded images with drastically reduced SNR and increased artifact burden [10].

The current development and future integration of end-to-end DL reconstruction methods for combined SMS-parallel imaging acceleration will further transform

the landscape. Extending DL-enhanced image reconstruction capabilities to simultaneously accelerated datasets, such as SMS2-PAT3, SMS3-PAT3, SMS2-PAT4, SMS3-PAT4, and SMS2-PAT6, may enable total acceleration factors exceeding 10, while preserving or enhancing image quality [11, 12]. The convergence of DL-enhanced SMS-parallel-imaging-accelerated musculoskeletal MRI is a powerful framework to build on. Much like a speedster breaking the dimensional barrier, these technologies allow musculoskeletal MRI to transcend former limits.

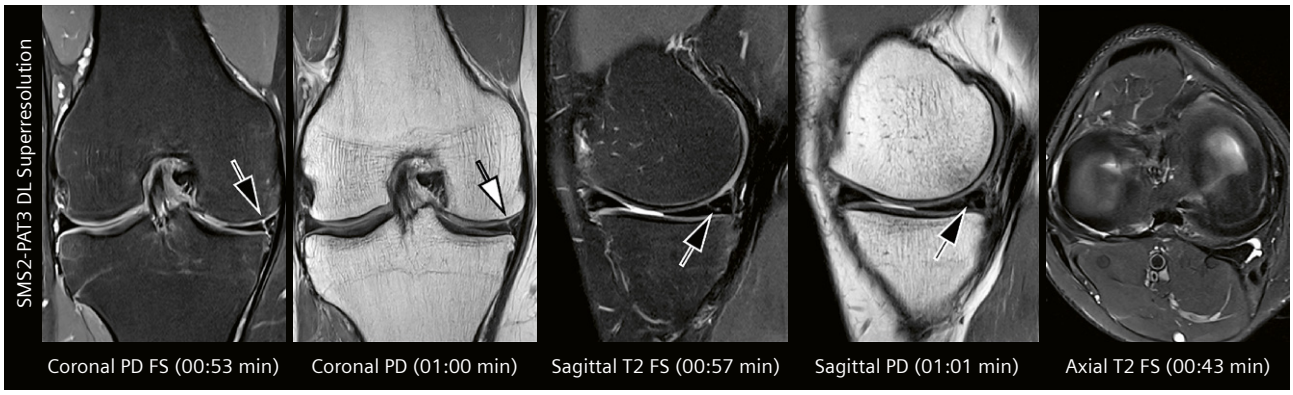

1 3-Tesla knee MRI with echo-train-compacted turbo spin-echo pulse sequences using combined twofold simultaneous multislice and threefold parallel imaging acceleration with deep learning-based image reconstruction and superresolution augmentation. The MR images show a vertical longitudinal medial meniscus tear (arrows).
MR images were obtained with a 3T MAGNETOM Vida MRI system and a 1-transmit-channel-18-receiver-channel knee coil. The MRI protocol is given in Table 1. PD = proton density weighting, PD FS = fat-suppressed proton density weighting, T2 FS = fat-suppressed T2 weighting.

Parameter	Ax T2 FS	Cor PD	Cor PD FS	Sag T2 FS	Sag PD
Gradient performance	high	high	high	high	high
Radiofrequency speed	fast	fast	fast	fast	fast
Repetition/echo time [ms]	3600 / 57	3700 / 24	3700 / 35	3700 / 56	3700 / 24
PI	3	3	3	3	3
SMS / FOV shift	2 / 2	2 / 2	2 / 2	2 / 2	2 / 2
Echo-train length	13	13	13	13	13
Bandwidth [Hz/pixel]	296	354	301	299	354
Echo spacing [ms]	7.1	8.0	7.1	8.0	8.0
FOV [mm]	140 × 140	140 × 140	140 × 140	140 × 140	140 × 140
Matrix	272 × 204	336 × 252	272 × 204	304 × 228	336 × 252
Slice thickness [mm]	3	3	3	3	3
Slices	38	36	36	38	38
Phase direction	right-to-left	head-to-foot	head-to-foot	head-to-foot	head-to-foot
Flip angle [°]	125	125	125	125	125
Acquisition time [mm:ss]	00:43	01:00	00:53	00:57	01:01

Table 1: NYU comprehensive rapid 3T sixfold SMS2-PAT3-accelerated knee MRI protocol.
Ax = axial, Cor = coronal, Sag = sagittal, PD = proton density weighted, FS = fat suppression, PI = parallel imaging acceleration factor, SMS = simultaneous multi-slice acquisition acceleration factor, FOV = field of view

Deep learning superresolution reconstruction: Precision at speed

Achieving higher spatial resolution in musculoskeletal MRI is essential for visualizing small anatomical details and detecting subtle pathology. However, the inherent trade-off between spatial resolution and SNR – defined by an inverse square-root relationship – posed a persistent challenge until recently. Higher-resolution acquisitions typically required longer scan times and came at the cost of reduced SNR, representing the well-known "no free lunch in MRI" theory.

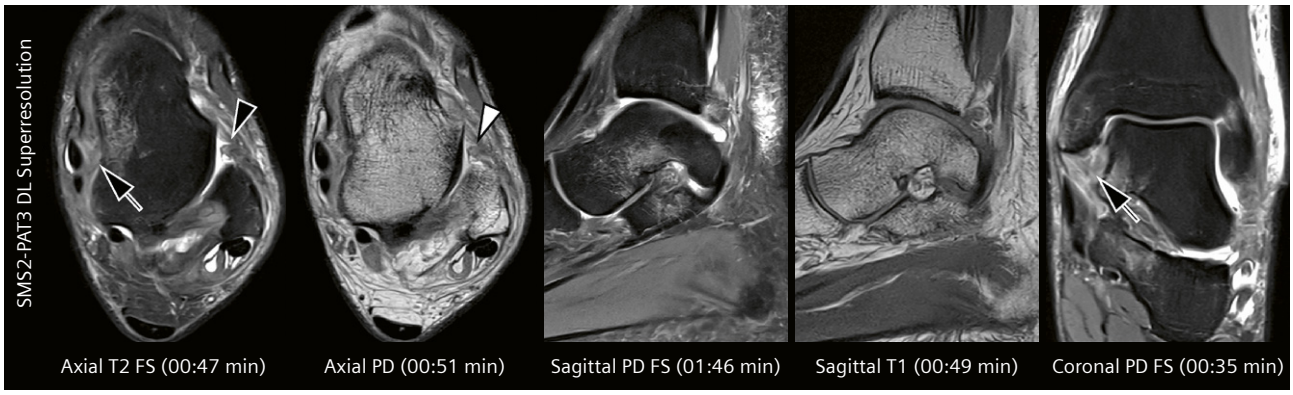

2 3-Tesla ankle MRI with echo-train-compacted turbo spin-echo pulse sequences using combined twofold simultaneous multislice and threefold parallel imaging acceleration with deep learning-based image reconstruction and superresolution augmentation. The MR images show sequela of a recent ankle sprain injury with tears of the deep fibers of the deltoid ligament complex (arrows) and the anterior talofibular ligament (arrowheads), as well as contusions of the medial talus and calcaneus without evidence of fracture.
MR images were obtained with a 3T MAGNETOM Vida MRI system and a 16-receiver-channel ankle/foot coil. The MRI protocol is given in Table 2. PD = proton density weighting, PD FS = fat-suppressed proton density weighting, T2 FS = fat-suppressed T2 weighting.

Parameter	Ax T2 FS	Ax PD	Sag PD FS	Cor PD FS	Sag T1
Gradient performance	high	high	high	high	high
Radiofrequency speed	low	low	normal	low	low
Repetition/echo time [ms]	4180 / 39	3800 / 19	5820 / 37	4000 / 39	400 / 8.9
PI	3	3	2	3	3
SMS / FOV shift	2 / 2	2 / 2	2 / 4	2 / 2	2 / 2
Echo-train length	14	14	16	14	4
Bandwidth [Hz/pixel]	305	354	304	305	347
Echo spacing [ms]	9.7	9.6	9.2	9.7	8.9
FOV [mm]	140 × 100	140 × 143	140 × 140	140 × 103	140 × 140
Matrix	304 × 228	336 × 252	336 × 252	304 × 228	272 × 204
Slice thickness [mm]	3	3	3	3	3
Slices	36	36	28	34	28
Phase direction	right-to-left	right-to-left	anterior-to-posterior	right-to-left	anterior-to-posterior
Flip angle [°]	138	121	160	126	127
Acquisition time [mm:ss]	00:47	00:51	01:46	00:49	00:35

Table 2: NYU comprehensive rapid 3T sixfold SMS2-PAT3-accelerated ankle MRI protocol.
Ax = axial, Cor = coronal, Sag = sagittal, PD = proton density weighted, FS = fat suppression, PI = parallel imaging acceleration factor, SMS = simultaneous multi-slice acquisition acceleration factor, FOV = field of view

The recent introduction of DL-based superresolution augmentation offers a transformative approach to breaking the interconnection of speed, image detail, and SNR. By computationally enhancing spatial resolution from lower-resolution acquisitions, these methods enable faster imaging without compromising diagnostic detail [11]. This allows MRI raw data to be acquired with lower matrix sizes in shorter acquisition windows while yielding high-resolution output image data. Alternatively, image detail can be improved beyond what is achievable with conventional techniques in the same scan time.

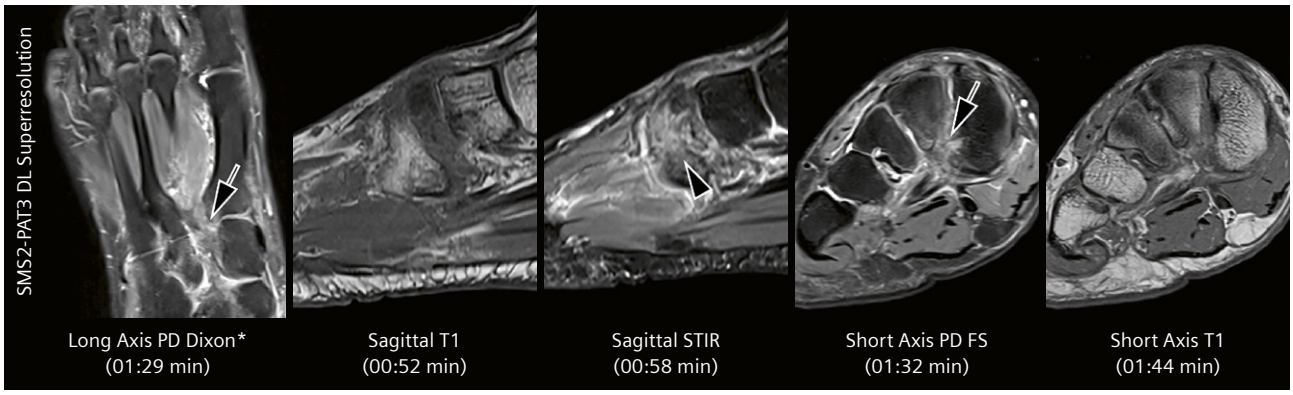

3 3-Tesla MRI of the midfoot with echo-train-compacted turbo spin-echo pulse sequences using combined twofold simultaneous multislice and twofold parallel imaging acceleration with deep learning-based image reconstruction and superresolution augmentation (*PD Dixon images were reconstructed with conventional methods because Deep Resolve Boost is not yet clinically available for Dixon-based fat-water separation). The MR images show high-grade tearing of the Lisfranc ligament (arrows) with surrounding soft tissue edema and adjacent osseous contusions (arrowhead).
MR images were obtained with a 3T MAGNETOM Vida MRI system and a 16-receiver-channel ankle/foot coil. The MRI protocol is given in Table 3. PD = proton density weighting, PD FS = fat-suppressed proton density weighting, STIR = short tau inversion recovery.

Parameter	Short axis PD FS	Short axis T1	Sag STIR	Sag T1	Long axis PD Dixon
Gradient performance	high	high	high	high	high
Radiofrequency speed	low	low	normal	low	normal
Repetition/echo time [ms]	6000 / 37	600 / 9.2	3030 / 33	600 / 8.6	3800 / 42
PI	2	2	2	2	2
SMS / FOV shift	2 / 4	2 / 4	2 / 4	2 / 4	2 / 2
Echo-train length	14	4	9	4	14
Bandwidth [Hz/pixel]	305	350	295	348	395
Echo spacing [ms]	9.2	9.2	8.3	8.6	10.4
FOV [mm]	120 × 109	120 × 108	200 × 138	200 × 141	200 × 144
Matrix	256 × 184	304 × 219	320 × 240	368 × 276	384 × 277
Slice thickness [mm]	3	3	3	3	3
Slices	54	54	34	32	30
Phase direction	right-to-left	right-to-left	head-to-foot	head-to-foot	right-to-left
Flip angle [°]	117	115	125	123	150
Acquisition time [mm:ss]	01:32	01:44	00:58	00:52	01:29

Table 3: NYU comprehensive rapid 3T fourfold SMS2-PAT2-accelerated forefoot/midfoot MRI protocol.
Sag = sagittal, PD = proton density weighted, FS = fat suppression, STIR = short tau inversion recovery, PI = parallel imaging acceleration factor, SMS = simultaneous multi-slice acquisition acceleration factor, FOV = field of view

Historically, interpolation methods such as zero-filling have been employed to estimate higher-resolution images, though these have shown limited effectiveness for musculoskeletal MRI [1, 13]. Deep Resolve Sharp, in contrast, has been trained on large datasets of paired low- and high-resolution images across various sequences and contrast settings, and seemingly enhances the level of image detail and visualization of small structural abnormalities [4]. Deep Resolve Sharp can effectively double the matrix size in both in-plane directions for 2D acquisitions and can augment slice resolution by a factor of two for 3D datasets to enhance image resolution.

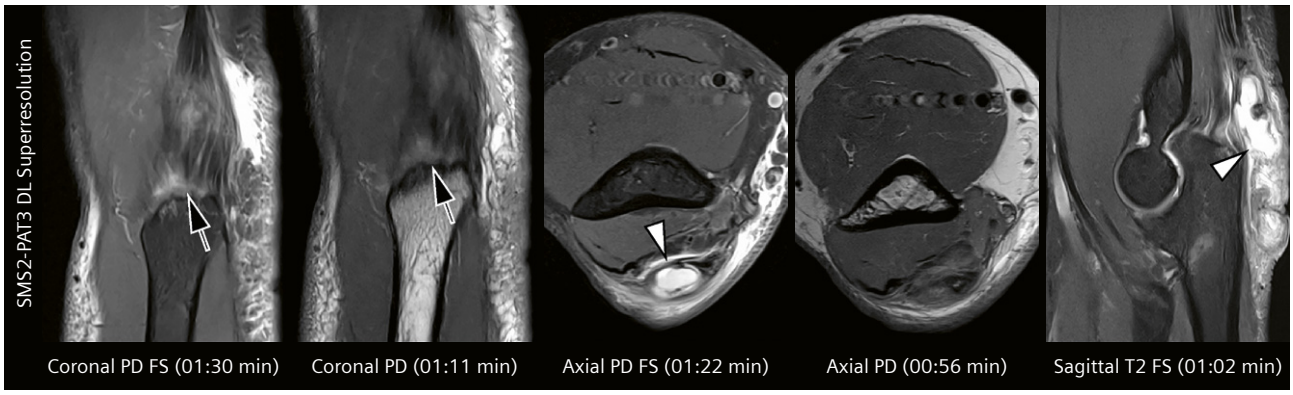

4 3-Tesla MRI of the elbow with echo-train-compacted turbo spin-echo pulse sequences using combined twofold simultaneous multislice and twofold parallel imaging acceleration with deep learning-based image reconstruction and superresolution augmentation. The MR images show a high-grade partial-thickness tear of the distal triceps tendon from the olecranon insertion (arrows) and associated moderate olecranon bursitis (arrowheads) with surrounding soft tissue edema.
MR images were obtained with a 3T MAGNETOM Vida MRI system and a 1-transmit-channel-18-receiver-channel knee coil. The MRI protocol is given in Table 4. PD = proton density weighting, PD FS = fat-suppressed proton density weighting, T2 FS = fat-suppressed T2 weighting.

Parameter	Ax PD	Ax PD FS	Cor PD FS	Cor PD	Sag T2 FS
Gradient performance	high	high	high	high	high
Radiofrequency speed	normal	normal	normal	normal	normal
Repetition/echo time [ms]	3800 / 28	3800 / 38	3800 / 38	3800 / 28	3800 / 46
PI	2	2	2	2	2
SMS / FOV shift	2 / 4	2 / 4	2 / 4	2 / 4	2 / 4
Echo-train length	15	11	11	15	15
Bandwidth [Hz/pixel]	281	294	299	286	299
Echo spacing [ms]	9.34	9.48	9.50	9.26	9.16
FOV [mm]	120 × 120	120 × 120	120 × 120	120 × 120	120 × 120
Matrix	336 × 252	288 × 216	288 × 216	336 × 252	288 × 216
Slice thickness [mm]	3	3	2.8	2.8	3
Slices	34	36	32	30	26
Phase direction	right-to-left	right-to-left	head-to-foot	head-to-foot	head-to-foot
Flip angle [°]	123	125	125	125	125
Acquisition time [mm:ss]	00:56	01:22	01:30	01:11	01:02

Table 4: NYU comprehensive rapid 3T fourfold SMS2-PAT2-accelerated elbow MRI protocol.
Ax = axial, Cor = coronal, Sag = sagittal, PD = proton density weighted, FS = fat suppression, PI = parallel imaging acceleration factor, SMS = simultaneous multi-slice acquisition acceleration factor, FOV = field of view

Most importantly, Deep Resolve Sharp can be integrated with advanced acceleration and image reconstruction methods, including parallel imaging, SMS acquisition, and Deep Resolve Boost, further enhancing the speed and quality of musculoskeletal MRI. This multi-layered approach enables the generation of superresolution images from rapidly acquired, undersampled datasets, delivering stunning visual improvements and meaningful real-life gains in diagnostic confidence [4].

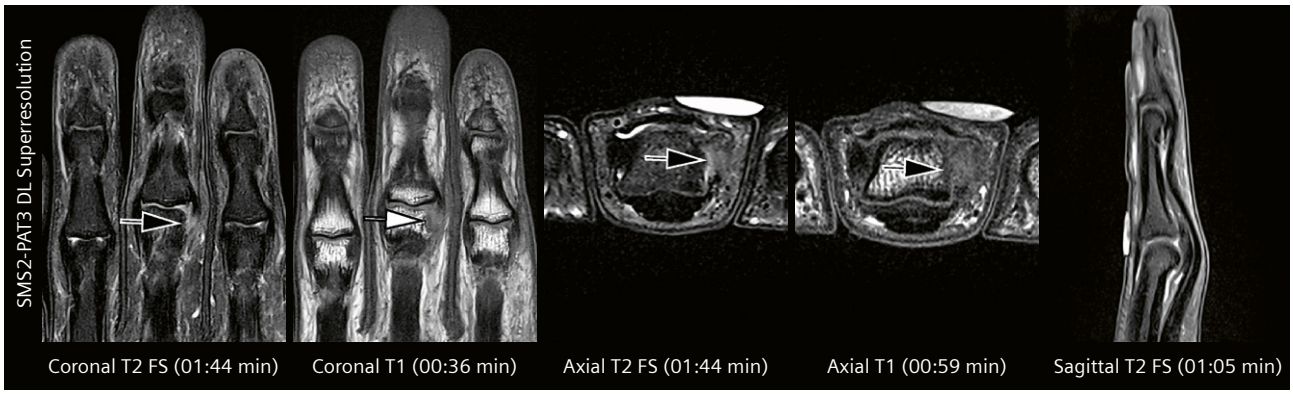

5 3-Tesla MRI of the fingers with echo-train-compacted turbo spin-echo pulse sequences using combined twofold simultaneous multislice and twofold parallel imaging acceleration with deep learning-based image reconstruction and superresolution augmentation. The MR images show a tear of the radial collateral ligament of the middle finger at the proximal insertion at the proximal phalanx (arrows).
MR images were obtained with a 3T MAGNETOM Vida MRI system and a 16-receiver-channel hand/wrist coil. The MRI protocol is given in Table 5. T2 FS = fat-suppressed T2 weighting.

Parameter	Ax T1	Sag T2 FS	Ax T2 FS	Cor T1	Cor T2 FS
Gradient performance	high	high	high	high	high
Radiofrequency speed	low	low	low	low	fast
Repetition/echo time [ms]	500 / 11	4000 / 43	4280 / 70	400 / 12	4500 / 65
PI	2	2	2	2	2
SMS / FOV shift	2 / 4	2 / 4	2 / 4	2 / 4	2 / 4
Echo-train length	3	16	11	3	11
Bandwidth [Hz/pixel]	363	301	289	289	284
Echo spacing [ms]	11.2	10.8	11.7	11.8	9.3
FOV [mm]	80 × 80	100 × 103	80 × 80	100 × 100	100 × 100
Matrix	320 × 288	272 × 204	304 × 228	320 × 256	320 × 256
Slice thickness [mm]	3	3	3	2.2	2.2
Slices	36	18	36	16	16
Phase direction	anterior-to-posterior	head-to-foot	right-to-left	right-to-left	right-to-left
Flip angle [°]	117	130	112	120	120
Acquisition time [mm:ss]	00:59	01:05	01:44	00:36	01:44

Table 5: NYU comprehensive rapid 3T fourfold SMS2-PAT2-accelerated finger MRI protocol.
Ax = axial, Cor = coronal, Sag = sagittal, FS = fat suppression, PI = parallel imaging acceleration factor, SMS = simultaneous multi-slice acquisition acceleration factor, FOV = field of view

Putting it all together: Where we stand and where we are headed

The combined use of finely tuned TSE pulse sequences with compact echo trains, advanced image acceleration techniques like parallel imaging and SMS acquisitions, and DL-based image reconstruction and superresolution augmentation methods facilitate clinical sixfold (SMS2-PAT3) accelerated DL superresolution MRI of the knee (Fig. 1, Table 1) with excellent diagnostic performance for the detection of intra-articular structural abnormalities [14]. Similarly, fourfold (SMS2-PAT2) to sixfold (SMS2-PAT3) accelerated DL superresolution MRI of the ankle (Fig. 2,

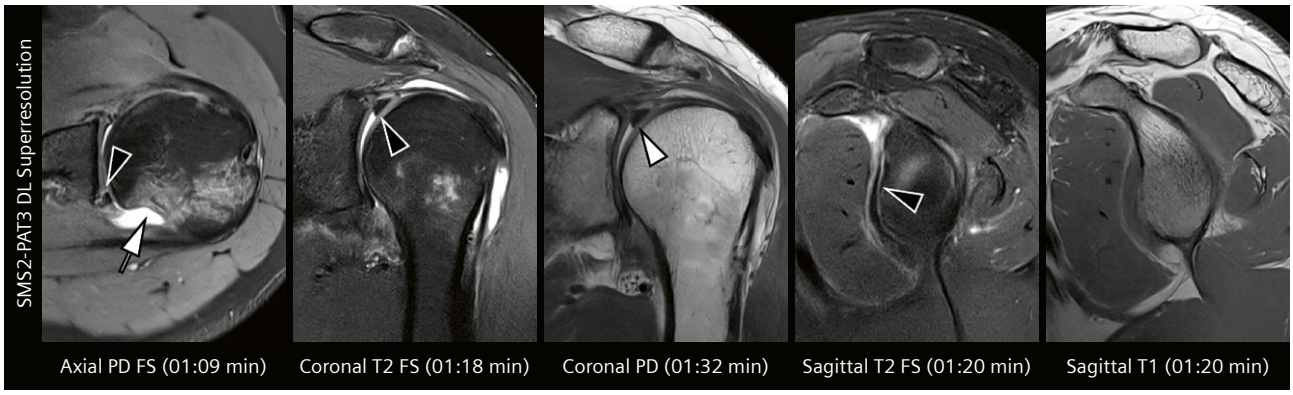

6 3-Tesla MRI of the shoulder with echo-train-compacted turbo spin-echo pulse sequences using threefold parallel imaging acceleration with deep learning-based image reconstruction and superresolution augmentation. The MR images show sequela of a recent anterior shoulder dislocation with a large Hill-Sachs fracture with adjacent bone marrow edema (arrow) and extensive, 360-degree labral tear, including displacement of the superior labrum (arrowheads).
MR images were obtained with a 3T MAGNETOM Vida MRI system and a 16-receiver-channel shoulder coil. The MRI protocol is given in Table 6. PD = proton density weighting, PD FS = fat-suppressed proton density weighting, T2 FS = fat-suppressed T2 weighting.

Parameter	Ax PD FS	Cor T2 FS	Cor PD	Sag T2 FS	Sag T1
Gradient performance	high	high	high	high	high
Radiofrequency speed	normal	low	low	low	low
Repetition/echo time [ms]	4200 / 31	4350 / 54	3970 / 35	5030 / 53	786 / 11
PI	3	3	3	3	3
SMS / FOV shift	0 / 0	0 / 0	0 / 0	0 / 0	0 / 0
Echo-train length	11	12	11	13	4
Bandwidth [Hz/pixel]	260	252	279	217	279
Echo spacing [ms]	10.3	10.8	11.5	10.6	10.6
FOV [mm]	140 × 140	140 × 140	140 × 140	140 × 140	140 × 140
Matrix	320 × 256	320 × 256	448 × 314	320 × 240	320 × 256
Slice thickness [mm]	3	3	3	3	3
Slices	30	28	28	28	28
Phase direction	anterior-to-posterior	head-to-foot	head-to-foot	head-to-foot	head-to-foot
Flip angle [°]	150	150	150	150	150
Acquisition time [mm:ss]	01:09	01:18	01:32	01:20	01:20

Table 6: NYU comprehensive rapid 3T threefold PAT3-accelerated shoulder MRI protocol.
Ax = axial, Cor = coronal, Sag = sagittal, PD = proton density weighted, FS = fat suppression, PI = parallel imaging acceleration factor, SMS = simultaneous multi-slice acquisition acceleration factor, FOV = field of view

Table 2), foot (Fig. 3, Table 3), elbow (Fig. 4, Table 4), and fingers (Fig. 5, Table 5) are routinely used in clinical practice with acquisition times of five to six minutes. Such comprehensive yet rapid MRI protocols can be accommodated in 10- to 15-minute MRI appointment times in architecturally optimized settings to maximize operational efficiency and sustainability [15, 16]. Imaging of peripheral joints benefits from closed coil designs and advantageous geometric arrangements of individual coil elements that prevent extensive aliasing artifacts and incomplete slice separation compared with central joints like the shoulder and hip, and in the spine. Combined parallel imaging and SMS acceleration for these joints may result in incomplete artifact removal during image reconstruction, even with current DL methods. However, three- to fourfold parallel imaging accelerated DL superresolution MRI, e.g., in the shoulder, can be achieved with excellent diagnostic performance in an acquisition time below seven minutes [17] (Fig. 6, Table 6). Future directions include the clinical implementation of currently developed end-to-end DL reconstruction methods for combined PI-SMS acceleration that promise to eliminate residual aliasing artifacts and make artifact-free eight- to twelvefold-accelerated DL superresolution musculoskeletal MRI with acquisition times below three minutes a clinical reality in the near future.

These developments have pushed through frontiers in musculoskeletal MRI by breaking physical interconnections with acceleration factors at a level of image detail that no one believed was possible a few years ago. However, the journey to new horizons has likely just started, and our excitement for enhancing the efficiency and value of musculoskeletal MRI is exponentially accelerating. We are on the verge of further bending the rules of time and physics and racing toward a future where ultra-fast superresolution MRI is not just possible, but also global routine clinical practice.

References

1 Del Grande F, Guggenberger R, Fritz J. Rapid Musculoskeletal MRI in 2021: Value and Optimized Use of Widely Accessible Techniques. AJR Am J Roentgenol. 2021;216(3):704–717.
2 Vosshenrich J, Koerzdoerfer G, Fritz J. Modern acceleration in musculoskeletal MRI: applications, implications, and challenges. Skeletal Radiol. 2024;53(9):1799–1813.
3 Fritz J, Guggenberger R, Del Grande F. Rapid Musculoskeletal MRI in 2021: Clinical Application of Advanced Accelerated Techniques. AJR Am J Roentgenol. 2021;216(3):718–733.
4 Walter SS, Vosshenrich J, Cantarelli Rodrigues T, Dalili D, Fritz B, Kijowski R, et al. Deep Learning Superresolution for Simultaneous Multislice Parallel Imaging-Accelerated Knee MRI Using Arthroscopy Validation. Radiology. 2025;314(1):e241249.
5 Recht MP, Zbontar J, Sodickson DK, Knoll F, Yakubova N, Sriram A, et al. Using Deep Learning to Accelerate Knee MRI at 3 T: Results of an Interchangeability Study. AJR Am J Roentgenol. 2020;215(6):1421–1429.
6 Fritz J, Kijowski R, Recht MP. Artificial intelligence in musculoskeletal imaging: a perspective on value propositions, clinical use, and obstacles. Skeletal Radiol 2022;51(2):239–243.
7 Fritz J, Fritz B, Zhang J, Thawait GK, Joshi DH, Pan L, et al. Simultaneous Multislice Accelerated Turbo Spin Echo Magnetic Resonance Imaging: Comparison and Combination With In-Plane Parallel Imaging Acceleration for High-Resolution Magnetic Resonance Imaging of the Knee. Invest Radiol. 2017;52(9):529–537.
8 Barth M, Breuer F, Koopmans PJ, Norris DG, Poser BA. Simultaneous multislice (SMS) imaging techniques. Magn Reson Med. 2016;75(1):63–81.
9 Breuer F, Blaimer M, Griswold MA, Jakob PM. CAIPIRINHA – Revisited. Simultaneous Multi-Slice Supplement. MAGNETOM Flash. 2025;63(3):8–15.
10 Del Grande F, Rashidi A, Luna R, Delcogliano M, Stern SE, Dalili D, et al. Five-Minute Five-Sequence Knee MRI Using Combined Simultaneous Multislice and Parallel Imaging Acceleration: Comparison with 10-Minute Parallel Imaging Knee MRI. Radiology. 2021;299(3):635–646.
11 Lin DJ, Walter SS, Fritz J. Artificial Intelligence-Driven Ultra-Fast Superresolution MRI: 10-Fold Accelerated Musculoskeletal Turbo Spin Echo MRI Within Reach. Invest Radiol. 2023;58(1):28–42.
12 Fritz J. Boldly Going Where No One Has Gone Before – The Roadmap to 10-fold Accelerated Routine Musculoskeletal MRI Exams. MAGNETOM Flash. 2021;79(2):4–14.
13 Bernstein MA, Fain SB, Riederer SJ. Effect of windowing and zero-filled reconstruction of MRI data on spatial resolution and acquisition strategy. J Magn Reson Imaging. 2001;14(3):270–80.
14 Vosshenrich J, Breit HC, Donners R, Obmann MM, Walter SS, Serfaty A, et al. Clinical Implementation of Sixfold-Accelerated Deep Learning Super-Resolution Knee MRI in Under 5 Minutes: Arthroscopy-Validated Diagnostic Performance. AJR Am J Roentgenol. 2025 Apr 23. doi: 10.2214/AJR.25.32878. Epub ahead of print.
15 Recht MP, Block KT, Chandarana H, Friedland J, Mullholland T, Teahan D, et al. Optimization of MRI Turnaround Times Through the Use of Dockable Tables and Innovative Architectural Design Strategies. AJR Am J Roentgenol. 2019;212(4):855–858.
16 Chaban YV, Vosshenrich J, McKee H, Gunasekaran S, Brown MJ, Atalay MK, et al. Environmental Sustainability and MRI: Challenges, Opportunities, and a Call for Action. J Magn Reson Imaging. 2024;59(4):1149–1167.
17 Vosshenrich J, Bruno M, Cantarelli Rodrigues T, Donners R, Jardon M, Leonhardt Y, et al. Arthroscopy-validated Diagnostic Performance of 7-Minute Five-Sequence Deep Learning Super-Resolution 3-T Shoulder MRI. Radiology. 2025;314(2):e241351.

Contact

Jan Vosshenrich, M.D.
University Hospital Basel
Department of Radiology
Spitalstrasse 21
4031 Basel
Switzerland
jan.vosshenrich@usb.ch

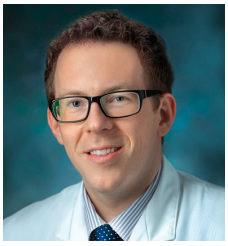

Jan Fritz, M.D.
New York University
Grossman School of Medicine
Department of Radiology
550 1st Avenue, 2nd Floor
New York, NY 10016
USA
jan.fritz@nyulangone.org

Deep Learning-Accelerated FLAIR Imaging: A Non-Contrast Alternative for Knee Synovitis Assessment

Georg C. Feuerriegel, M.D.[1]; Sophia S. Goller, M.D., MBA[1]; Constantin von Deuster, Ph.D.[2, 3]; Reto Sutter, M.D.[1]

[1]Department of Radiology, Balgrist University Hospital, Faculty of Medicine, University of Zurich, Switzerland
[2]Swiss Innovation Hub, Siemens Healthineers AG, Zurich, Switzerland
[3]Swiss Center for Musculoskeletal Imaging (SCMI), Balgrist Campus, Zurich, Switzerland

Abstract

Magnetic resonance imaging (MRI) plays a crucial role in diagnosing and monitoring inflammatory arthritis. While contrast-enhanced (CE) imaging is the gold standard for synovitis assessment, concerns regarding gadolinium-based contrast agents necessitate the exploration of alternatives without contrast enhancement. In this study, we evaluated a deep learning (DL)-accelerated fluid-attenuated inversion recovery (FLAIR) sequence[1] with fat saturation (FS) against conventional CE T1-weighted (T1w) FS imaging for knee synovitis assessment. Fifty-five patients underwent 3T MRI with both imaging techniques. Semiquantitative scoring of synovitis, image quality, and reader confidence was assessed independently by two radiologists for the CE T1w FS and FLAIR FS sequences. No significant differences in whole-knee synovitis scores, effusion synovitis scores, or Hoffa synovitis scores were found between the sequences, with high inter- and intra-reader agreement. The DL-accelerated FLAIR FS sequence reduced scan time by 66% while maintaining diagnostic accuracy. These findings suggest that a DL-accelerated FLAIR FS sequence provides a noncontrast alternative to CE imaging for the assessment of inflammatory changes in the knee.

[1]Work in progress. The application is currently under development and is not for sale in the U.S. and in other countries. Its future availability cannot be ensured.

Sequence	CE T1w FS	FLAIR FS
Echo time (ms)	10	91
Repetition time (ms)	755	6070
Slice thickness (mm)	2.5	2.5
Acquisition matrix	448 × 314	204 × 274
Imaged field of view (mm)	149 × 149	180 × 180
Readout bandwidth (Hz/pixel)	180	289
Acquisition time (min:sec)	4:50	1:38
iPAT factor	2	4
Inversion time (ms)	N/A	1855

Table 1: Sequence parameters

Introduction

Synovitis is a key feature of inflammatory arthritis and is associated with disease progression and joint damage [1]. Magnetic resonance imaging (MRI) is the preferred imaging modality for detecting and monitoring synovitis, with contrast-enhanced T1-weighted fat-saturated (CE T1w FS) sequences being the preferred imaging standard [2]. However, the use of gadolinium-based contrast agents is associated with potential nephrotoxicity, deposition concerns, and patient discomfort [3, 4]. This has fueled interest in noncontrast alternatives. Fluid-attenuated inversion recovery (FLAIR) imaging, traditionally employed for MRI of the brain, has shown promise in musculoskeletal applications due to its ability to suppress free fluid signals while highlighting inflammatory changes [5]. Recent advances in deep learning (DL)-accelerated imaging techniques have significantly improved FLAIR imaging quality and acquisition times [6]. Therefore, this study compared a DL-accelerated FLAIR FS sequence with a standard CE T1w FS sequence to investigate their efficacy in assessing cases of suspected acute and chronic synovitis of the knee [7].

Technique

This prospective study included 55 patients (mean age: 49.3 years) with suspected knee synovitis [7]. All patients underwent MRI at 3T on a MAGNETOM Vida scanner (Siemens Healthineers, Erlangen, Germany) using a routine MRI protocol that included a CE T1w FS sequence and a DL-accelerated FLAIR FS sequence.

The fourfold-accelerated FLAIR FS images were obtained in 1 minute, 38 seconds, and reconstructed using a DL algorithm (Deep Resolve Boost and Deep Resolve Sharp, Siemens Healthineers, Erlangen, Germany; Fig. 1). The algorithm was inspired by variational networks to enhance the signal-to-noise ratio and image sharpness [8]. The CE T1w FS sequence was performed after intravenous administration of a gadolinium-based contrast agent, and had an acquisition time of 4 minutes, 50 seconds. Detailed image parameters are listed in Table 1.

Image analysis

Two fellowship-trained musculoskeletal radiologists independently assessed the images using a semiquantitative scoring system, including the whole-knee synovitis sum score (range 0–27) the Hoffa synovitis score (range 0–3), and the effusion synovitis score (range 0–3). Image quality (sharpness, contrast, and artifact presence) and diagnostic confidence were rated on a 5-point Likert scale. Inter- and intrareader reliability were analyzed using Cohen's kappa statistic.

1 Axial FLAIR FS image without DL reconstruction **(1A)** and with Deep Resolve Boost and Deep Resolve Sharp reconstruction **(1B)**, showing excellent noise reduction and image contrast.

Results

Synovitis assessment

There were no significant differences between DL-accelerated FLAIR FS and CE T1w FS sequences in whole-knee synovitis scores (FLAIR: 10.69 ± 8.83 vs. CE T1w FS: 10.74 ± 10.32; p = 0.521). Both the Hoffa synovitis score and the effusion synovitis score showed excellent agreement between sequences (Figs. 2 and 3).

Image quality and diagnostic confidence

Both sequences were rated similarly in terms of image quality (FLAIR FS: 4.3 ± 0.7 vs. CE T1w FS: 4.5 ± 0.6; p = 0.312) and diagnostic confidence (FLAIR FS: 4.6 ± 0.6 vs. CE T1w FS: 4.7 ± 0.5; p = 0.297). DL-accelerated FLAIR FS exhibited fewer artifacts and noise, as well as enhanced signal contrast compared to the undersampled FLAIR sequence.

Inter- and intrareader agreement

Cohen's kappa values for inter- and intrareader agreement were excellent (0.82–0.96), indicating a high reproducibility of findings across both imaging techniques.

Scan time reduction

The DL-accelerated FLAIR FS sequence reduced acquisition time by 66%, providing a time-efficient alternative without compromising diagnostic accuracy.

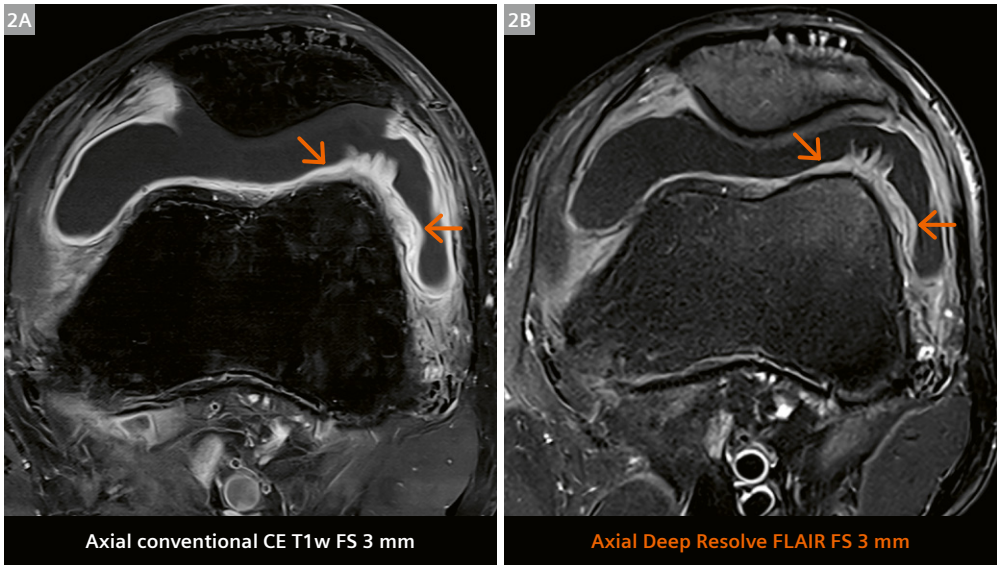

2 A conventional contrast-enhanced (CE) T1w image **(2A)** with fat saturation (FS) compared to a noncontrast FLAIR FS image **(2B)** using Deep Resolve Boost and Deep Resolve Sharp. Note the contrast of the thickened synovium compared to the joint fluid, which is similar in the CE T1w FS sequence and the non-CE FLAIR FS sequence (arrows).

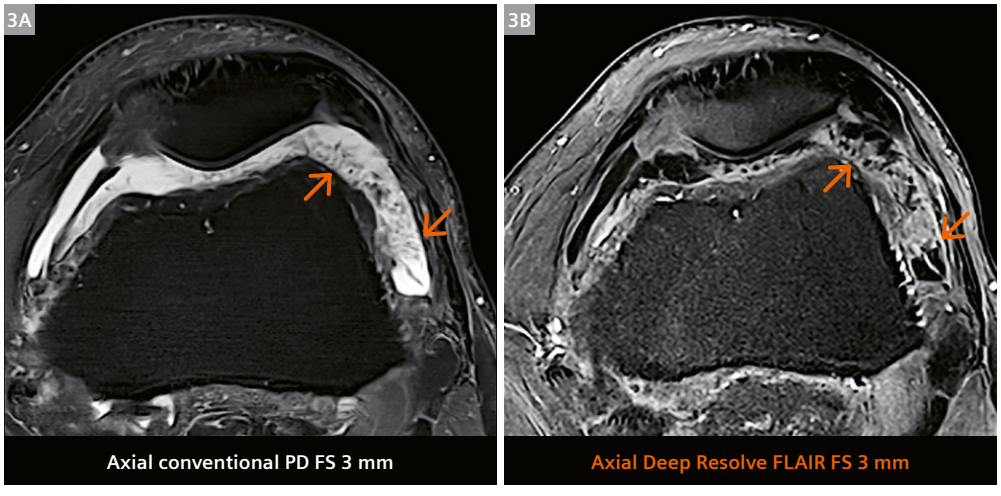

3 A conventional proton density-weighted image **(3A)** with fat saturation (FS) compared with a noncontrast FLAIR FS image **(3B)** using Deep Resolve Boost and Deep Resolve Sharp. Note the improved contrast of the thickened synovia compared to the joint fluid on the non-CE FLAIR FS sequence (arrows), which allows for better assessment of the degree of synovitis.

Discussion

DL-accelerated FLAIR FS imaging is a robust alternative to CE T1w FS imaging for knee synovitis assessment, as described in a study published in Investigative Radiology [7]. The ability of DL-accelerated FLAIR FS to suppress fluid signals while highlighting inflammatory changes makes it a valuable tool for detecting inflammatory changes of the synovia without the need for contrast agent administration. Additionally, the significant reduction in scan time enhances patient comfort and reduces the risk of movement artifacts. Given increasing concerns over gadolinium-based contrast agents, DL-accelerated FLAIR FS imaging provides a practical solution for patients with renal impairment or those requiring repeated MRI examinations. The DL-based reconstruction techniques used in this study significantly reduced image noise and artifacts while increasing image contrast and reducing scan time, further enhancing their clinical utility.

In summary, our study demonstrated that DL-accelerated FLAIR FS imaging is a viable noncontrast alternative to CE T1w FS imaging for knee synovitis assessment. It offers comparable diagnostic accuracy while significantly reducing scan time, enhancing accessibility, and eliminating the risks of gadolinium-based contrast agents. These findings support the clinical adoption of DL-enhanced noncontrast imaging techniques in musculoskeletal MRI.

References

1 Filippucci E, Di Geso L, Grassi W. Progress in imaging in rheumatology. Nat Rev Rheumatol. 2014;10(10):628-34.
2 Roemer FW, Kassim Javaid M, Guermazi A, Thomas M, Kiran A, Keen R, et al. Anatomical distribution of synovitis in knee osteoarthritis and its association with joint effusion assessed on non-enhanced and contrast-enhanced MRI. Osteoarthritis Cartilage. 2010;18(10):1269-74.
3 Ramalho J, Semelka RC, Ramalho M, Nunes RH, AlObaidy M, Castillo M. Gadolinium-Based Contrast Agent Accumulation and Toxicity: An Update. AJNR Am J Neuroradiol. 2016;37(7):1192-8. Orthop J Sports Med. 2020;8(3):2325967120909090.
4 McDonald RJ, McDonald JS, Kallmes DF, Jentoft ME, Murray DL, Thielen KR, et al. Intracranial Gadolinium Deposition after Contrast-enhanced MR Imaging. Radiology. 2015;275(3):772-82.
5 Yoo HJ, Hong SH, Oh HY, Choi JY, Chae HD, Ahn JM, et al. Diagnostic Accuracy of a Fluid-attenuated Inversion-Recovery Sequence with Fat Suppression for Assessment of Peripatellar Synovitis: Preliminary Results and Comparison with Contrast-enhanced MR Imaging. Radiology. 2017;283(3):769-778.
6 Johnson PM, Lin DJ, Zbontar J, Zitnick CL, Sriram A, Muckley M, et al. Deep Learning Reconstruction Enables Prospectively Accelerated Clinical Knee MRI. Radiology. 2023;307(2):e220425.
7 Feuerriegel GC, Goller SS, von Deuster C, Sutter R. Inflammatory Knee Synovitis: Evaluation of an Accelerated FLAIR Sequence Compared With Standard Contrast-Enhanced Imaging. Invest Radiol. 2024;59(8):599-604.
8 Hammernik K, Klatzer T, Kobler E, Recht MP, Sodickson DK, Pock T, et al. Learning a variational network for reconstruction of accelerated MRI data. Magn Reson Med. 2018;79(6):3055-3071.

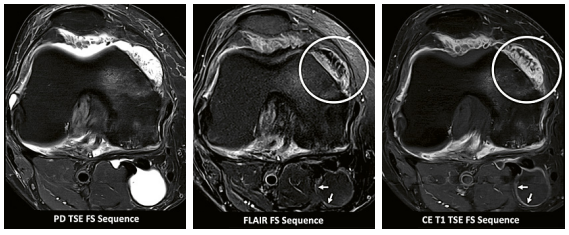

Feuerriegel GC, Goller SS, von Deuster C, Sutter R. Inflammatory Knee Synovitis: Evaluation of an Accelerated FLAIR Sequence Compared With Standard Contrast-Enhanced Imaging. Invest Radiol. 2024 Aug 1;59(8):599-604.

The study is available as an open access article here:

https://doi.org/10.1097/rli.0000000000001065

Contact

Georg C. Feuerriegel, M.D.
Fellow
Department of Radiology
Balgrist University Hospital
Forchstrasse 340
8008 Zurich
Switzerland
georg.feuerriegel@balgrist.ch

Reto Sutter, M.D.
Professor of Radiology
Head of Department
Department of Radiology
Balgrist University Hospital
Forchstrasse 340
8008 Zurich
Switzerland
reto.sutter@balgrist.ch

Highly Accelerated 3D Knee Cartilage Imaging using Deep Learning Reconstruction

Thomas Marth, Dr. med. univ.[1,2,3]; Adrian Alexander Marth, M.D.[2,3]; Georg Wilhelm Kajdi, M.D.[2,3]; Marcel Dominik Nickel, Ph.D.[4]; Dominik Paul, Ph.D.[4]; Reto Sutter, M.D.[2,3]; Daniel Nanz, Ph.D.[1,3]; Constantin von Deuster, Ph.D.[1,5]

[1]Swiss Center for Musculoskeletal Imaging, Balgrist Campus AG, Zurich, Switzerland
[2]Balgrist University Hospital, Radiology, University of Zurich, Switzerland
[3]Medical Faculty, University of Zurich, Switzerland
[4]Research & Clinical Translation, Magnetic Resonance, Siemens Healthineers, Erlangen, Germany
[5]Swiss Innovation Hub, Siemens Healthineers, Zurich, Switzerland

Introduction

Three-dimensional (3D) high-spatial-resolution MRI performed for morphological evaluation of the knee cartilage using double-echo steady-state (DESS) imaging is limited by long acquisition times. With deep-learning (DL) reconstructions now available for 3D imaging[1] as a research package, this obstacle can be overcome. In a recent feasibility study, we explored the limits of scan acceleration with different undersampling rates and schemes in combination with DL-based reconstructions: We showed the feasibility of acquiring high-resolution 0.3 mm isotropic DESS knee images within approximately one minute [1]. Here, we present 3D DESS knee images acquired at 7T and 3T, and image segmentation in Chondral Quant [2, 3], an automatic tool for quantitative analysis of the knee cartilage.

Materials and methods

One healthy volunteer underwent a knee examination on our 7T MAGNETOM Terra.X MR system equipped with a 1Tx/28Rx knee coil (QED, Quality Electrodynamics, Mayfield Village, OH, USA). DESS data was acquired with a research application sequence[1] with 4-fold accelerated GRAPPA, 8-fold accelerated CAIPIRINHA (CAIPI), and 16-fold accelerated Compressed Sensing (CS). Additionally, one healthy volunteer underwent a knee examination on our 3T MAGNETOM Prisma MR system equipped with a 1Tx/15Rx knee coil (QED, Quality Electrodynamics, Mayfield Village, OH, USA), and 12-fold accelerated CS DESS data was acquired. Detailed acquisition parameters are listed in Table 1. 16-fold accelerated 7T images (acquisition time 01:12 min) and 12-fold accelerated 3T images (acquisition time 01:04 min) were used for automatic knee cartilage segmentation in Version VA10A of Chondral Quant (*syngo*.via, Version VB60G).

Results

Figure 1 shows sagittal 3D DESS knee images with 4-fold GRAPPA, 8-fold CAIPI, and 16-fold CS acceleration at 7T. The combination of incoherent CS undersampling with DL reconstructions allows acceleration factors up to 16-fold without apparent impairment in image quality compared to GRAPPA with 4-fold acceleration. The 3D high-resolution reconstructions allow high-quality multiplanar reconstructions with an excellent depiction of the knee cartilage at 3T (Fig. 2). Figure 3 shows the accurate automatic segmentation of the knee cartilage with Chondral Quant in a 34-year-old healthy female at 3T. Figure 4 demonstrates the automatic segmentation of the knee cartilage of a 38-year-old volunteer at 7T.

[1] *Work in progress. The application is currently under development and is not for sale in the U.S. and in other countries. Its future availability cannot be ensured.*

MAGNETOM Terra.X (7T); 3D DESS

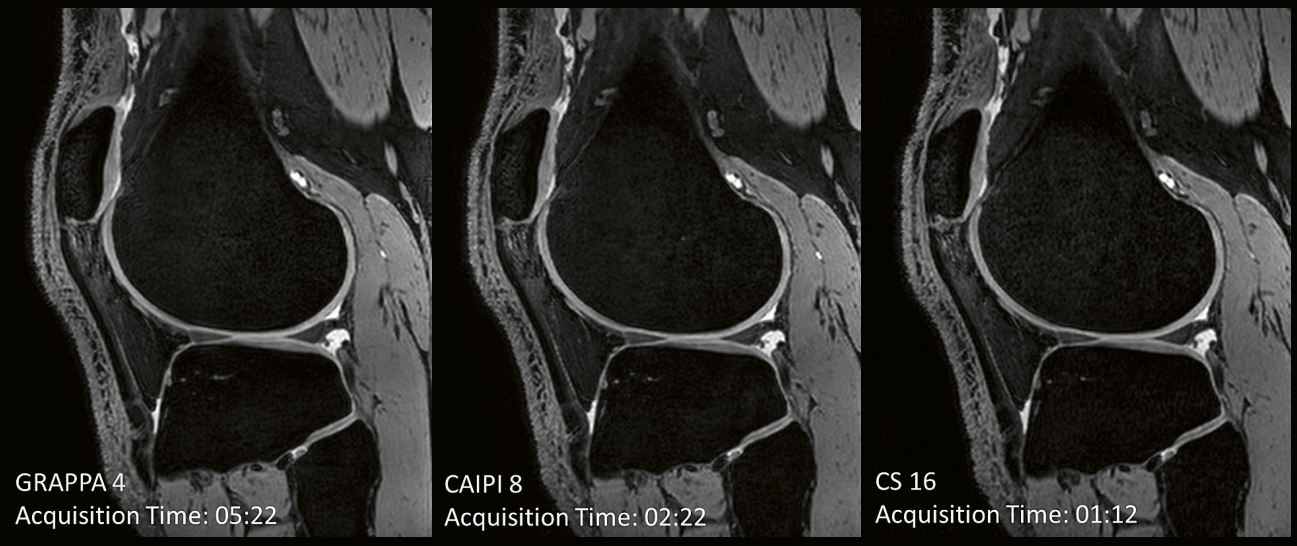

1 Sagittal 3D DESS knee images of a 38-year-old healthy male with 4-fold GRAPPA, 8-fold CAIPIRINHA, and 16-fold Compressed Sensing acceleration. All images are reconstructed using deep learning reconstruction, which, in combination with CS, enables acceleration factors of up to 16-fold at 7T, resulting in an excellent depiction of the knee cartilage. The acquisition time is given in min:sec.

MAGNETOM Prisma (3T); 3D DESS

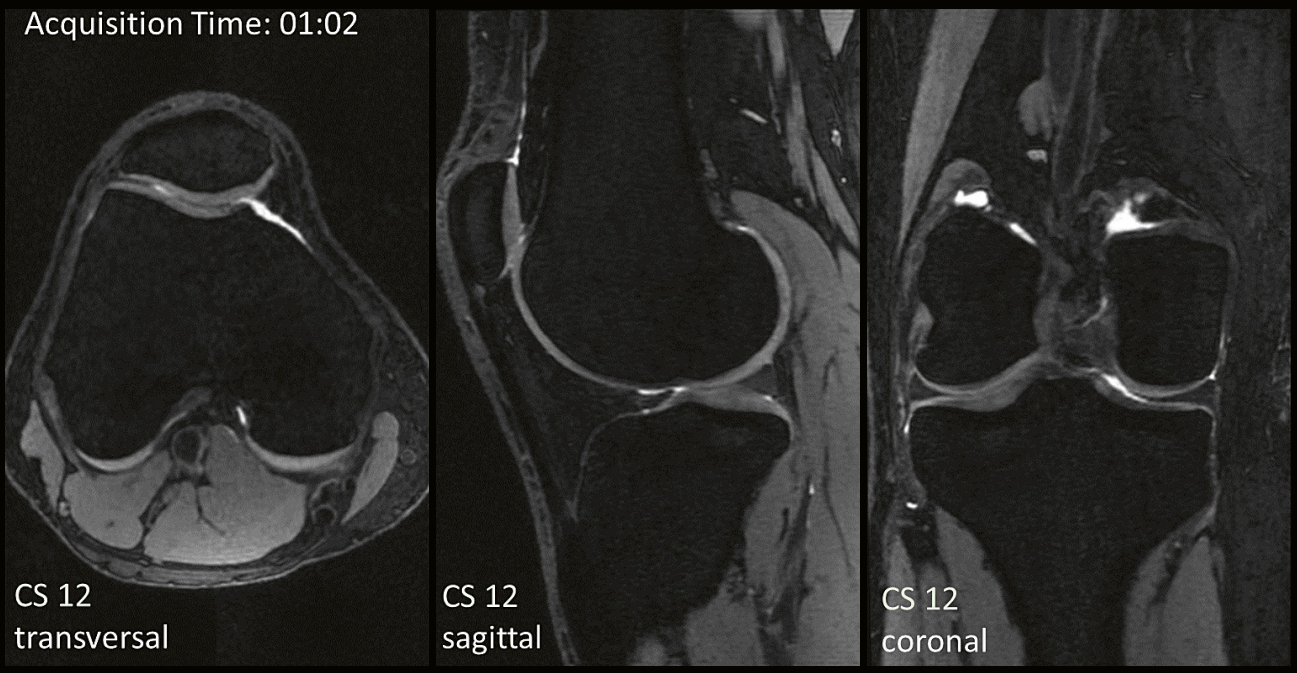

2 3D DESS knee images of a 34-year-old healthy female with 12-fold Compressed Sensing acceleration at 3T field strength. Isotropic data acquisition in the sagittal plane allowed for high-resolution multiplanar reconstruction in the other planes. By employing deep learning reconstruction, these images were feasible at an acquisition time of only 01:02 min.

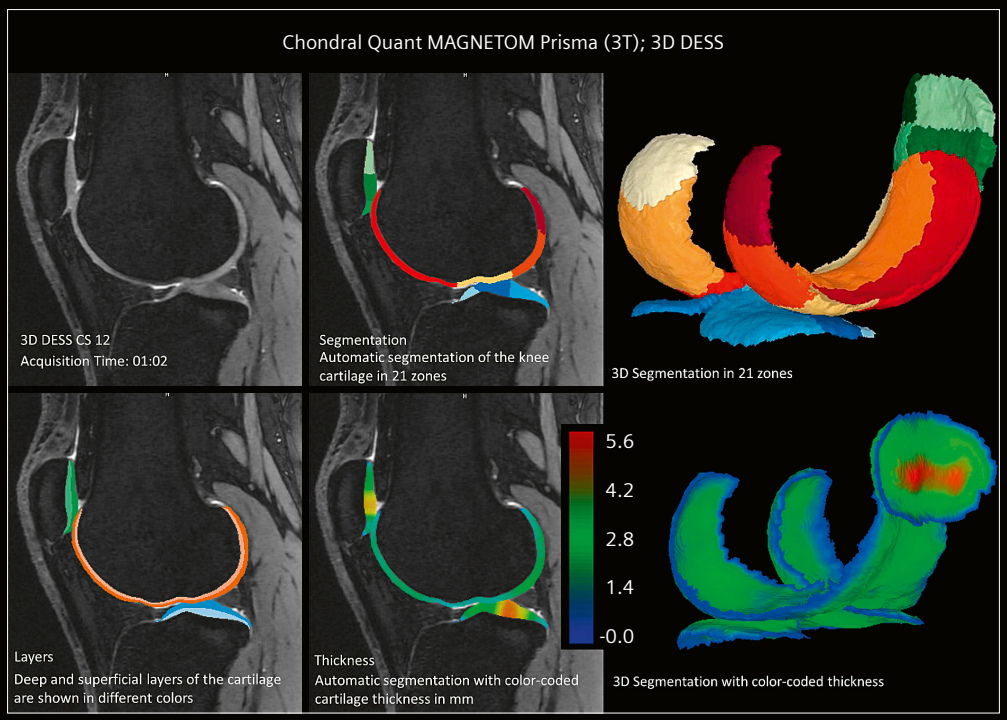

3 Automatic segmentation of knee cartilage on 12-fold Compressed Sensing accelerated 3D DESS images acquired in a 34-year-old healthy female at 3T using Chondral Quant. Acquisition time of the 3D dataset was 01:02 min, with a reconstructed voxel size of 0.3 × 0.3 × 0.3 mm.

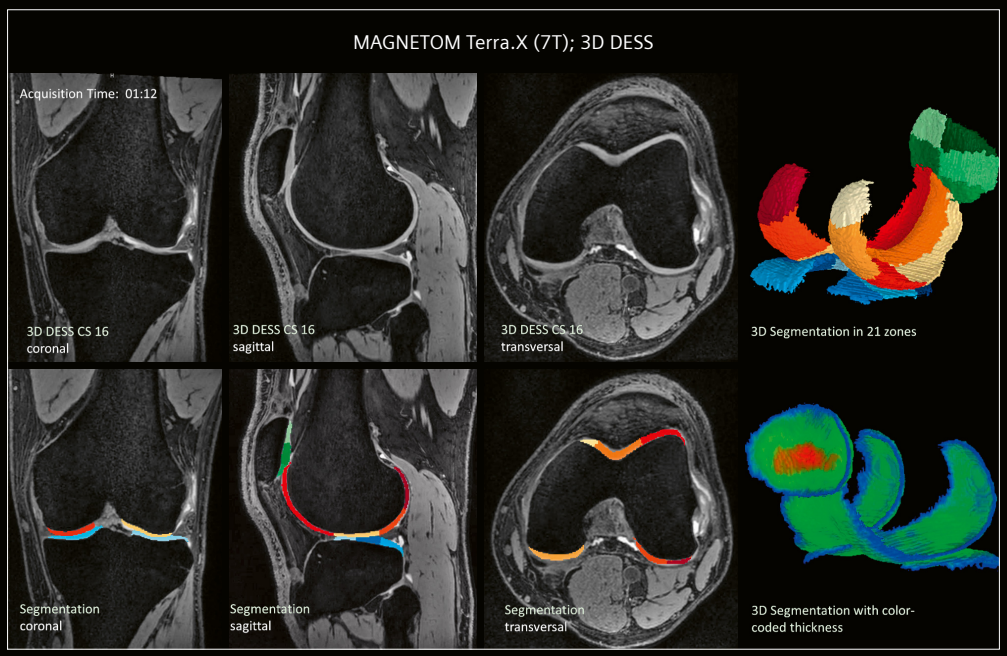

4 Automatic segmentation of the knee cartilage on 16-fold Compressed Sensing accelerated 3D DESS images acquired in a 38-year-old healthy male at 7T using Chondral Quant. Acquisition time of the 3D dataset was 01:12 min, with a reconstructed voxel size of 0.3 × 0.3 × 0.3 mm.

	MAGNETOM Terra.X (7T)			MAGNETOM Prisma (3T)
	GRAPPA × 4	**CAIPIRINHA × 8**	**Compressed Sensing × 16**	**Compressed Sensing × 12**
Acquisition time (min:sec)	05:22	02:22	01:12	01:04
Reconstructed voxel size (mm^3)	0.3 Isotropic	0.3 Isotropic	0.3 Isotropic	0.3 Isotropic
Field of view (mm × mm)	164 × 164	164 × 164	164 × 164	154 × 154
Number of slices	448	448	448	320
Reconstruction matrix size	544 × 544	544 × 544	544 × 544	512 × 512
Base resolution	272 × 272	272 × 272	272 × 272	256 × 256
TR/TE (msec)	10.3/3.00	10.3/3.00	10.3/3.00	12.5/4.30
Flip angle (°)	15	15	15	35
Pixel bandwidth (Hz/Px)	301	301	301	331
Phase/slice oversampling (%)	60 / 14	60 / 14	60 / 14	0 / 50
Fat-water contrast	Water excitation	Water excitation	Water excitation	Water excitation
Phase encoding direction	Head-feet	Head-feet	Head-feet	Anterior-posterior
Orientation of imaging plane	Sagittal	Sagittal	Sagittal	Sagittal

Table 1: Clinical 3D DESS sequence protocols

Conclusion

Deep learning reconstructions enable high acceleration factors for 3D DESS cartilage imaging and allow total acquisition times of approximately one minute [1, 3]. As proof of concept, we acquired similar results in a healthy volunteer at 3T. A detailed evaluation of the DL reconstruction algorithm was recently conducted in a prospective 7T study with 40 knee exams [1]. Given the excellent cartilage contrast, 3D DESS images could serve as an ideal basis for automatic cartilage segmentation in Chondral Quant.

References

1 Marth T, Marth AA, Kajdi GW, Nickel MD, Paul D, Sutter R, et al. Evaluating Undersampling Schemes and Deep Learning Reconstructions for High-Resolution 3D Double Echo Steady State Knee Imaging at 7 T: A Comparison Between GRAPPA, CAIPIRINHA, and Compressed Sensing. Invest Radiol. 2025 Feb 25. Epub ahead of print.

2 Siemens Healthineers Digital Marketplace. Chondral Quant [Internet]. Erlangen, Germany: Siemens Healthineers. [Accessed 2025, March 26]. Available from: https://marketplace.teamplay.siemens-healthineers.com/app/detail/OpenApps-Chondral-Quant?country=gb&language=en&search=chondral%20quant

3 Siemens Healthineers. Musculoskeletal Imaging [Internet]. Zurich, Switzerland : Siemens Healthineers International AG. [Accessed 2025, March 26]. Available from: https://www.siemens-healthineers.com/de-ch/magnetic-resonance-imaging/clinical-specialities/musculoskeletal-imaging

Contact

Thomas Marth, Dr. med. univ.
Swiss Center for Musculoskeletal Imaging
Balgrist Campus AG
Lengghalde 5
8008 Zurich
Switzerland
thomas.marth@balgristcampus.ch

Constantin von Deuster, Ph.D.
Swiss Innovation Hub,
Siemens Healthineers
Freilagerstrasse 40
8047 Zurich
Switzerland
constantin.von_deuster@siemens-healthineers.com

Beyond Limits: Unveiling Clinical Precision in Knee Imaging with 7 Tesla MRI

Bénédicte Delattre[1], Gian Franco Piredda[2], Antoine Klauser[2], Loan Mattera[3], Cédric Garcia[4], Roberto Martuzzi[3], Tom Hilbert[2], Sana Boudabbous[1]

[1]Division of Radiology, Diagnostic Department, Geneva University Hospitals, Geneva, Switzerland
[2]Advanced Clinical Imaging Technology, Siemens Healthineers International AG, Lausanne, Switzerland
[3]Fondation Campus Biotech Geneva, Switzerland
[4]Clinical Education, Siemens Healthineers International AG, Renens, Switzerland

Introduction

Undoubtedly, MRI is the cornerstone for imaging traumatic and degenerative knee conditions. High-field MRI at 3 Tesla has demonstrated improved image resolution, better image quality, and significantly higher diagnostic accuracy for articular cartilage lesion compared to 1.5T systems [1]. Nevertheless, challenges persist in diagnosing partial cruciate ligament injuries, differentiating meniscus tears from signal alterations in normal anatomy, and identifying early cartilage clefts. The advent of ultra-high-field (UHF) MRI at 7T holds promise for addressing these challenges, given its ability to produce higher-resolution images and offer distinct contrasts due to different relaxation time constants. This advancement is promising for both enhancing diagnostic precision and introducing novel applications in knee imaging.

Previous publications have underscored the advantages of UHF in diagnostics [2, 3], leading to recognition by international regulatory bodies through the approval of a clinical 7T system. While UHF imaging offers clear benefits such as higher signal-to-noise ratio (SNR) and spatial resolution, it also presents notable challenges, including coping with increased T1 and reduced T2. While this can be advantageous for enhancing the contrast of specific structures, it generally necessitates longer TR and shorter TE to maintain T1 and T2 weighting. Additionally, it introduces pronounced difficulties in homogenizing B_0 and B_1 radio-frequency fields. However, ongoing research and development has progressively addressed these challenges, rendering 7T increasingly accessible for clinical investigations. A recent comprehensive review extensively details these challenges and proposes strategies for overcoming them in clinical musculoskeletal (MSK) applications [4]. In alignment with the launch of clinical MSK activities at 7T in Geneva, dedicated efforts have been invested into setting up and optimizing morphological sequences using the latest innovations of the MAGNETOM Terra.X.

Concerning protocol optimization, three-dimensional (3D) sequences like proton density (PD) weighted SPACE with fat suppression offer significant advantages in terms of acquisition time and the ability to explore structures across various planes. However, optimizing this sequence for routine clinical use poses a challenge even at conventional clinical fields (1.5T and 3T). Specifically, striking a suitable balance between spatial resolution, acquisition time, and SNR might be challenging. Finally, the integration of Artificial Intelligence (AI) technologies like Deep Resolve Boost and Deep Resolve Sharp in the 2D turbo spin-echo sequences yields substantial benefits, particularly in MSK applications. Incorporating efficient denoising within the reconstruction method alongside enhanced spatial resolution holds tremendous potential for clinical applications. Both of these technologies were explored for knee applications at 7T.

Material and methods

Two healthy volunteers underwent scans at both 3T and 7T to assess the visualization of key knee structures. Table 1 provides a summary of the protocol and sequence parameters used. The knee protocol employed at 3T was tailored for clinical efficiency, aiming for a streamlined workflow of 30 minutes per patient, including setting up the patient and removing them from the scanner. Conversely, at 7T, sequences were optimized to achieve superior spatial resolution while maintaining a favorable SNR. The clinical workflow at 7T allocates approximately 45 minutes per patient, including setting up and removing the patient from the scanner. Neither acquisition time nor spatial resolution were matched between the 3T and 7T protocols, but both were individually optimized considering the clinical workflow and specific needs. During the protocol optimization, challenges were encountered with the 3D sequence PD SPACE with fat suppression. In the previous software version at 3T, this led to increased blurring within the sequence. The development team at Siemens Healthineers have worked over the past years to optimize the refocusing flip angle train, and have effectively resolved this issue. Furthermore, the implementation of the Compressed Sensing acceleration technique has notably improved image quality, enabling higher resolution within a shorter acquisition time. This holds true at 7T, where the sequence could be implemented with an isotropic spatial resolution of 0.25 mm.

3T	Sequence	TE/TR (ms)	parrallel imaging acc. factor	SMS	AI	BW (Hz/px)	slice thickness (mm)	voxel size (recon)	acquisition time
	t1 tse coronal	9.50 / 619	GRAPPA 4	2	DRB + DRS	261	3	0.19 × 0.19	1:04 min
	pd tse sagittal	18 / 3230	GRAPPA 4	no	DRB + DRS	217	3	0.34 × 0.34	1:35 min
	pd space fatsat sagittal	76 / 1100	CS 7.0	NA	NA	401	0.34	0.31 × 0.31	4:49 min
	pd tse fatsat transverse	35 / 6860	GRAPPA 4	no	DRB + DRS	161	3	0.22 × 0.22	1:34 min
	pd tse fatsat coronal	33 / 5910	GRAPPA 4	no	DRB + DRS	162	3	0.22 × 0.22	1:20 min
	pd tse fatsat sagittal	33 / 5910	GRAPPA 4	no	DRB + DRS	162	3	0.22 × 0.22	1:26 min
								TOTAL protocol time (including survey) : 12:02 min	

7T	Sequence	TE/TR (ms)	parrallel imaging acc. factor	SMS	AI	BW (Hz/px)	slice thickness (mm)	voxel size (recon)	acquisition time
	t1 tse coronal	10 / 707	GRAPPA 4	no	DRB + DRS	266	2.5	0.14 × 0.14	2:09 min
	pd tse sagittal	43 / 3900	GRAPPA 4	no	DRB + DRS	249	2.5	0.13 × 0.13	5:35 min
	pd space fatsat sagittal	31 / 900	CS 5.0	NA	NA	401	0.25	0.25 × 0.25	6:35 min
	pd tse fatsat transverse	32 / 4930	GRAPPA 4	no	DRB + DRS	260	1.5	0.16 × 0.16	3:38 min
	pd tse fatsat coronal	21 / 2820	GRAPPA 3	no	DRB + DRS	260	2	0.16 × 0.16	3:38 min
	pd tse fatsat sagittal	43 / 3900	GRAPPA 4	no	DRB + DRS	249	2.5	0.13 × 0.13	5:45 min
								TOTAL protocol time (including survey) : 27:40 min	

Table 1: Protocol and sequence parameters at 3T and 7T.
SMS: Simultaneous Multi-Slice; DRB: Deep Resolve Boost; DRS: Deep Resolve Sharp; CS: Compressed Sensing; fatsat: fat suppression

Image review

In this section, images acquired at 7T are shown, demonstrating general superior image quality and structure conspicuity in comparison to 3T. Emphasis was placed on specific anatomical regions that are notoriously challenging to analyze due to the inherent limitations in visualization at 3T.

1 Patient setup in the 7T MAGNETOM Terra.X scanner using the transmit/receive knee coil. Apart from bore length and scanner size, the setup closely resembles that of a clinical 3T scanner.

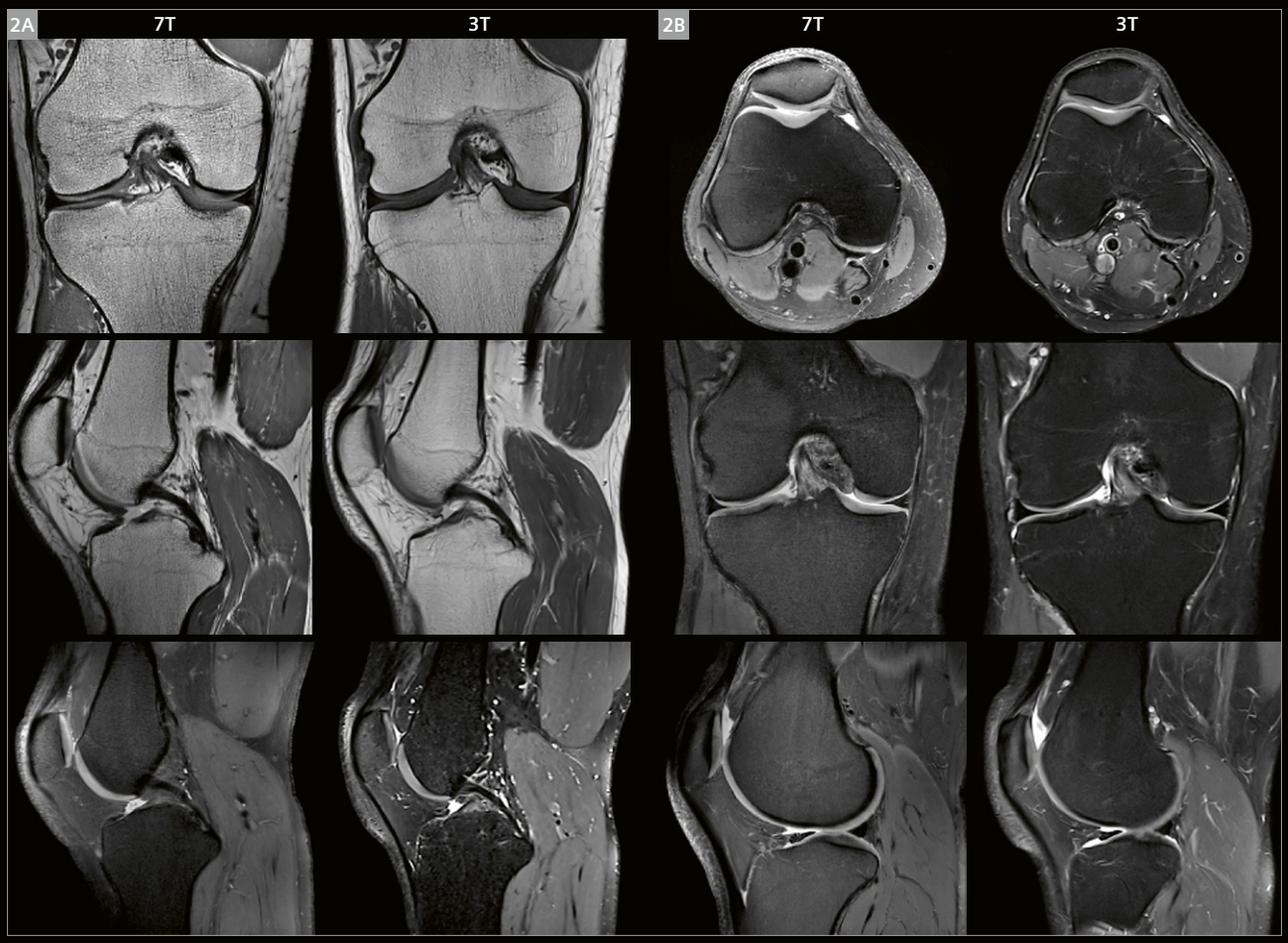

2 Comprehensive knee protocol for a volunteer at 7T and 3T. **(2A)** From top to bottom: T1 TSE coronal, PD TSE sagittal, 3D PD SPACE with fat suppression sagittal. **(2B)** From top to bottom: PD TSE with fat suppression in transverse, coronal, and sagittal orientations. This protocol comparison allows for a direct observation of the resolution enhancement and overall image quality attained at 7T and 3T.

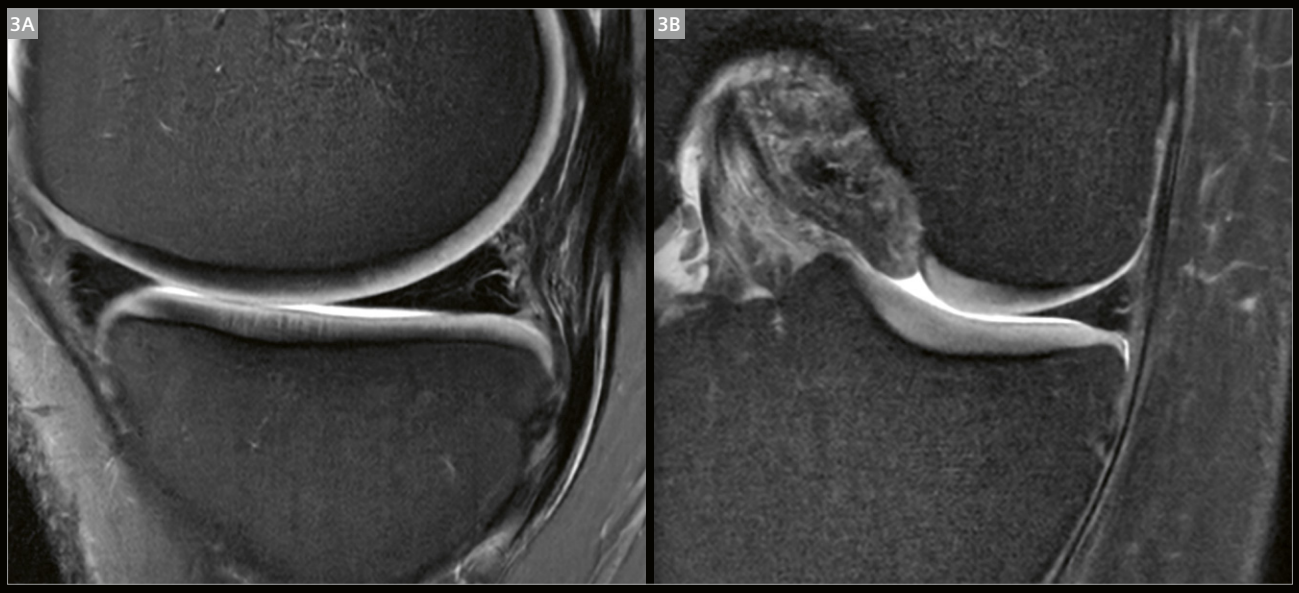

3 General aspect of the meniscus on 7T 2D PD TSE with fat suppression in sagittal **(3A)** and coronal **(3B)** planes.

4 3D PD SPACE with fat suppression at 7T **(4A)** and 3T **(4B)** for the same volunteer, coronal reformat. Meniscus vasculature is more visible at 7T than at 3T, as indicated by the arrow. This addresses a well-known pitfall that often mimics a meniscal tear.

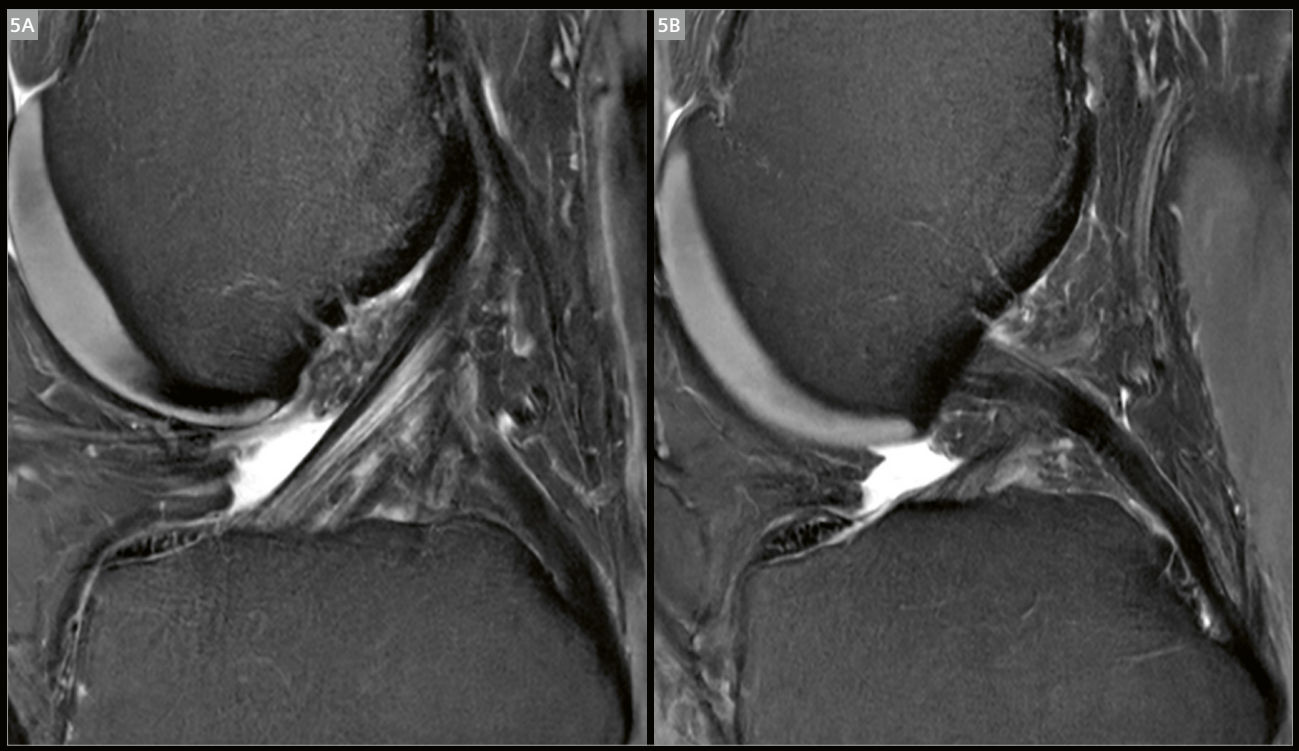

5 Aspect of the anterior **(5A)** and posterior **(5B)** cruciate ligament at 7T for the same volunteer on 2D PD TSE with fat suppression in sagittal plane.

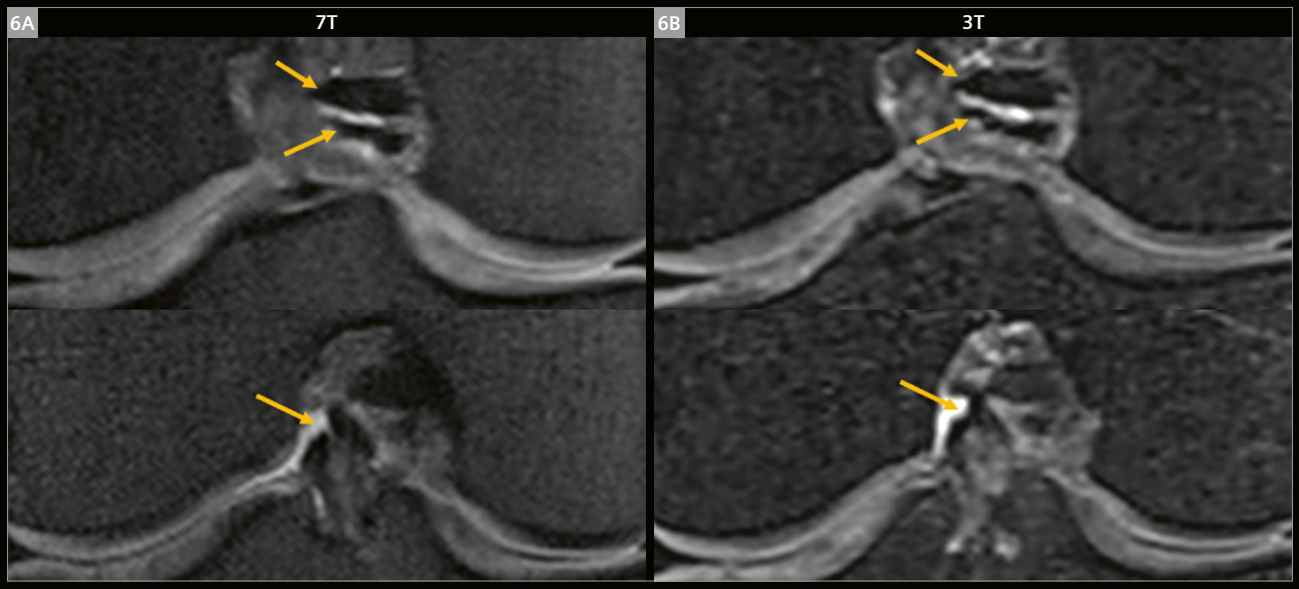

6 3D PD SPACE with fat suppression at 7T (left) and 3T (right) in coronal reformat. In the top row, distinct high-contrast imaging reveals the two bundles of the anterior cruciate ligament (ACL), displaying normal characteristics at 7T, thereby offering a confident diagnosis. In comparison, images obtained at 3T exhibit irregularities and abnormal sizing, contributing to diagnostic uncertainties. On the bottom row, the posterior cruciate ligament (PCL) displays improved conspicuity of its two bundles at 7T compared to 3T. This improved visibility results in greater confidence regarding the ligament's integrity, reducing diagnostic ambiguity.

7 3D PD SPACE with fat suppression at 7T **(7A)** and 3T **(7B)** in coronal reformat. At 7T, the images consistently reveal a homogeneous low signal intensity of the lateral collateral ligament, particularly noticeable at its proximal enthesis. This uniformity is a common imaging challenge on PD FS sequences, as it often resembles a torn ligament. The effect is evident in the 3T images, where the signal appears less homogeneous, further emphasizing the potential for misinterpretation as a ligament tear.

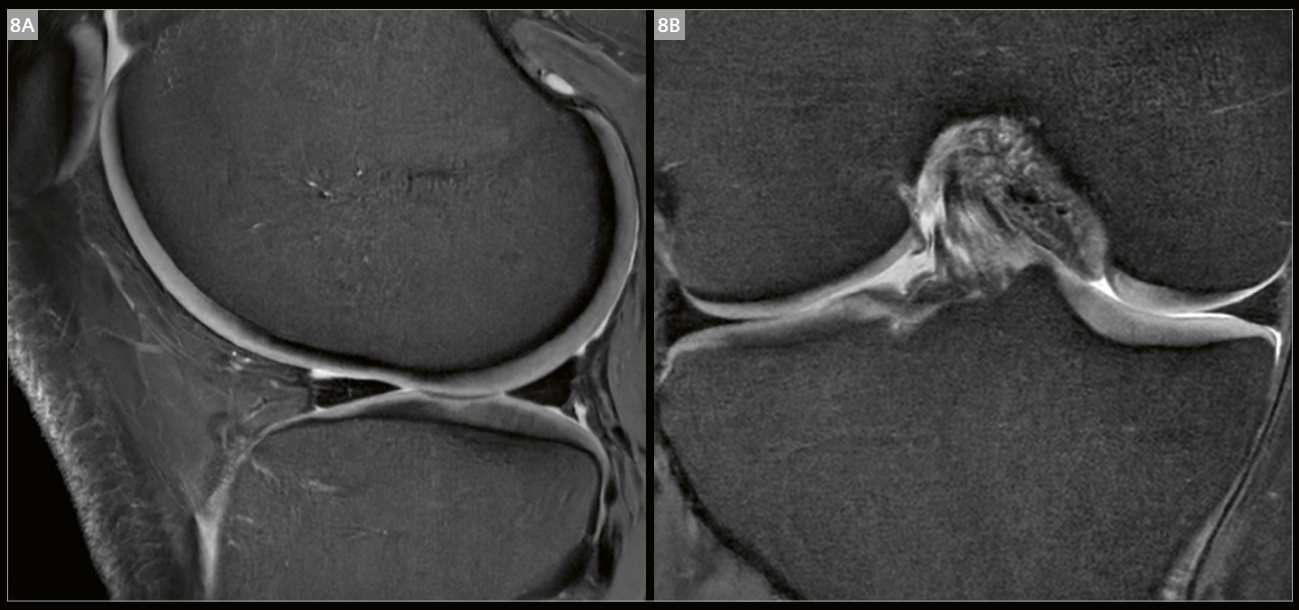

8 2D PD TSE with fat suppression in sagittal **(8A)** and coronal **(8B)** planes at 7T, showing the general aspect of the cartilage in different planes.

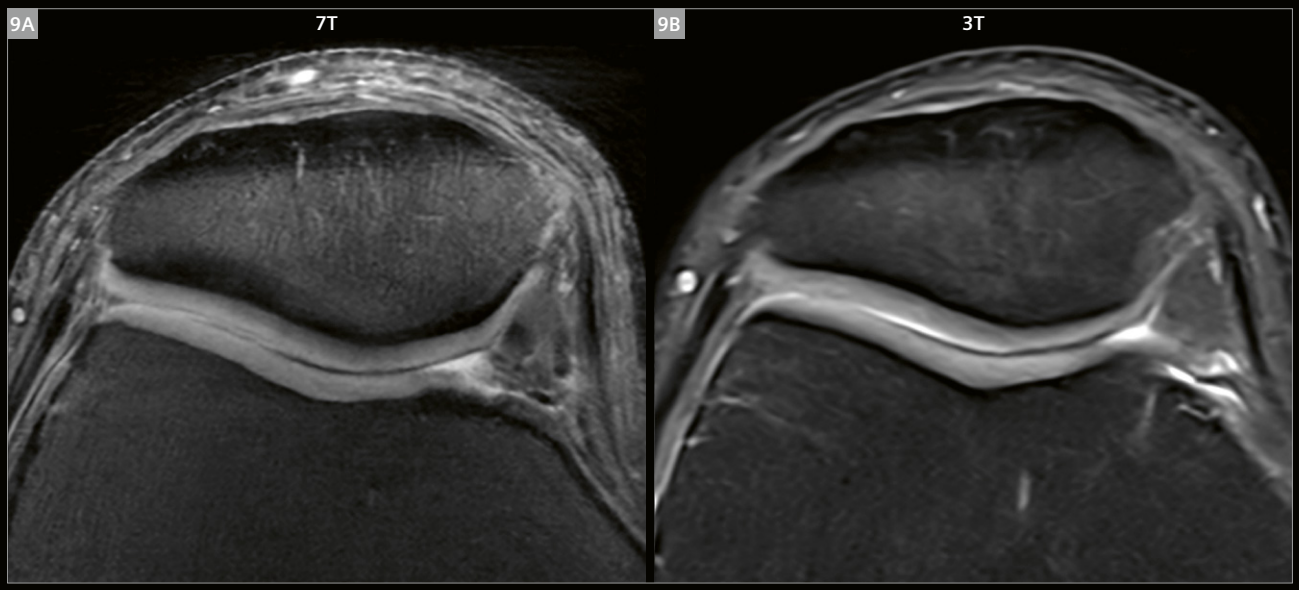

9 2D PD TSE with fat suppression in transverse plane at 7T **(9A)** and 3T **(9B)** for the same volunteer. The assessment of the patellofemoral cartilage exhibits high accuracy, characterized by a uniform signal without indications of chondromalacia in this region. While the 3T images maintain sufficient quality, a distinct advantage in confidence arises from the signal homogeneity observed in the 7T images.

Conclusion and perspectives

Using tailored imaging sequences in an ultra-high-field setting notably enhances resolution, providing greater confidence for the anatomical assessment of the knee. The incorporation of 3D sequences further addresses common pitfalls encountered in routine scans at 3T and 1.5T. Optimizing the protocol with the latest AI developments, such as the Deep Resolve options, facilitates the acquisition of high-quality sequences within a reasonable time frame.

References

1 Cheng Q, Zhao FC. Comparison of 1.5- and 3.0-T magnetic resonance imaging for evaluating lesions of the knee: A systematic review and meta-analysis (PRISMA-compliant article). Medicine (Baltimore). 2018;97(38):e12401.

2 Juras V, Mlynarik V, Szomolanyi P, Valkovič L, Trattnig S. Magnetic Resonance Imaging of the Musculoskeletal System at 7T: Morphological Imaging and Beyond. Top Magn Reson Imaging. 2019;28(3):125–135.

3 Aringhieri G, Zampa V, Tosetti M. Musculoskeletal MRI at 7T: do we need more or is it more than enough? Eur Radiol Exp. 2020;4(1):48.

4 Pazahr S, Nanz D, Sutter R. 7 T Musculoskeletal MRI: Fundamentals and Clinical Implementation. Invest Radiol. 2023;58(1):88–98.

Contact

Sana Boudabbous, M.D., Ph.D.
Division of Radiology
Department of Imaging
and Medical Informatics
Geneva University Hospitals
Rue Gabrielle-Perret-Gentil 4
1211 Geneva 14
Switzerland
Tel: +41 79 553 42 22
Sana.Boudabbous@hcuge.ch

What happens when you have an MRI scan?

Help your little patients lose their fear – with Lottie

Lottie is an adventurous little lamb that loves to skateboard. But poor Lottie had an accident and may have broken her ankle. Now instead of leaping, she can only limp. Lottie is off to the hospital for an MRI scan. This engaging story by Professor Rolf Vosshenrich and Sylvia Graupner explains to children what it's like to have an MRI scan in a way they can understand.

We offer Lotti's story as a children's book in 19 languages (PDF) and as video in 6 languages. You can also order hard copies of the book in German, English, and Spanish.

The material is available at
www.siemens-healthineers.com/magnetom-world

Go to **> Publications > MR Basics**

From Concept to Deployment: A Deep Learning Model for Lumbar Spinal Stenosis at National University Hospital in Singapore

James Hallinan[1], Beng Chin Ooi[2], Jonathan Jiong Hao Tan[1], Stefan Huwer[3], Sai Sharath Hakeen[3], Benjamin Schmitt[3], Heiko Meyer[3], Andrew Makmur[1]

[1]Department of Diagnostic Imaging, National University Hospital, Singapore
[2]National University of Singapore
[3]Siemens Healthineers

Introduction

Lumbar spinal stenosis (LSS) is one of the most common degenerative conditions in adults, with around 200,000 individuals diagnosed annually in the United States [1–3]. Given the pivotal role of magnetic resonance imaging (MRI) in diagnosing and grading LSS, radiologists must routinely evaluate multiple lumbar levels to check for narrowing at the spinal canal, lateral recesses, and neural foramina. Despite the critical role of MRI, reporting LSS remains a time-intensive, repetitive task for radiologists, often compounded by poor interobserver agreement in stenosis grading. Recognizing these challenges, a multidisciplinary team from the National University Hospital (NUH) in Singapore, the National University of Singapore (NUS), and external collaborators set out to develop a deep learning (DL) solution (Spine AI)[1] aimed at streamlining LSS evaluation.

[1]MR Lumbar Spine AI is currently under development and not commercially available. It is for research use only. Not for clinical use. It is not for sale in the USA and its future availability cannot be ensured.

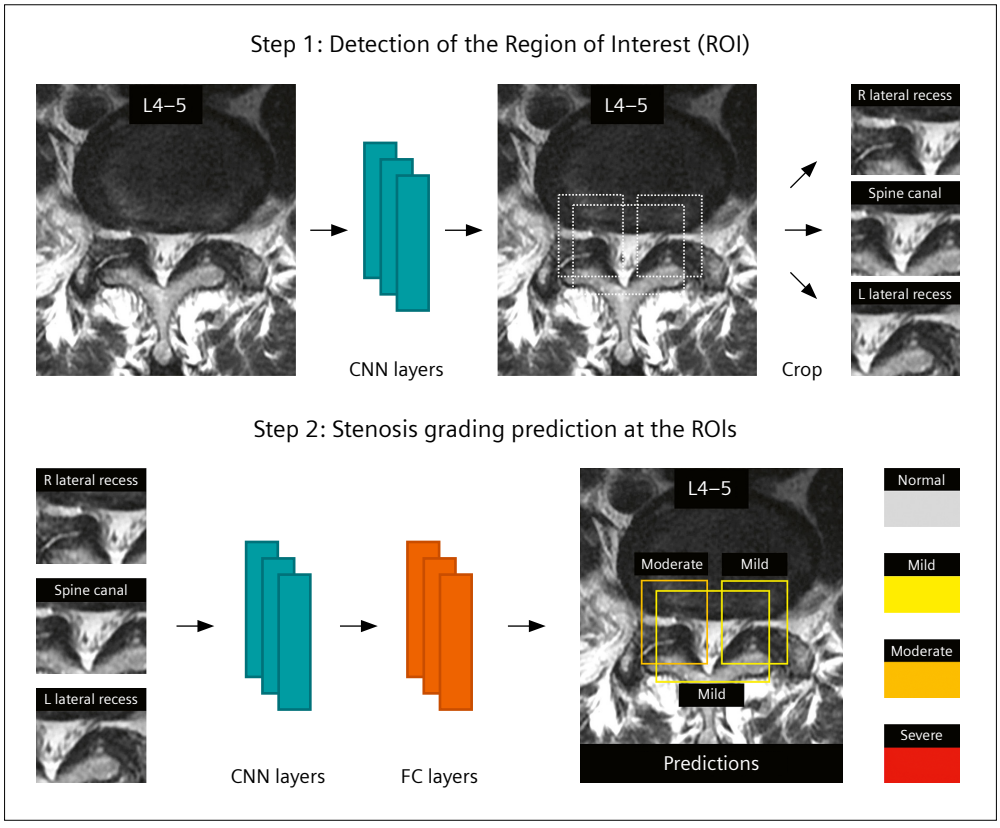

1 Architecture of the CNN-based models for lumbar stenosis. Step 1 involves a CNN that detects the ROI. Step 2 applies another CNN to classify stenosis severity, as illustrated here for the spinal canal and bilateral lateral recesses at the L4–L5 level. Abbreviations: CNN: convolutional neural network, ROI: region of interest, FC: fully connected, R: right side, L: left side

Motivation behind the project

The project was born from the clinical realities faced by our radiology department at NUH, where a typical Monday morning could see over 50 lumbar spine MRIs queued for reporting. The tedious nature of detailing stenosis at the spinal canal, lateral recesses, and neural foramina inspired us to explore whether DL could semi-automate this process and thereby reduce variability and achieve time savings. Additionally, prior studies had demonstrated promise in applying DL to lumbar spine MRI, but none had comprehensively addressed all three regions of interest (ROIs) or integrated explainable outputs to aid radiologists [4, 5].

The development of the Spine AI model was made possible through a multidisciplinary collaboration that included radiologists, computer scientists, and clinicians. Key contributors included Professor Beng Chin Ooi's computer science team at NUS, whose work in advanced machine learning helped refine the AI architecture. The first step in development was securing institutional ethics approval, which paved the way for collecting high-quality imaging data across a range of vendor platforms to create a generalizable DL solution.

Development of the deep learning model

Our initial technical study on the LSS model was published in *Radiology* in 2021 [6]. Over a three-year period (September 2015 to September 2018), the team extracted 446 lumbar spine MRI studies for DL model training and testing. Exclusions included studies with spinal instrumentation, scoliosis, suboptimal image quality, and post-gadolinium sequences. Axial T2-weighted images were used for assessing the spinal canal and paired lateral recesses, while sagittal T1-weighted images were used for analyzing the paired neural foramina. The dataset was split into an internal training set (80%), a validation set (9%), and a test set (11%). External validation included a dataset of 100 lumbar spine MRI studies from Saudi Arabia, to assess the model's generalizability across geographic regions.

Four radiologists with subspecialty expertise in spine imaging (musculoskeletal radiologists and neuroradiologists with 2–9 years of experience) labelled the training data using bounding box annotations. This supervised labelling ensured high-quality inputs for model training. When drawing each bounding box at the region of interest, the radiologist classified stenosis on axial and sagittal MRI based on established criteria and visual scales for the spinal canal [7–9], lateral recesses [10], and neural foramina [7]. Overall, stenosis was categorized into four clinical grades: normal, mild, moderate, and severe. These corresponded to stenosis of 0, < 1/3, 1/3–2/3, and > 2/3 of the normal diameter, respectively. We decided not to use more granular quantitative measures, as these are not typically used in clinical practice [11].

The developed DL model consisted of two main convolutional neural networks (CNN). The first CNN was tasked with localizing ROIs: the spinal canal, bilateral lateral recesses, and neural foramina. The second CNN performed the actual stenosis classification, assigning each region to one of four severity grades (normal, mild, moderate, or severe). This approach bypassed the pitfalls of relying on unstructured radiology reports by requiring high-quality annotated datasets (Fig. 1).

Performance evaluation

The performance of the DL model was evaluated using both an internal test set at NUH (50 cases) and an external test set of 100 lumbar spine MRI studies provided by a collaborator in Saudi Arabia. The internal test set was labelled by a senior musculoskeletal (MSK) radiologist, Professor Hiroshi Yoshioka, who has over 30 years of experience and served as the reference standard. Two subspecialist radiologists, a neuroradiologist with five years of experience and an MSK radiologist with nine years of experience, also labelled the test dataset to enable comparison with the DL model.

When detecting ROIs, the DL model achieved recall rates exceeding 99% for the spinal canal and over 95% for the lateral recesses, which closely matched the performance of the subspecialist radiologists. For the neural foramina, the DL model's recall was 84.5%, comparable to one of the radiologist's recall at 83.9%. This slightly lower performance in foraminal detection likely reflects the challenge posed by less distinct anatomical borders between the foramina, the spinal canal, and the paravertebral region.

Interobserver agreement for stenosis classification was calculated using Gwet's kappa (AC1), which took into account the higher prevalence of normal classifications in the dataset. Under a dichotomous classification scheme (normal/mild versus moderate/severe), the central canal demonstrated almost perfect agreement, with kappa values of 0.98 for both radiologists and 0.96 for the DL model. For the lateral recesses, the model achieved a kappa value of 0.92, aligning with one radiologist's score and slightly lower than the 0.95 for the other radiologist. Neural foraminal agreement for the model was 0.89, which was slightly reduced compared to the subspecialist radiologists' kappa values of 0.95 and 0.94. Notably, on the external test set, the model's performance for the neural foramina improved to 0.96, accompanied by high agreement for the central canal (0.95) and lateral recesses (0.96). This strong performance on external testing suggested the model's potential for broader application across different populations and imaging protocols.

This initial article showed promising results and was accompanied by an editorial in *Radiology* by Professor

Hayashi (2021), which underscored the importance of further evaluating clinical utility [12]. While recognizing the model's technical success, Professor Hayashi stressed the need for studies assessing how AI assistance might reduce interpretation times, standardize reporting, and reduce variability among radiologists. For our team, these insights served as a roadmap for further development and assessment of the DL model.

Clinical validation and key findings

The potential clinical impact of the Spine AI DL model was evaluated in a second study in *Radiology* in 2022, which focused on the model's ability to improve productivity and consistency among radiologists reporting lumbar spine MRI studies [13]. In this retrospective study, eight radiologists with experience ranging from 2 to 13 years (in-training and attending radiologists) interpreted lumbar spine MRI studies both with and without AI assistance. A cross-over design with a one-month washout period was used to minimize learning or recall bias. As before, the radiologists assessed stenosis at three key regions along the lumbar spine: the spinal canal, lateral recesses, and neural foramina. The evaluation included both reporting time and interobserver agreement, using a reference standard which was again provided by Professor Yoshioka, an external MSK radiologist with over 30 years of experience.

The results demonstrated a significant reduction in reporting time when AI assistance was used. On average, interpretation time decreased from around 2–4.5 minutes (124–274 seconds) without AI to 1 minute or less (47–71 seconds) with AI ($P < 0.001$). These time savings were most marked for general and in-training radiologists, who appeared to benefit the most from the automated stenosis gradings and bounding box visualizations provided by the Spine AI model. Specifically, musculoskeletal radiologists reduced their mean reporting time from 124 ± 25 seconds to 47 ± 24 seconds (a 62% decrease), general radiologists cut their time from 226 ± 61 seconds to 70 ± 29 seconds (a 69% decrease), and in-training radiologists experienced the greatest drop, declining 74% from 274 ± 88 seconds to 71 ± 28 seconds (Table 1).

In addition to improved efficiency, the AI model enhanced the consistency of stenosis grading for non-specialist radiologists (Table 1). General and in-training radiologists demonstrated marked improvements in interobserver agreement for four-class neural foraminal stenosis when using AI assistance, with Gwet's kappa values increasing from 0.39 (without AI) to 0.70–0.71 (with AI). For other stenosis gradings, AI-assisted radiologists achieved either superior or equivalent interobserver agreement compared to unassisted interpretations. These findings highlighted the DL model's ability to bridge the gap in performance between specialist and non-specialist radiologists.

Transition to clinical deployment: The *syngo*.via Frontier platform from Siemens Healthineers

Having established both the technical feasibility and clinical benefits, the team turned its attention to deployment of the Spine AI model. In November 2023, a technology development agreement (TDA) was signed by NUH, NUS, and Siemens Healthineers to integrate the Spine AI model into the *syngo*.via Frontier platform as a research application (MR Lumbar Spine AI[1]) which will be made available in the marketplace. This marked the most exciting phase in the project so far, effectively taking the DL model from bench to bedside. As many radiologists are aware, seamlessly incorporating a DL model into routine workflows is no simple task, and involves close engineering collaboration, robust user-interface and user-experience (UI/UX) development, and alignment with clinical safety and security protocols.

Collaboration with Siemens Healthineers was essential for providing key advancements in the overall performance

Radiologist Group	Reading Time (sec)		Time saved (%)	Neural foramina (κ)	Lateral recess (κ)	Spinal canal (κ)
	Without DL	With DL		Without DL → With DL		
MSK	124 ± 25	47 ± 24	62	0.83 → 0.87	0.81 → 0.78	0.86 → 0.85
General	226 ± 61	70 ± 29	69	0.71 → 0.87	0.68 → 0.76	0.74 → 0.84
In-training	274 ± 88	71 ± 28	74	0.71 → 0.88	0.65 → 0.77	0.85 → 0.80

Table 1: Summary of mean interpretation times and two-class interobserver agreement for MRI lumbar spine stenoses with and without DL model support
Note: Reading time is presented as mean ± standard deviation, and time saved (%) reflects the reduction in mean reporting time. Gwet's kappa (κ) values indicate interobserver agreement for two-class stenosis grading (normal/mild versus moderate/severe) without → with DL assistance.

of the lumbar spine DL model regarding their use in a clinical setting: vertebral disc level detection was developed and is now robust, ensuring the correct levels are identified for accurate autoreport generation of stenosis gradings. Using the AutoAlign Spine technology for the MRI scan, can further improve the accuracy of the vertebral disc level detection. The engineers at Siemens Healthineers also helped refine features, such as presenting bounding boxes only at the most prominent levels of stenosis at each ROI, thus reducing clutter and focusing the radiologist's attention where it matters most.

The lumbar Spine AI application is now available as a research prototype[1] on *syngo*.via Frontier. The automatic processing involves carefully mapping MRI sequences to the model's input requirements. When a lumbar spine MRI study is opened, the system automatically identifies axial T2-weighted and sagittal T1-weighted images, then applies the AI algorithms in the background. Color-coded bounding boxes corresponding to different stenosis severities are subsequently overlaid on each relevant level of the lumbar spine. These results are stored in the form of grayscale presentation state overlays on the source images. The model also generates an automated summary report, which radiologists can review and edit. This can be output as either a DICOM structured report or a DICOM-encapsulated PDF, both of which are designed to merge smoothly into existing radiology information systems. Automated reports, bounding boxes, and stenosis grading examples are provided in Figures 2–4, which show a full range of stenosis gradings, even on a background of scoliosis.

At NUH, deployment of the Spine AI model on *syngo*.via and prospective evaluation are now taking place. *syngo*.via has been installed on all radiologists' desktops, allowing for the incorporation of Spine AI into routine reporting workflows. The Spine AI clinical innovation and deployment has also been supported by multiple grants from the National Medical Research Council (NMRC), including the New Investigator Grant and Clinical Innovator Awards, and it has been recognized through the Practice Changing Innovations Award (NUH and Ministry of Health, Singapore).

2A

Spine AI report

At T11-T12 there is mild spinal canal, no bilateral recess stenosis. There is no right and mild left neural foraminal stenosis.
At T12-L1 there is mild spinal canal, mild bilateral recess stenosis.
At L1-L2 there is moderate spinal canal, severe right and moderate left lateral recess stenosis.
At L2-L3 there is moderate spinal canal, no right and mild left lateral recess stenosis. There is moderate right and no left neural foraminal stenosis.
At L3-L4 there is no spinal canal, mild right and severe left lateral recess stenosis. There is severe right and no left neural foraminal stenosis.
At L4-L5 there is severe spinal canal, severe bilateral recess stenosis. There is moderate right and severe left neural foraminal stenosis.
At L5-S1 there is mild spinal canal, mild right and moderate left lateral recess stenosis. There is mild right and severe left neural foraminal stenosis.

Report based on automated processing!
Research only, Not for clinical use

Input Data:
5 SAG T1
7 AX T2 TOP
8 AX T2 MID
9 AX T2 BOT

2B

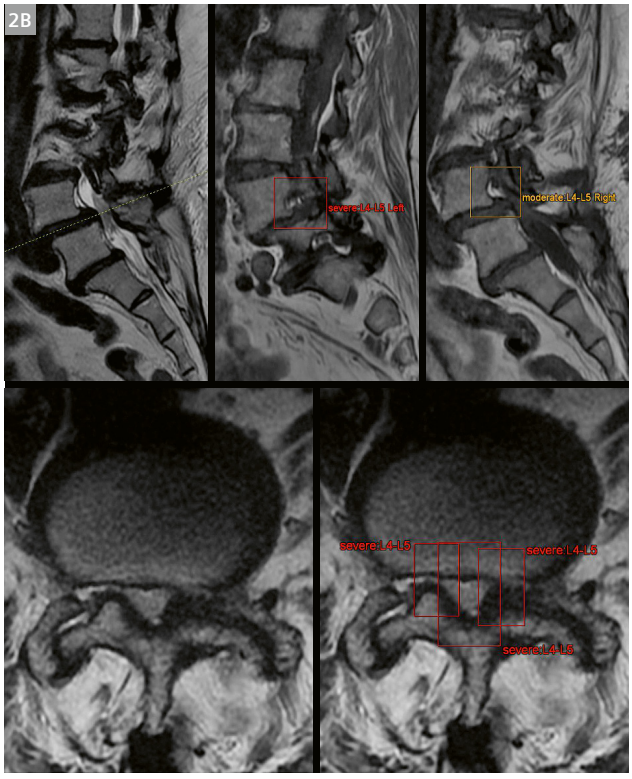

2 Spine AI predictions for Patient 1, a 70-year-old woman with back pain and bilateral lower limb radiculopathy. The assessment was limited by scoliosis, although the most severe stenoses in the lower lumbar spine from L3 to S1 were detected and classified correctly. An autogenerated Spine AI report is shown in Figure **(2A)**. In Figure **(2B)**, the top left is a sagittal T2-weighted image showing the scoliosis and spinal deformity with a cross-reference line at L4–5. Sagittal T1-weighted images are provided in the top row and show neural foramina stenosis gradings. Axial T2-weighted images are provided in the bottom row and show the paired lateral recesses and central spinal canal stenosis gradings at L4–5.

Future directions: Expanding capabilities and exploring new frontiers

While the deployment of the Spine AI model is a significant achievement, there is great potential for further development. Future work aims to expand the model beyond stenosis grading to include other pathologies such as spondylolisthesis, fractures, and disc disease. Additionally, the team plans to extrapolate its application to other regions, such as the cervical spine[2] [14], and explore the deployment of additional tools for detecting spinal metastases[2] and early epidural spinal cord compression[2] on MRI and CT imaging, supported through the New Investigator Grant and Clinical Innovator Award from the National Medical Research Council [15–18]. Initial work on these fronts has already been presented at national and international conferences, including the European Society of Skeletal Radiology (ESSR) conference in 2024 and the Global Spine Congress (GSC) in 2023.

[2]*The product/features (mentioned herein) are not commercially available. Their future availability cannot be guaranteed.*

Building on the success of the lumbar spine work, the group recently introduced a DL model for degenerative cervical spondylosis in The Spine Journal in 2024 [14]. This transformer-based model was trained on MRI data from 454 patients at NUH, and tested on an internal dataset of 50 patients and an external dataset of 100 patients from Ng Teng Fong General Hospital (NTFGH), Singapore. The model demonstrated excellent performance in classifying stenosis at each cervical disc, achieving near-perfect binary classification (normal/mild versus moderate/severe) agreement for spinal canal ($\kappa = 0.95$) and neural foraminal stenosis ($\kappa = 0.90$). Its sensitivity and specificity ranged from 83.7% to 92.4% and from 87.8% to 98.3%, respectively, across both datasets. In addition, it outperformed radiologists in grading spinal canal ($\kappa = 0.78$ vs. $\kappa = 0.57–0.70$) and neural foraminal stenosis ($\kappa = 0.80$ vs. $\kappa = 0.63–0.69$), with high recall for cord signal abnormalities (92.3%). These results highlight the potential of the cervical spine model to improve the efficiency and consistency of reporting. The model is now being assessed in a study where radiologists perform stenosis assessment with and without DL assistance [14, 19]. This initial work on a deep

3A

Spine AI report

At T12-L1 there is no spinal canal or lateral recess stenosis. There is no neural foraminal stenosis.
At L1-L2 there is mild spinal canal, no bilateral recess stenosis. There is no neural foraminal stenosis.
At L2-L3 there is mild spinal canal, no bilateral recess stenosis. There is no neural foraminal stenosis.
At L3-L4 there is severe spinal canal, moderate bilateral recess stenosis. There is no neural foraminalstenosis.
At L4-L5 there is severe spinal canal, severe bilateral recess stenosis. There is no right and mild left neural foraminal stenosis.
At L5-S1 there is moderate spinal canal, severe bilateral recess stenosis. There is moderate right and mild left neural foraminal stenosis.

Report based on automated processing!
Research only, Not for clinical use

Input Data:
5 SAG TI
7 AX T2 TOP
8 AX T2 MID
9 AX T2 BOT

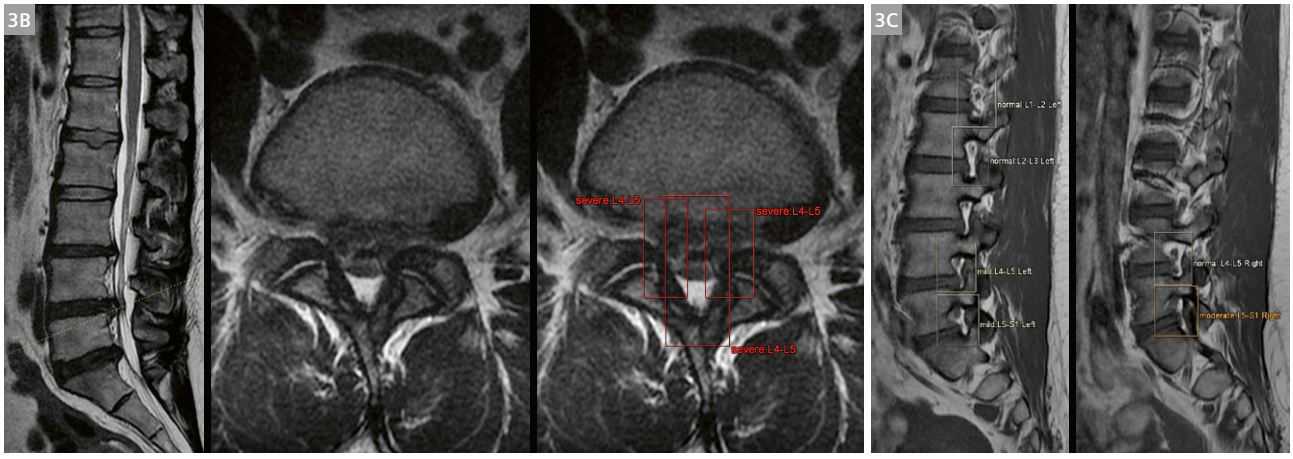

3 Spine AI predictions for Patient 2, a 36-year-old woman with back pain and suspected lumbar spinal stenosis. An autogenerated Spine AI report is shown in Figure **(3A)**. In Figure **(3B)**, a sagittal T2-weighted image is shown for orientation with a cross-reference line at L4–L5. Stenosis predictions are provided, with severe stenoses at the spinal canal and lateral recesses, mainly due to a large disc protrusion. Figure **(3C)** shows sagittal T1-weighted images with bounding boxes and stenosis gradings along the bilateral neural foramina, with a nice example of moderate right neural foraminal stenosis at L5–S1.

learning model for MRI cervical spine assessment won a best abstract award at the Royal College of Radiologists (RCR) and NHS Global AI Conference 2025.

Perhaps the most exciting future work is uniting cervical and lumbar models with new thoracic-level algorithms to detect stenoses and spinal cord compression, yielding a unified, whole-spine solution[2]. Such an approach would integrate degenerative pathology detection with oncological assessments for metastatic spinal disease, resulting in a single DL pipeline that offers comprehensive coverage from the cervical to the lumbar region. This is a key aim within the NMRC Clinical Innovator Award, and the team believes it could deliver a greater impact that extends beyond the current lumbar spinal stenosis model [19].

An additional frontier in our team's clinical innovation lies in exploring large language models (LLMs) within radiology. LLMs have great potential to significantly reduce administrative burdens for radiologists by automating tasks such as vetting imaging requests, scheduling appointments and optimizing reporting [20, 21]. Combined with existing clinical data in electronic medical records, prior imaging findings, and AI-generated assessments (e.g., stenosis gradings from the Spine AI model), LLM-based systems could create more comprehensive and context-aware radiology reports. Integrating image-based and language-based AI would make it possible to further boost productivity, ensure more consistent reporting, and ultimately improve patient care with outputs that are both clinically relevant and seamlessly integrated into the radiology workflow [22].

Conclusion

The journey from developing an AI-based standalone solution for lumbar spinal stenosis to seamlessly integrating it into the clinical workflow illustrates how research, clinical expertise, and industrial collaboration can align to transform clinical care. The DL model created at NUH and NUS has already shown benefits in boosting radiologist productivity, cutting reporting times, and improving the consistency of stenosis gradings. However, these achievements are just the start. As the model evolves and gains more features – such as detecting additional spinal pathologies, analyzing the cervical spine, and identifying metastatic lesions – AI-based tools are poised to become indispensable in everyday radiology. The successful deployment of the Spine AI model as a research application on

4A

Spine AI report

At T12-L1 there is no spinal canal or lateral recess stenosis. There is no neural foraminal stenosis.
At L1-L2 there is no spinal canal or lateral recess stenosis. There is no neural foraminal stenosis.
At L2-L3 there is no spinal canal, no right and mild left lateral recess stenosis. There is no right and left neural foraminal stenosis.
At L3-L4 there is no spinal canal, mild right and no left lateral recess stenosis. There is mild bilateral neural foraminal stenosis.
At L4-L5 there is mild spinal canal, moderate right and mild left lateral recess stenosis. There is mild bilateral neural foraminal stenosis.
At L5-S1 there is mild spinal canal, no bilateral recess stenosis. There is mild right and no left neural foraminal stenosis.

Report based on automated processing!
Research only, Not for clinical use

Input Data:
5 SAGTI
7 AX T2 TOP
8 AX T2 MID
9 AX T2 BOT

4B

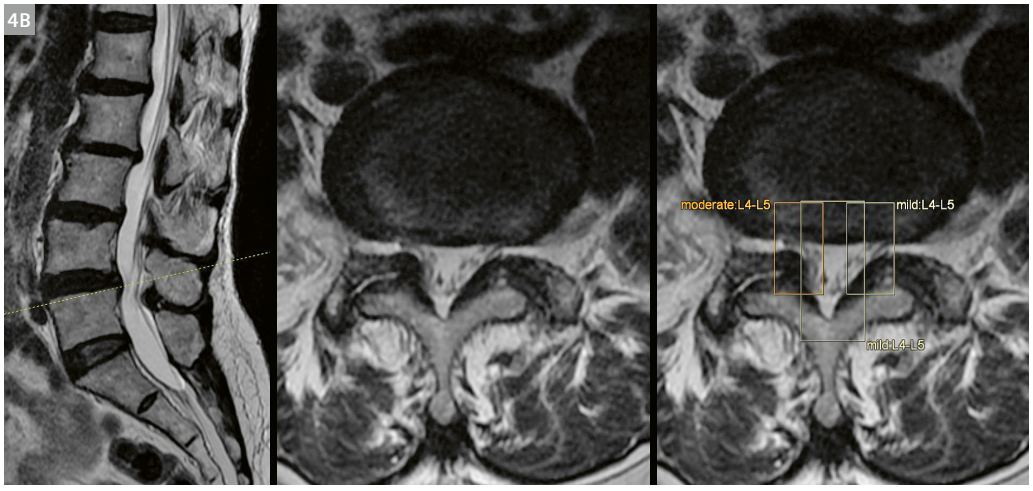

4 Spine AI predictions for Patient 3, a 66-year-old woman with back pain and bilateral L5 radiculopathy with right L5 weakness. An autogenerated Spine AI report is shown in Figure **(4A)**. In Figure **(4B)**, a sagittal T2-weighted image is shown for orientation with a cross-reference line at L4–L5. Stenosis predictions are provided, with a nice example of moderate lateral recess stenosis on the right side at L4–5 due to facet joint arthropathy and ligamentum flavum thickening. This impinges on the traversing right L5 nerve root in the lateral recess, compatible with the clinical history.

syngo.via Frontier, backed by a technology development agreement, highlights the practical application of academic AI research in everyday clinical practice and paves the way for further interdisciplinary efforts to improve patient care.

Acknowledgments

The Spine AI model development was supported by direct funding from the Singapore Ministry of Health (MOH) and the National Medical Research Council (NMRC). Specifically, it is supported under the NMRC Clinician Innovator Award (CIA) with the grant titled Deep Learning Pipeline for Augmented Reporting of MRI Whole Spine (Grant Number: CIAINV23jan-0001, MOH-001405) awarded to J.T.P.D.H. The deployment and adoption of Spine AI model is funded and supported by Singapore National University Health System (NUHS) Flagship Practice Changing Innovations (PCI) Programme.

References

1 Lurie J, Tomkins-Lane C. Management of lumbar spinal stenosis. BMJ. 2016;352:h6234.
2 Epidemiology and Disease Control Division, Ministry of Health, Singapore. National Health Survey 2010. Available at: https://www.moh.gov.sg/others/resources-and-statistics/reports-national-health-survey-2010. Accessed September 22, 2020.
3 See QY, Tan JB, Kumar DS. Acute low back pain: diagnosis and management. Singapore Med J. 2021;62(6):271–275.
4 Jamaludin A, Lootus M, Kadir T, Zisserman A, Urban J, Battié MC, et al. ISSLS PRIZE IN BIOENGINEERING SCIENCE 2017: Automation of reading of radiological features from magnetic resonance images (MRIs) of the lumbar spine without human intervention is comparable with an expert radiologist. Eur Spine J. 2017;26(5):1374–1383.
5 Lu JT, Pedemonte S, Bizzo B, Doyle S, Andriole KP, Michalski MH, et al. Deep Spine: Automated Lumbar Vertebral Segmentation, Disc-Level Designation, and Spinal Stenosis Grading using Deep Learning. Proceedings of the 3rd Machine Learning for Healthcare Conference. 2018;85:403–419.
6 Hallinan JTPD, Zhu L, Yang K, Makmur A, Algazwi DAR, Thian YL, et al. Deep Learning Model for Automated Detection and Classification of Central Canal, Lateral Recess, and Neural Foraminal Stenosis at Lumbar Spine MRI. Radiology. 2021;300(1):130–138.
7 Lurie JD, Tosteson AN, Tosteson TD, Carragee E, Carrino J, Kaiser J, et al. Reliability of readings of magnetic resonance imaging features of lumbar spinal stenosis. Spine (Phila Pa 1976). 2008;33:1605–10.
8 Fardon DF, Williams AL, Dohring EJ, Murtagh FR, Gabriel Rothman SL, Sze GK. Lumbar disc nomenclature: version 2.0: recommendations of the combined task forces of the North American Spine Society, the American Society of Spine Radiology and the American Society of Neuroradiology. Spine J. 2014;14(11):2525–45.
9 Andreisek G, Deyo RA, Jarvik JG, Porchet F, Winklhofer SF, Steurer J; et al. Consensus conference on core radiological parameters to describe lumbar stenosis - an initiative for structured reporting. Eur Radiol. 2014;24(12):3224–32.
10 Bartynski WS, Lin L. Lumbar root compression in the lateral recess: MR imaging, conventional myelography, and CT myelography comparison with surgical confirmation. AJNR Am J Neuroradiol. 2003;24(3):348–60.
11 Mamisch N, Brumann M, Hodler J, Held U, Brunner F, Steurer J, et al. Radiologic criteria for the diagnosis of spinal stenosis: results of a Delphi survey. Radiology. 2012;264(1):174–9.
12 Hayashi D. Deep Learning for Lumbar Spine MRI Reporting: A Welcome Tool for Radiologists. Radiology. 2021;300(1):139–140.
13 Lim DSW, Makmur A, Zhu L, Zhang W, Cheng AJL, Sia DSY, et al. Improved Productivity Using Deep Learning-assisted Reporting for Lumbar Spine MRI. Radiology. 2022;305(1):160–166.
14 Lee A, Wu J, Liu C, Makmur A, Ting YH, Muhamat Nor FE, et al. Deep learning model for automated diagnosis of degenerative cervical spondylosis and altered spinal cord signal on MRI. Spine J. 2025;25(2):255–264.
15 Hallinan JTPD, Zhu L, Zhang W, Kuah T, Lim DSW, Low XZ, et al. Deep Learning Model for Grading Metastatic Epidural Spinal Cord Compression on Staging CT. Cancers (Basel). 2022;14(13):3219.
16 Hallinan JTPD, Zhu L, Zhang W, Ge S, Muhamat Nor FE, Ong HY, et al. Deep learning assessment compared to radiologist reporting for metastatic spinal cord compression on CT. Front Oncol. 2023;13:1151073.
17 Hallinan JTPD, Zhu L, Tan HWN, Hui SJ, Lim X, Ong BWL, et al. A deep learning-based technique for the diagnosis of epidural spinal cord compression on thoracolumbar CT. Eur Spine J. 2023;32(11):3815–3824.
18 Hallinan JTPD, Zhu L, Zhang W, Lim DSW, Baskar S, Low XZ, et al. Deep Learning Model for Classifying Metastatic Epidural Spinal Cord Compression on MRI. Front Oncol. 2022;12:849447.
19 Lee A, Ong W, Makmur A, Ting YH, Tan WC, Lim SWD, et al. Applications of Artificial Intelligence and Machine Learning in Spine MRI. Bioengineering (Basel). 2024;11(9):894.
20 Bhayana R. Chatbots and Large Language Models in Radiology: A Practical Primer for Clinical and Research Applications. Radiology. 2024;310(1):e232756.
21 Hallinan JTPD, Leow NW, Ong W, Lee A, Low YX, Chan MDZ, et al. MRI spine request form enhancement and auto protocoling using a secure institutional large language model. Spine J. 2024:S1529-9430(24)01111-2.
22 Li J, Guan Z, Wang J, Cheung CY, Zheng Y, Lim LL, et al. Integrated image-based deep learning and language models for primary diabetes care. Nat Med. 2024;30(10):2886–2896.

Contact

James Hallinan, MBChB, FRCR
Senior Consultant Radiologist
Head of Musculoskeletal division
Assistant Professor, National University of Singapore
National University Hospital
Department of Diagnostic Imaging
5 Lower Kent Ridge Rd
NUH Main Building
Singapore 119074
james_hallinan@nuhs.edu.sg

Andrew Makmur, MBBS, FRCR
Group Chief Technology Officer and Consultant Radiologist
National University Health System (NUHS)
1E Kent Ridge Road
NUHS Tower Block
Singapore 119228
andrew_makmur@nuhs.edu.sg

Update on Imaging Hamstring Injuries with a Focus on the Biceps Femoris

Ara Kassarjian, M.D., FRCPC

Founder, Elite Sports Imaging SL, Pozuelo de Alarcón, Spain
Head of Radiology, Olympia Sports Medicine and Surgical Center, Madrid, Spain

Of all the muscle injuries in elite sports, hamstring injuries are the most common, with the long head of the biceps femoris most frequently affected. This article will focus on injuries of the biceps femoris and will discuss concepts that can be extrapolated to muscle injuries in general. It will also explore the follow-up of muscle injuries and their correlation with return-to-play/return-to-competition intervals.

General concepts

Some of the most common questions regarding muscle injuries in elite sports are:

- When should we image?
- How should we image?
- When can the athlete return to play/competition?

In elite sports, when a muscle injury occurs, imaging should be performed as soon as possible. This intermediate knowledge of the severity and extent of the injury is important for the athlete and the team in terms of short- and long-term planning for upcoming matches, tournaments, and other competitions.

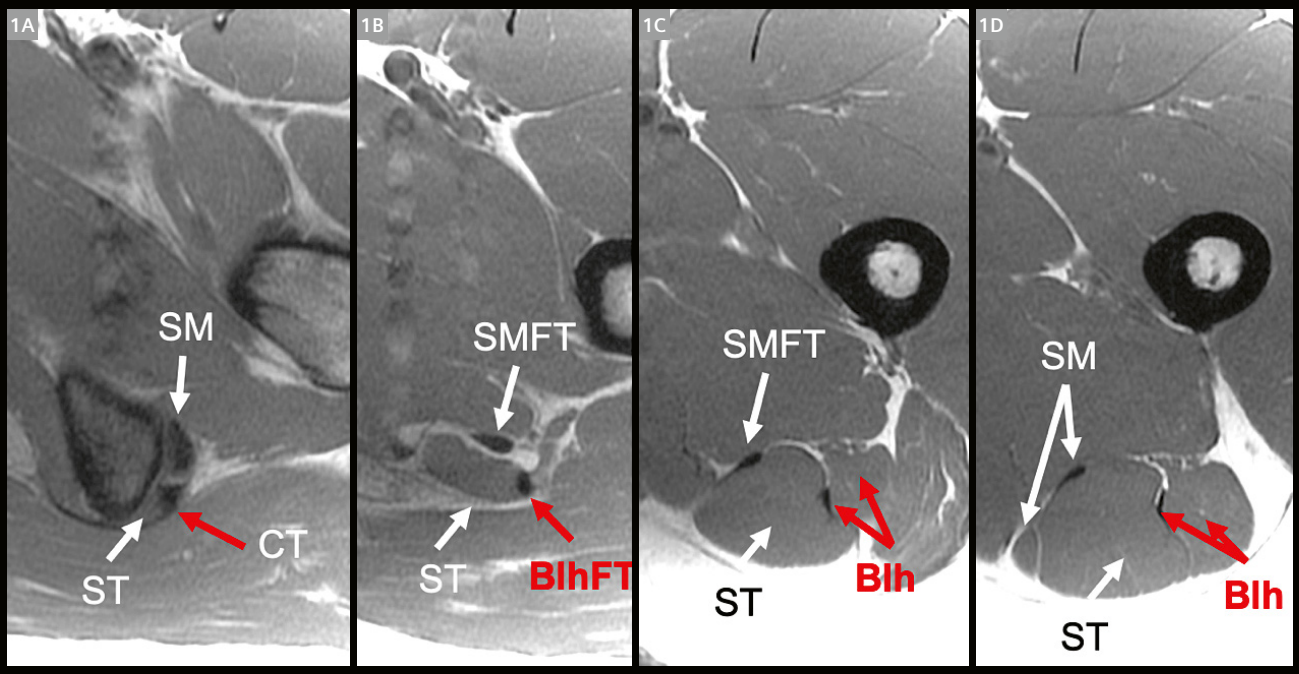

1 Axial proton-density (PD)-weighted images demonstrate the proximal hamstring anatomy. **(1A)** Origins of the semimembranosus (SM), semitendinosus (ST), and common tendon (CT) of the semitendinosus and biceps femoris long head. **(1B)** Semimembranosus free tendon (SMFT), semitendinosus muscle belly (ST), and biceps femoris long head free tendon (BlhFT). **(1C)** Semimembranosus free tendon (SMFT), semitendinosus muscle belly (ST), and biceps femoris long head muscle and tendon (Blh). **(1D)** Semimembranosus muscle and tendon (SM), semitendinosus muscle belly (ST), and biceps femoris long head muscle and tendon (Blh).

For acute hamstring injuries, magnetic resonance (MR) is the imaging modality of choice. It provides excellent soft tissue contrast at high resolution and allows detailed analysis of the tissues involved, particularly considering the complex anatomy of the hamstrings and the deep location of some of the structures, especially in athletic/muscular individuals. Although ultrasound can also be used, it has lower sensitivity during the first 24–48 hours [1]. It can also be limited in its evaluation of very proximal hamstring injuries, and in its ability to determine exactly which tissue components are involved in an acute injury.

When assessing acute muscle injuries, some general concepts need to be addressed. First of all, one must determine exactly which muscle or muscles are primarily involved in the injury. In addition, one must assess whether the injury involves the proximal, mid, or distal portion of the muscle. Finally, and most importantly, the detailed anatomical extent of the lesion must be assessed. Specifically, it is imperative to determine exactly which tissues are involved. This includes the tendon, the aponeurosis, the fascia (or epimysium), and the myofibrils (muscle fibers) [2–4]. Once the exact tissues involved have been determined, one must establish whether there is a loss of tension or a connective tissue gap.

When assessing MR exams, the axial images are the most adequate for determining exactly which tissue components are involved. Assessment of loss of tension and connective tissue gaps should be done on the three orthogonal planes. In particular, loss of tension is very difficult to assess on axial images and is often best assessed on coronal or sagittal images.

Hamstring injuries

As previously mentioned, MR is the imaging modality of choice for assessing hamstring injuries.

The most proximal injuries are avulsions at the level of the ischial tuberosity, where one or more tendons may be involved. The anatomy at this level is quite complex, with a common tendon of the biceps femoris and the semitendinosus, a muscular attachment of the semitendinosus, and a broad anterior and slightly more superior origin of the semimembranosus tendon (Fig. 1).

Subsequently, lesions can be divided across the three hamstring muscles: the biceps femoris, the semimembranosus, and the semitendinosus. This article focuses on the biceps femoris, as it is the most commonly injured of the hamstring muscles.

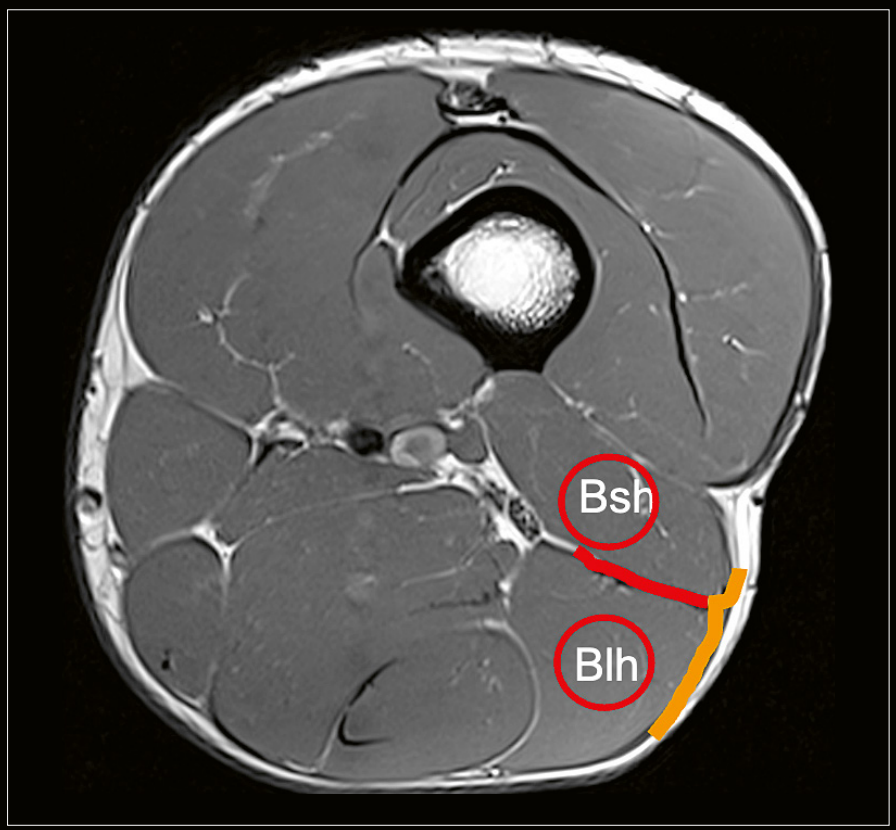

2 Axial PD-weighted images demonstrate the T-junction or zipper region of the biceps femoris. At this level, the muscle bellies of the long head (Blh) and short head (Bsh) of the biceps femoris are in close proximity and are intimately related to two connective tissue components that form a T: the superficial fascia/epimysium (yellow line) and the deep fascia/epimysium (red line).

Biceps femoris

The proximal anatomy of the biceps femoris includes a proximal free tendon of the long head of the biceps femoris, which attaches directly to the ischial tuberosity and has a variable length of between 4 and 7 cm, and an average of 5 cm. Although it may appear to have a myotendinous junction proximally, the muscle belly seen adjacent to the proximal free tendon of the long head of the biceps femoris is actually the muscle belly of the semitendinosus. The actual myotendinous junction of the long head of the biceps femoris can be seen further down (Fig. 1).

Another region of interest in the biceps femoris is the junction of the muscle bellies of the long head and short head, often referred to as the T-junction or the zipper. At this level, the two muscles are in close proximity and eventually form a common tendon distally (Fig. 2).

Two specific injuries to the biceps femoris are those of the proximal free tendon and of the T-junction/zipper. These lesions seem to have a longer return-to-play/competition (RTP/RTC) interval than other injuries [3, 5].

Biceps femoris free tendon injuries

It is of the utmost importance to localize the exact site of injury to the proximal free tendon of the biceps femoris. There are two common patterns of injury: The first is an actual avulsion of the tendon from its osseous attachment on the ischial tuberosity (Fig. 3). These lesions are typically quite evident on MR imaging, with a fluid-filled gap between the tendon and ischial tuberosity with surrounding hemorrhage. In addition, there is typically loss of tension in the tendon and caudal displacement of the tendon and the myotendinous junction of the long head of the biceps femoris. Free tendon avulsions are typically treated surgically in elite athletes. The other common site of injury of the free tendon is just proximal to and at its actual myotendinous junction and transition to the intra-muscular portion of the tendon (Fig. 4). At this level, high-resolution MR imaging is needed to assess whether it is a myotendinous injury with the tear centered at the actual myotendinous junction, or a tendinous injury with extension to the myotendinous junction. Axial images demonstrate the exact nature of the lesion and whether there is true tendinous involvement. These lesions typically have extensive adjacent muscle edema, often in the form of feathery edema. With high-grade incomplete tears, loss of tension

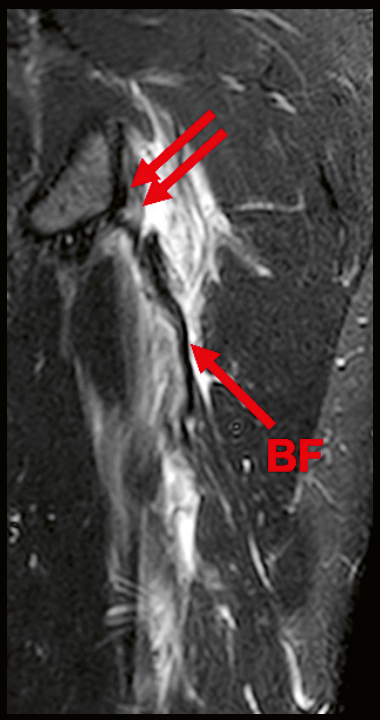

3 A 21-year-old professional soccer player with a surgically confirmed biceps femoris free tendon avulsion. Coronal T2-weighted fat-saturated imaging demonstrates the free tendon of the biceps femoris long head (BF) avulsed from the ischial tuberosity (double arrow) with loss of tension (single arrow) and extensive surrounding edema and fluid.

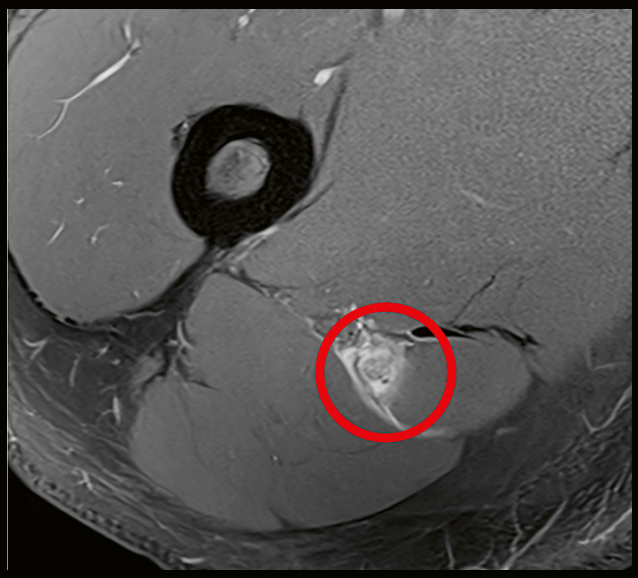

4 A 20-year-old professional soccer player with a surgically confirmed tear of the distal portion of the free tendon and proximal portion of the intramuscular tendon at the level of the proximal myotendinous junction of the biceps femoris. An axial intermediate-weighted fat-saturated image demonstrates complete loss of visualization of the normal hypointense tendon with surrounding edema and fluid.

is typically present, although it may not be as prominent as that seen with lesions in the more cranial portion of the free tendon. Treatment of the more distal free tendon and myotendinous injuries is controversial: Some advocate for early surgical intervention while others believe these lesions can be treated conservatively with subsequent adequate scarring and return of function.

Biceps femoris T-junction/zipper injuries

The other region of interest in biceps femoris injuries is the T-junction or distal zipper region. This is where the long and short heads of the biceps femoris join before forming a common tendon and inserting into the head of the fibula. This region is composed of both the superficial and deep components, with the deep component representing a connective tissue between the two muscle bellies. Injuries to this region are notorious for having a longer return-to-play interval, and appear to have a higher risk of reinjury (Fig. 5). This seems to be more the case with lesions that involve either both the superficial and deep components of the T-junction, or just the deep component. Isolated superficial lesions in this region seem to have a better prognosis and a lower incidence of reinjury.

Classification of muscle injuries

Many classification systems for muscle injuries have been proposed, including MRI and ultrasound classifications and, more recently, many MRI-specific classifications [5–7]. Although most classification systems have certain advantages, it is difficult to implement and generalize them, given the extensive variability in the architecture of the different muscle groups.

When considering the hamstring muscles, the most commonly used classification system is the British Athletics Muscle Injury Classification (BAMIC). Although this system appears to be useful in assessing injury and return-to-play intervals, its limitations include the fact that it was based on injuries in track-and-field athletes and does not differentiate between injuries of the different muscles within the hamstrings. In addition, there have been mixed experiences regarding the ability of the general classification systems to predict RTP and RTC intervals [8–12]. As such, it is probably more appropriate to described in detail which muscle, which component (e.g., proximal, mid, or distal), and which tissues (e.g., tendon or aponeurosis) are involved in the injury. In the future, it may be more appropriate to have specific classification systems for each of the most commonly injured muscles [13].

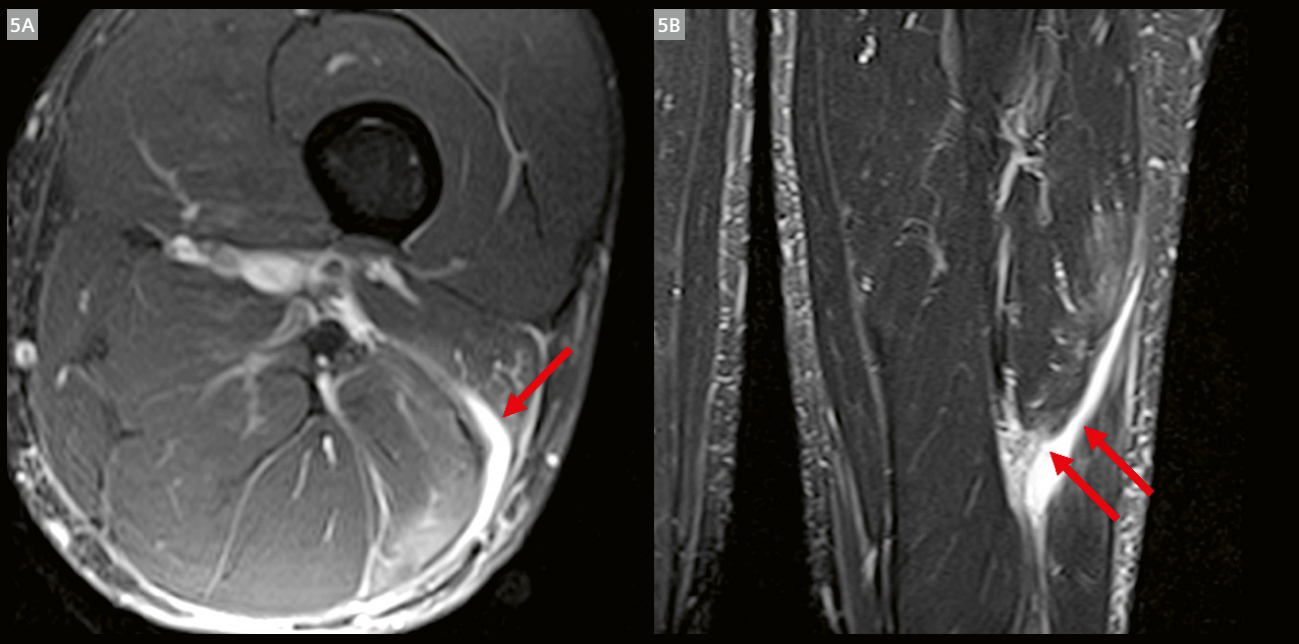

5 A 34-year-old amateur athlete with biceps femoris T-junction/zipper injury. Axial PD-weighted fat-saturated **(5A)** and coronal T2 fat-saturated **(5B)** sequences demonstrate an injury to the deep and superficial components of the T-junction (single arrow) with retraction of the biceps femoris long head muscle belly (double arrow).

Follow-up of muscle injuries

The protocol for following up on muscle injuries varies by site and according to regional preferences. In general, in elite athletes, follow-up of hamstring injuries is done with MRI, as it provides excellent soft tissue contrast and high resolution and enables assessment of the different phases of the healing process.

Following a muscle injury, there is a predictable progression of signal and morphological changes on MR imaging (Fig. 6) [14]. Initially, there is a destructive phase that lasts approximately one week and is characterized by extensive edema and high signal on T2-weighted images. Over the next 2–7 weeks, the tissues enter the various phases of repair with the appearance of scar formation, which is initially relatively hyperintense on T2-weighted images and progressively becomes more hypointense. In the late repair phase and subsequent remodeling phase, which can last from 10 weeks to a year, the initial hypertrophic scar undergoes remodeling with a progressive decrease in T2 signal. In the late remodeling phase and the final scarring phase, there is contraction of the scar, and a decline in T2 signal and T1 signal.

It should be noted that there can be significant overlap in the timing between the different phases depending on the individual biology of the injured athlete. However, the progression of the signal changes on MR imaging is relatively predictable.

Factors to consider before a return to play/ return to competition

During the recovery phase of muscle injuries, certain factors should be assessed as they may have a role in guiding training load. Preliminary studies suggest that the persistence or appearance of feathery edema around the soft tissue scar may be a sign of overload and that training intensity should be decreased. Conversely, cotton-like edema patterns (delayed-onset-muscle-soreness (DOMS) patterns) appear to represent adaptation to the training load and can be considered a normal finding during recovery.

In addition, certain MR findings may indicate an increased risk of reinjury, in the manner of red flags. They include a change in tendon morphology, increased signal in the tendon on T2-weighted images, a connective tissue gap, a gap in the forming scar, and the appearance of

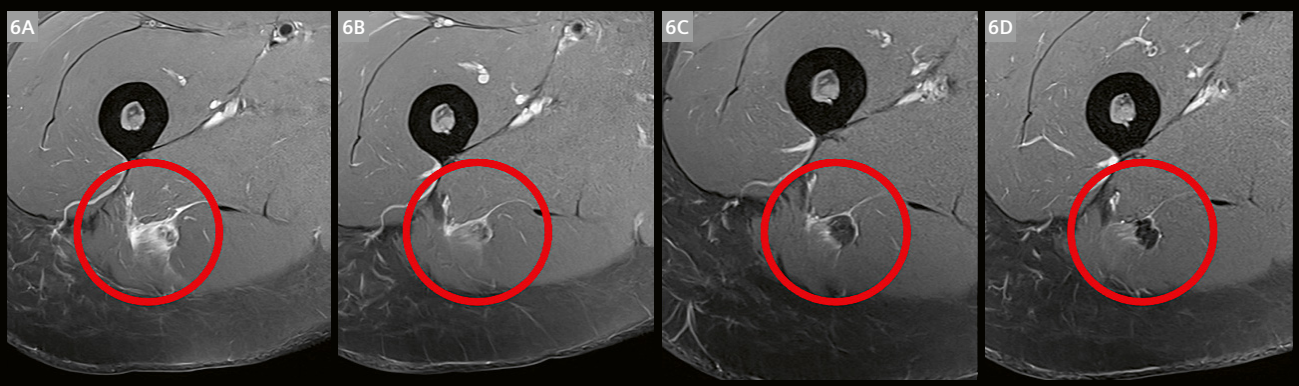

6 A 29-year-old professional female soccer player who sustained an acute injury to her right biceps femoris long head tendon at the level of the distal free tendon and proximal intramuscular tendon near the myotendinous junction. Axial intermediate-weighted fat-saturated images: At the time of initial injury **(6A)**, there is a tear of the distal portion of the free tendon and the proximal portion of the intramuscular tendon with intermuscular edema and intermuscular fluid. At two weeks **(6B)**, there is very early scar formation as the reparative phase is beginning with a scar that is essentially isointense to muscle. There is a decrease in intermuscular edema and a slight decrease in intermuscular fluid. At four weeks **(6C)**, there is further repair with the scar tissue becoming markedly hypointense to muscle. Adjacent intramuscular edema and intermuscular fluid continues to decrease. At six weeks **(6D)**, the scar is entering the late reparative phase with a further decrease in signal (very similar intensity to adjacent tendons) and the beginning of retraction and very early remodeling of the scar. Both intramuscular edema and intermuscular fluid are nearly completely resolved.

intermuscular edema and fluid. A preliminary study suggests that if two of these five findings are present, there is a very high risk of reinjury, with an odds ratio of 29 [15].

Conclusion

Imaging of hamstring injuries requires a detailed knowledge of the complex anatomy and patterns of injury. Injuries to the free tendon and the T-junction/zipper seem to have a longer RTP/RTC interval than other lesions.

Follow-up MR imaging of muscle injuries demonstrates a predictable progression of signal changes corresponding to the various phases of repair and remodeling.

Certain imaging features, such as a gap in the connective tissues or scar and the appearance of intermuscular fluid and edema, may be predictors of an increased risk of reinjury.

References

1 Connell DA, Schneider-Kolsky ME, Hoving JL, Malara F, Buchbinder R, Koulouris G, et al. Longitudinal study comparing sonographic and MRI assessments of acute and healing hamstring injuries. AJR Am J Roentgenol. 2004;183(4):975-84.

2 Isern-Kebschull J, Mechó S, Pruna R, Kassarjian A, Valle X, Yanguas X, et al. Sports-related lower limb muscle injuries: pattern recognition approach and MRI review. Insights Imaging. 2020;11:108.

3 Isern-Kebschull J, Mechó S, Kassarjian A, Bencardino JT. Injuries of the Hamstring Tendons: MR Imaging Diagnosis. Magn Reson Imaging Clin N Am. 2025;33(1):115-133.

4 Study Group of the Muscle and Tendon System from the Spanish Society of Sports Traumatology; Balius R, Blasi M, Pedret C, Alomar X, Peña-Amaro J, Vega JA, et al. A Histoarchitectural Approach to Skeletal Muscle Injury: Searching for a Common Nomenclature. Orthop J Sports Med. 2020;8(3):2325967120909090.

5 Valle X, Alentorn-Geli E, Tol JL, Hamilton B, Garrett WE Jr, Pruna R, et al. Muscle Injuries in Sports: A New Evidence-Informed and Expert Consensus-Based Classification with Clinical Application. Sports Med. 2017;47(7):1241-1253.

6 Pollock N, James SL, Lee JC, Chakraverty R. British athletics muscle injury classification: a new grading system. Br J Sports Med. 2014;48(18):1347-51.

7 Mueller-Wohlfahrt HW, Haensel L, Mithoefer K, Ekstrand J, English B, McNally S, et al. Terminology and classification of muscle injuries in sport: the Munich consensus statement. Br J Sports Med. 2013;47(6):342-50.

8 Day MA, Karlsson LH, Herzog MM, Weiss LJ, McGonegle SJ, Greditzer HG 4th, et al. Correlation of Player and Imaging Characteristics With Severity and Missed Time in National Football League Professional Athletes With Hamstring Strain Injury: A Retrospective Review. Am J Sports Med. 2024;52(11):2709-2717.

9 Fontanier V, Bruchard A, Tremblay M, Mohammed R, da Silva-Oolup S, Suri-Chilana M, et al. Classification of myo-connective tissue injuries for severity grading and return to play prediction: A scoping review. J Sci Med Sport. 2025;28(1):46-55.

10 Hollabaugh W, Hill T, Davidson C, Pennings J, Strasser N, Porras L, Cox C, Fitch R. Application of the British Athletics Muscle Injury Classification in Collegiate Football Athletes: A Retrospective, Observational Study. Sports Health. 2025:19417381251326531.

11 Kerin F, O'Flanagan S, Coyle J, Curley D, Farrell G, Persson UM, et al. Are all hamstring injuries equal? A retrospective analysis of time to return to full training following BAMIC type 'c' and T-junction injuries in professional men's rugby union. Scand J Med Sci Sports. 2024;34(2):e14586.

12 Zein MI, Reurink G, Suskens JJM, Monte JRC, Smithuis FF, Buckens S, et al. 3.0-Tesla MRI Observation at Return to Play After Hamstring Injuries. Clin J Sport Med. 2025;35(2):119-126.

13 Balius R, Pedret C, Kassarjian A. Muscle Madness and Making a Case for Muscle-Specific Classification Systems: A Leap from Tissue Injury to Organ Injury and System Dysfunction. Sports Med. 2021;51(2):193-197.

14 Isern-Kebschull J, Mechó S, Pedret C, Pruna R, Alomar X, Kassarjian A, et al. Muscle Healing in Sports Injuries: MRI Findings and Proposed Classification Based on a Single Institutional Experience and Clinical Observation. Radiographics. 2024;44(8):e230147.

15 Isern-Kebschull J, Pedret C, Mechó S, Pruna R, Alomar X, Yanguas X, et al. MRI findings prior to return to play as predictors of reinjury in professional athletes: a novel decision-making tool. Insights Imaging. 2022;13(1):203.

Contact

Ara Kassarjian, M.D., FRCPC
Founder, Elite Sports Imaging SL
Pozuelo de Alarcón
Spain

Head of Radiology, Olympia Sports Medicine and Surgical Center
Paseo de la Castellana 259E
28046 Madrid
Spain
kassarjian@me.com

Optimizing Brachial Plexus Magnetic Resonance Neurography at 3 Tesla

Yenpo Lin, M.D.[1]; Ek T. Tan, Ph.D.[1]; Xiaoying Cai, Ph.D.[2]; Peter Kollasch, M.Sc.[2]; Alto Stemmer, Dipl.-Phys.[3]; Marcel Dominik Nickel, Ph.D.[3]; Guido Buonincontri, Ph.D.[3]; Andreas Schäfer, Ph.D.[3]; Tom Hilbert, Ph.D.[4,5]; Darryl B. Sneag, M.D.[1]

[1]Department of Radiology and Imaging, Hospital for Special Surgery, New York, NY, USA
[2]Siemens Healthineers, Malvern, PA, USA
[3]Siemens Healthineers, Erlangen, Germany
[4]Advanced Clinical Imaging Technology, Siemens Healthineers International AG, Lausanne, Switzerland
[5]LTS5, École Polytechnique Fédérale de Lausanne (EPFL), Lausanne, Switzerland

Introduction

At the Hospital for Special Surgery (HSS), ongoing efforts are made to improve image quality in magnetic resonance neurography (MRN). MRN comprises a specialized set of techniques focused on imaging peripheral nerves, which can be challenging given their small size and non-linear course throughout the body. When utilized in parallel with electrodiagnostic testing, MRN not only facilitates accurate localization of nerve injuries but also offers a comprehensive assessment of both the injured nerve and the end-organ muscle. MRN of the brachial plexus (BP) presents unique challenges due to inherent field inhomogeneities related to the neck/shoulder curvature and proximity to the lungs [1]. In 2021, the first Siemens Healthineers system was installed at our institution – a MAGNETOM Vida 3T. In this article, we share our experience in optimizing imaging quality for BP imaging on the MAGNETOM Vida.

Three-coil setup:
20-channel HNU +
18-channel UltraFlex +
posterior Spine Coil

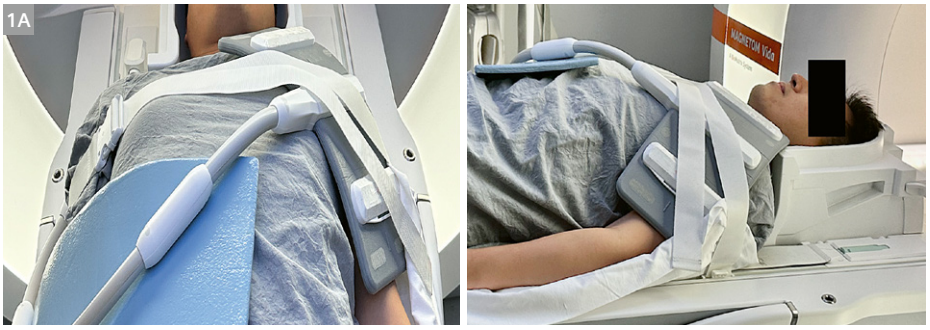

Two-coil setup:
18-channel UltraFlex
(anterior: small,
posterior: large)

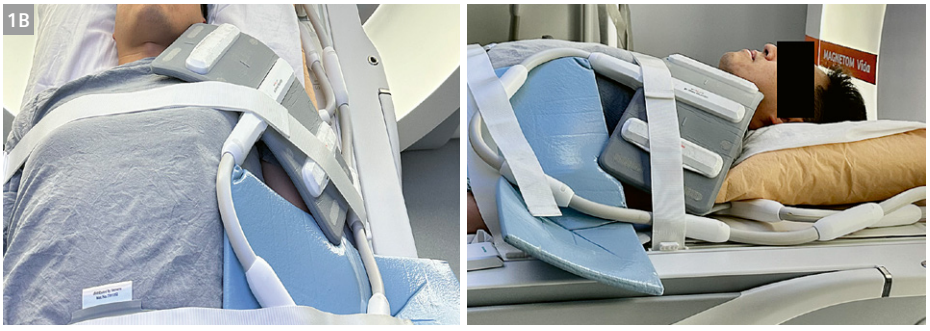

1 Comparison of coil types for unilateral, left brachial plexus MRN. **(1A)** Imaging with the neck at isocenter and the brachial plexus off isocenter using a combination of a 20-channel neurovascular array for the neck region, an 18-channel UltraFlex flexible coil array, and posterior spine elements. The BioMatrix Respiratory Sensor may be used for respiratory gating. **(1B)** An alternative setup with the left brachial plexus at isocenter, using two 18-channel UltraFlex arrays; the smaller coil is placed anteriorly while the larger coil is placed posteriorly (under the subject). An additional strap may be needed to deploy the respiratory pillow.

Sequence	2D IW-TSE	2D T2w-TSE	SPACE STIR	2D T2w-TSE
Deep Resolve Boost	Y	Y (Prototype)[1]	Y (Prototype)[1]	Y (Prototype)[1]
Orientation	Axial	Coronal	Double oblique-coronal	Oblique sagittal
Field of view, cm	28	32	30	16
TR/TE, ms	4000–6500/35	3000–9000/85	3000/161 (apparent TE = 60)	3000–6000/85
TI, ms	–	–	250	–
Matrix size (frequency × phase)	512 × 410	320 × 240	304 × 168	320 × 240
Pixel resolution (frequency × phase), mm^2	0.5 × 0.7	1.0 × 1.3	1.0 × 1.0	0.5 × 0.7
Slice thickness, mm (no spacing)	3.5	4.0	1.0	2.5
Slices	60	40–50	100–120	24–40
Bandwidth, Hz/Pixel	296	240	382	240
Turbo factor	14	14	130	14
Total acceleration factor (GRAPPA / CAIPIRINHA)	2	2	4	2
Gadolinium contrast	none	none	optional	none
Fat suppression	none	Dixon	STIR	Dixon/Fat saturation
Scan time, min:sec	2:00	3:45	4:40	4:00, variable with respiratory gating

Table 1: Unilateral brachial plexus protocol on MAGNETOM Vida 3T.
IW indicates intermediate-weighted; TSE: turbo spin echo; T2w: T2-weighted; TR: repetition time; TE: echo time; TI: inversion time; GRAPPA: generalized autocalibrating partial parallel acquisition; CAIPIRINHA: controlled aliasing in parallel imaging results in higher acceleration

[1] *Work in progress. The product is still under development and not commercially available. Its future availability cannot be ensured.*

Coil configuration

To maximize signal-to-noise ratio (SNR) for BP MRN, it is vital to use multichannel receiver arrays that cover the large anatomical regions of the neck, shoulder, and axilla, while also minimizing the distance between coil elements and the targeted anatomy [2]. At HSS, the BP is typically imaged unilaterally, rather than bilaterally, to optimize spatial resolution and coverage; if bilateral coverage is required, two unilateral scans are typically acquired. On the MAGNETOM Vida 3T, the preferred three-coil setup includes a combination of either a 20-channel neurovascular array for the neck region, an 18-channel UltraFlex flexible coil array (small or large, depending on coverage needed) over the chest wall/upper arm, and the posterior spine array (Fig. 1). Alternatively, two 18-channel UltraFlex arrays, the smaller version placed anteriorly and the larger placed posteriorly, can be placed (Fig. 1). The three-coil setup is easier to configure, in our experience, but the two-coil setup provides flexibility for positioning the targeted BP closer to magnet isocenter.

BP protocol – overview and rationale

Our current, unilateral BP protocol comprises acquisitions both longitudinal and orthogonal relative to the course of the nerve segments (Fig. 2). Following localizer scans, a two-dimensional (2D) axial intermediate-weighted (IW)-TSE is acquired to guide plotting of subsequent scans. Next, a large field of view 2D coronal T2-weighted Dixon TSE is acquired to assess the regional musculature. These two TSE sequences are used to plot the remaining nerve-sensitive scans: two, 2D oblique sagittal T2-weighted Dixon acquisitions for orthogonal, high in-plane

resolution and a single, coronal T2-weighted three-dimensional (3D) SPACE-STIR sequence for high through-plane resolution. For the SPACE-STIR, coverage is best optimized with a 'double oblique' prescription, which is first aligned parallel to the clavicle and includes cephalocaudal coverage from the C4 superior endplate to the axilla and anterior-posterior coverage from the chest wall to the posterior scapula. This is followed by a second alignment step, made off the 2D coronal T2-weighted Dixon TSE, from C4 to the axillary region.

Optimized 3D SPACE STIR

The SPACE sequence offers a significant advantage, compared to 2D imaging, by enabling higher through-plane spatial resolution (0.8–1.0 mm isotropic) and facilitating evaluation in any arbitrary plane without distortion, either using oblique or curved multiplanar reformations. We use a prototype SPACE-STIR sequence[1] with optimizations to improve B_0 and B_1+ robustness. These improvements include:

1. C-shaped frequency offset corrected inversion (C-FOCI) pulse for uniform fat suppression [3, 4],
2. variable flip angle train tailored with consideration of the B_1+ inhomogeneity and
3. deep-learning-based 3D reconstruction algorithm tailored for CAIPIRINHA sampling pattern for high-quality reconstruction.

In particular, 3D deep-learning reconstruction now facilitates acquisitions at 0.8 mm resolution, as compared to our default 1.0 mm-isotropic prescription (Fig. 3).

[1] *Work in progress. The product is still under development and not commercially available. Its future availability cannot be ensured.*

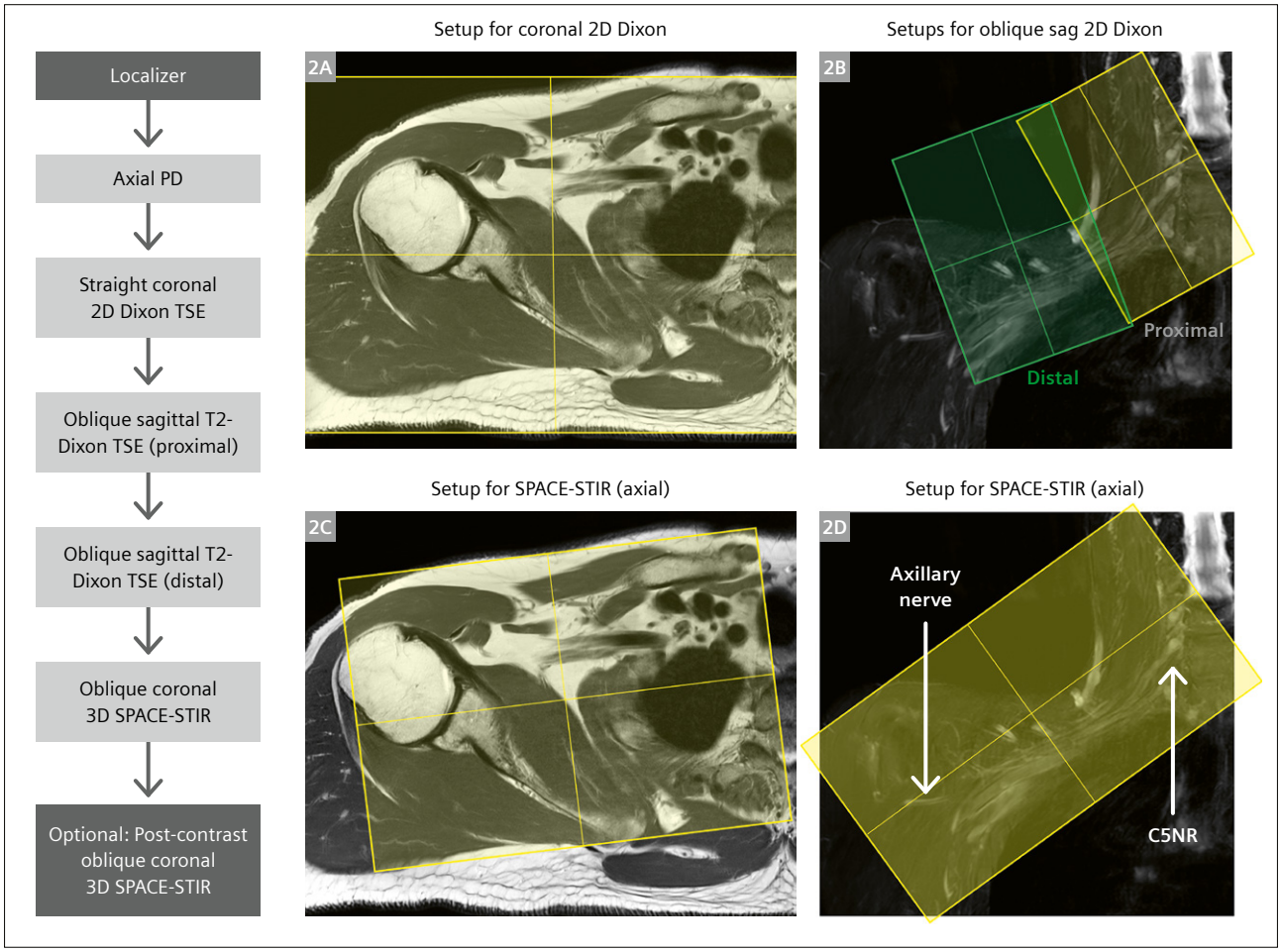

2 Suggested protocol for unilateral BP MRI, and illustration of prescription boxes. From the unilateral axial intermediate-weighted image **(2A)**, the straight coronal Dixon is plotted to cover 'skin-to-skin' (anterior to posterior) at the level of the subclavian vessels. Then two, 2D oblique sagittal T2-weighted Dixon scans are plotted off the coronal Dixon water image for proximal (yellow) and distal (green) coverages **(2B)**; two scans are needed to ensure the images are orthogonal to the BP. Finally, a double-oblique coronal 3D SPACE-STIR is plotted off the axial IW image, parallel to the clavicle **(2C)** and off the coronal Dixon, to include from the C5 nerve root to the axillary region (yellow box as shown in **2D**).

A SPACE-STIR sequence is sometimes acquired following intravenous gadolinium administration to improve vascular suppression, and to visualize small branch nerves of the plexus that may otherwise be obscured by venous contamination (Fig. 4) [5]. Gadolinium shortens the T1 of blood, thus bringing the blood T1 closer to that of fat, and reduces T2 transverse magnetization.

2D MRN

Orthogonal 2D MRN imaging typically provides higher in-plane spatial resolution, compared to 3D sequences, to better evaluate fascicular architecture [6]. However, achieving high in-plane spatial resolution (< 0.5 mm) within a clinically reasonable scan time (to mitigate respiratory motion artifact) while also maintaining adequate SNR poses a significant challenge. The Siemens Healthineers Deep Resolve Boost reconstruction algorithm helps mitigate these challenges by reducing noise amplification or blurring [7], when applying parallel imaging acceleration or partial Fourier acquisition.

Applying fat suppression techniques is also crucial in 2D MRN to enhance the contrast ratio between the peripheral nerves and surrounding fat. We typically employ the Dixon method in this context due to its ability to simultaneously provide homogenous fat suppression (despite field inhomogeneities) and high SNR efficiency. This is particularly important in the neck-shoulder region, which has high B_0-variation. For the 2D Dixon sequence on the MAGNETOM Vida system, one can choose between 'strong' and 'weak' fat suppression modes to modulate the degree to which the fat signal contributes to the MR images. Our preference is the 'strong' option to optimize nerve/muscle and nerve/fat contrast.

Respiratory triggering

Orthogonal imaging planes, particularly those through the infraclavicular segments of the BP, are prone to aliasing from respiratory motion due to the proximity of such segments to the lung apex. Respiratory motion artifacts are sometimes severe and may render the exam uninterpretable. Use of prospective respiratory

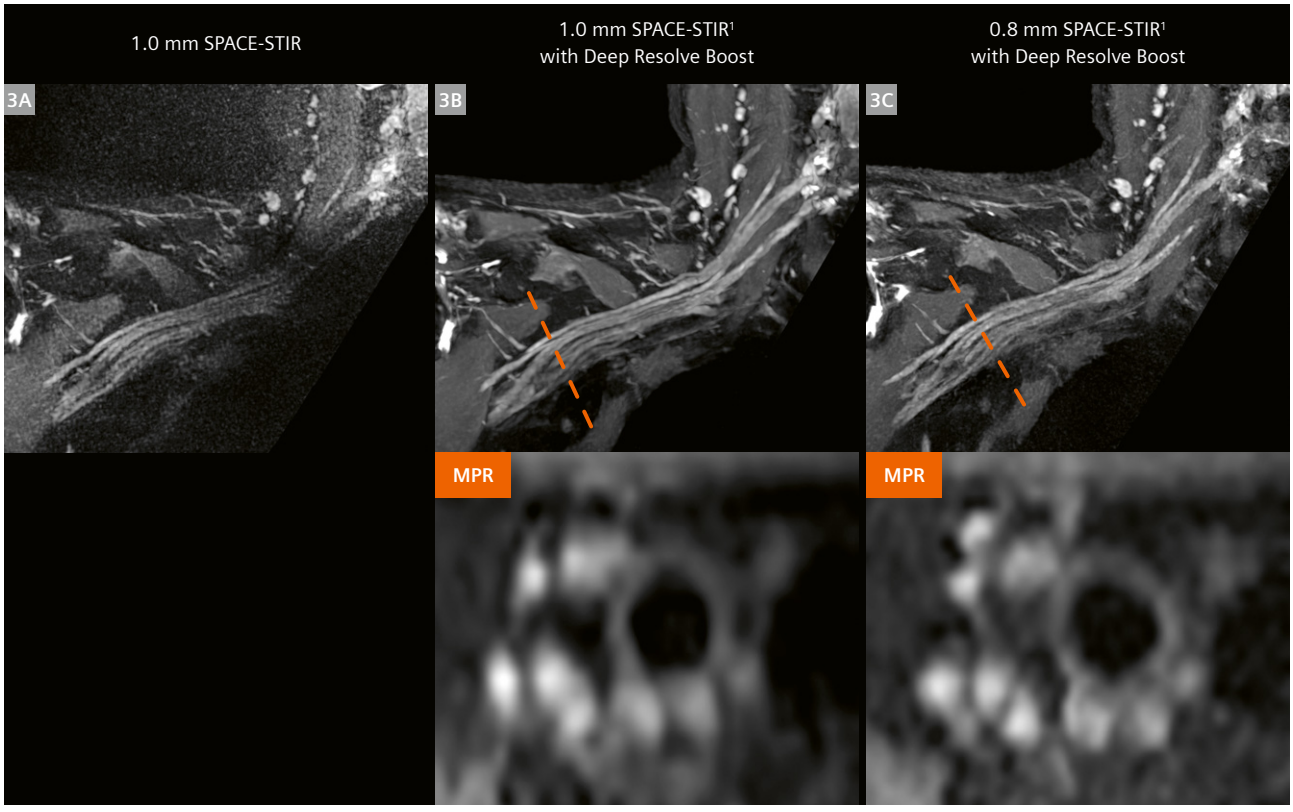

3 Comparison of SPACE-STIR acquired with standard reconstruction and with Deep Resolve (DR) Boost reconstruction. The top row images are all coronal SPACE-STIR images with 10 mm maximal intensity projection (MIP). **(3A)** Standard reconstruction of a 1.0 mm isotropic acquisition exhibits poor conspicuity of the brachial plexus. **(3B)** With DR Boost, improved conspicuity of the nerves is observed. **(3C)** DR Boost with 0.8 mm acquisition is feasible, providing sharper nerve definition, especially in the oblique-axial multiplanar reformation orthogonal to the brachial plexus at the level of the dashed lines (bottom row).

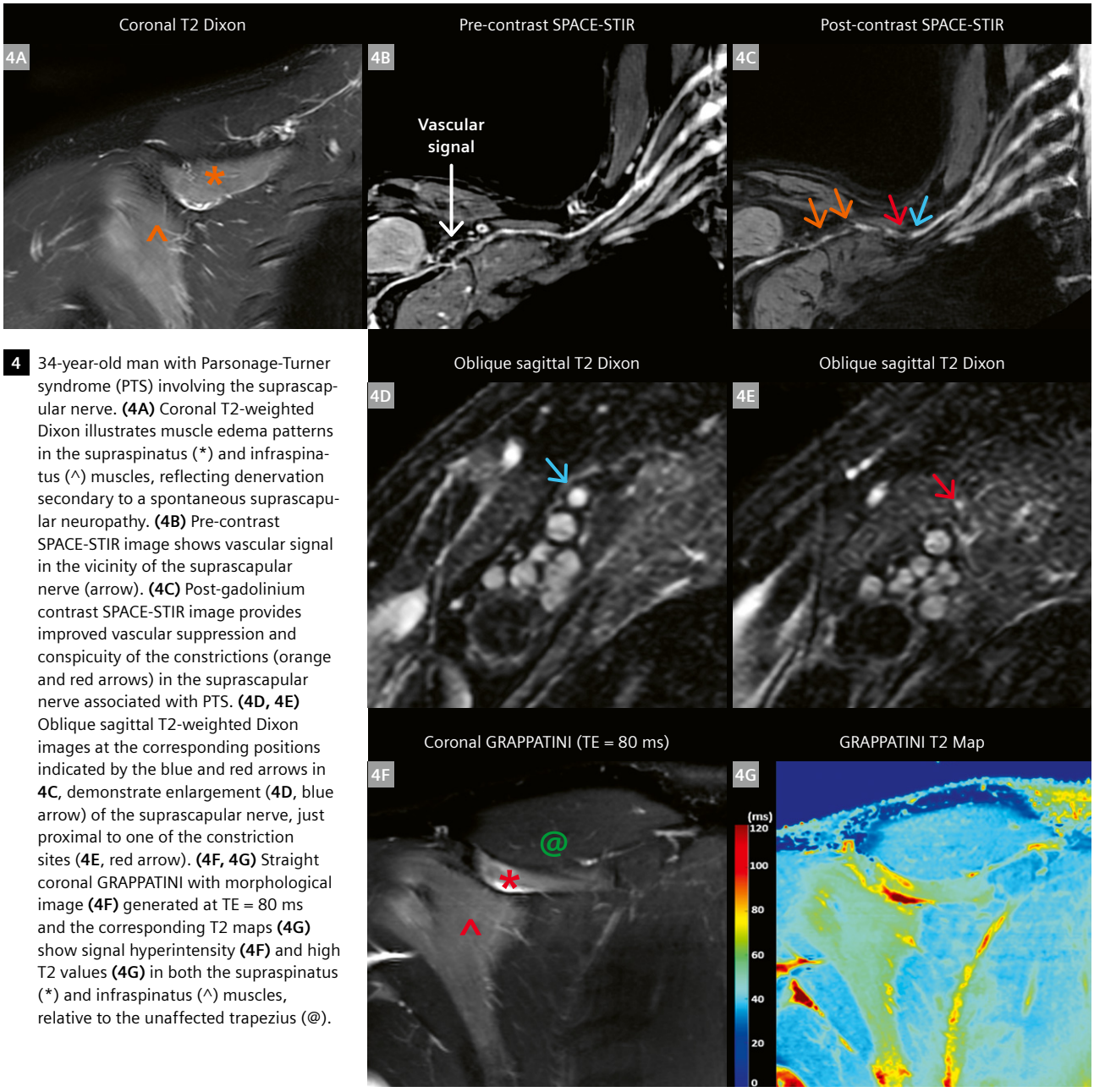

4 34-year-old man with Parsonage-Turner syndrome (PTS) involving the suprascapular nerve. **(4A)** Coronal T2-weighted Dixon illustrates muscle edema patterns in the supraspinatus (*) and infraspinatus (^) muscles, reflecting denervation secondary to a spontaneous suprascapular neuropathy. **(4B)** Pre-contrast SPACE-STIR image shows vascular signal in the vicinity of the suprascapular nerve (arrow). **(4C)** Post-gadolinium contrast SPACE-STIR image provides improved vascular suppression and conspicuity of the constrictions (orange and red arrows) in the suprascapular nerve associated with PTS. **(4D, 4E)** Oblique sagittal T2-weighted Dixon images at the corresponding positions indicated by the blue and red arrows in **4C**, demonstrate enlargement (**4D**, blue arrow) of the suprascapular nerve, just proximal to one of the constriction sites (**4E**, red arrow). **(4F, 4G)** Straight coronal GRAPPATINI with morphological image **(4F)** generated at TE = 80 ms and the corresponding T2 maps **(4G)** show signal hyperintensity **(4F)** and high T2 values **(4G)** in both the supraspinatus (*) and infraspinatus (^) muscles, relative to the unaffected trapezius (@).

triggering via bellows to enable acquisitions during maximal end-expiration has been shown to improve interobserver agreement and nerve conspicuity [8]. On the MAGNETOM Vida, prospective respiratory gating uses the BioMatrix Respiratory Sensor embedded into the posterior spine array. These sensors automatically detect and record respiratory and head movements once the patient is positioned on the table. This feature enhances workflow efficiency by enabling technologists to perform respiratory-triggered scans without incurring additional setup time (Fig. 5). Alternatively, the respiratory signal may also be obtained using the respiratory cushion complete with belt setup where an additional posterior phased-array coil is placed between the patient and the table in the two-coil setup.

Future directions

Quantitative MRI techniques, including T2 mapping, perfusion, and diffusion-weighted or diffusion tensor imaging (DWI/DTI), carry the potential to supplement qualitative BP assessment. A study of patients with chronic inflammatory demyelinating polyneuropathy found that not only were nerve root sizes enlarged but also demonstrated elevated

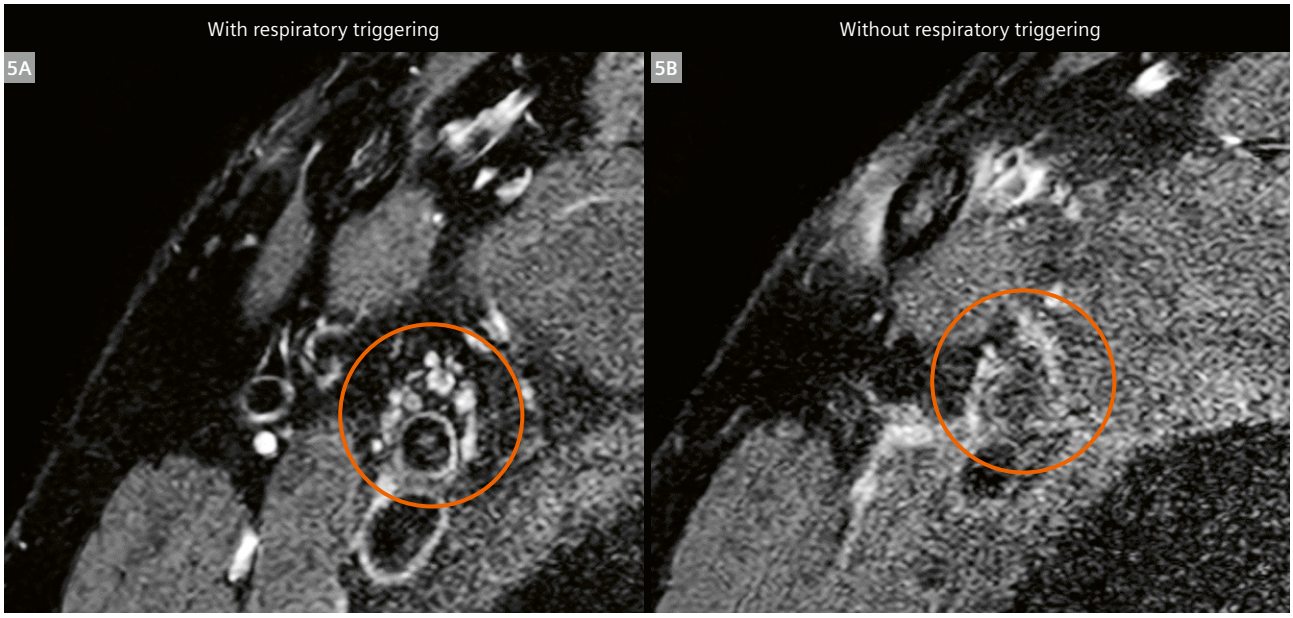

5 Oblique sagittal T2 Dixon imaging through the infraclavicular plexus (distal acquisition), demonstrates improved conspicuity of the cords with prospective respiratory gating (**5A**, using the imbedded BioMatrix Sensors) compared to the non-gated respiratory acquisition **(5B)**. Note that the gated scan requires approximately two minutes longer to acquire.

T2 relaxation times [9]. A quantitative Siemens Healthineers MRI prototype sequence, generalized autocalibrating partially parallel acquisition with the model-based accelerated relaxometry by iterative nonlinear inversion (GRAPPATINI)[1], can provide accurate T2 estimations and synthetic morphologic images [10, 11]. This technique may enable simultaneous qualitative and quantitative evaluation of both nerves and muscles in MR neurography, thereby shortening overall scan time and reducing registration errors between two separate acquisitions (Fig. 4F–G).

References

1 Davidson EJ, Tan ET, Pedrick EG, Sneag DB. Brachial Plexus Magnetic Resonance Neurography: Technical Challenges and Solutions. Invest Radiol. 2023;58(1):14-27.
2 Sneag DB, Queler S. Technological Advancements in Magnetic Resonance Neurography. Curr Neurol Neurosci Rep. 2019;19(10):75.
3 Ordidge RJ, Wylezinska M, Hugg JW, Butterworth E, Franconi F. Frequency offset corrected inversion (FOCI) pulses for use in localized spectroscopy. Magn Reson Med. 1996;36(4):562-566.
4 Wang X, Greer JS, Dimitrov IE, Pezeshk P, Chhabra A, Madhuranthakam AJ. Frequency Offset Corrected Inversion Pulse for B0 and B1 Insensitive Fat Suppression at 3T: Application to MR Neurography of Brachial Plexus. J Magn Reson Imaging. 2018;48(4):1104-1111.
5 Sneag DB, Daniels SP, Geannette C, Queler SC, Lin BQ, de Silva C, et al. Post-Contrast 3D Inversion Recovery Magnetic Resonance Neurography for Evaluation of Branch Nerves of the Brachial Plexus. Eur J Radiol. 2020;132:109304.
6 Sneag DB, Rancy SK, Wolfe SW, Lee SC, Kalia V, Lee SK, et al. Brachial plexitis or neuritis? MRI features of lesion distribution in Parsonage-Turner syndrome. Muscle Nerve. 2018;58(3):359-366.
7 Zochowski KC, Tan ET, Argentieri EC, Lin B, Burge AJ, Queler SC, et al. Improvement of peripheral nerve visualization using a deep learning-based MR reconstruction algorithm. Magn Reson Imaging. 2022;85:186-192.
8 Sneag DB, Mendapara P, Zhu JC, Lee SC, Lin B, Curlin J, et al. Prospective respiratory triggering improves high-resolution brachial plexus MRI quality. J Magn Reson Imaging. 2019;49(6):1723-1729.
9 Hiwatashi A, Togao O, Yamashita K, Kikuchi K, Momosaka D, Nakatake H, et al. Simultaneous MR neurography and apparent T2 mapping in brachial plexus: Evaluation of patients with chronic inflammatory demyelinating polyradiculoneuropathy. Magn Reson Imaging. 2019;55:112-117.
10 Roux M, Hilbert T, Hussami M, Becce F, Kober T, Omoumi P. MRI T2 Mapping of the Knee Providing Synthetic Morphologic Images: Comparison to Conventional Turbo Spin-Echo MRI. Radiology. 2019;293(3):620-630.
11 Wang F, Zhang H, Wu C, Wang Q, Hou B, Sun Y, et al. Quantitative T2 mapping accelerated by GRAPPATINI for evaluation of muscles in patients with myositis. Br J Radiol. 2019;92(1102):20190109.

Contact

Darryl B. Sneag, M.D.
Director of MRI Research & MR Neurography
Hospital for Special Surgery
535 East 70th Street
New York, NY 10021
USA
Tel.: +1 646 714 6043
sneagd@HSS.EDU

[1] *Work in progress. The product is still under development and not commercially available. Its future availability cannot be ensured.*

Exploring the T2-Mapping GRAPPATINI Technique for Qualitative and Quantitative Assessment of Orthopedic and Neuromuscular Conditions

Ek T. Tan, Ph.D.; Amy Z. Lu, BS; Darryl B. Sneag, M.D.

Department of Radiology and Imaging, Hospital for Special Surgery, New York, NY, USA
Weill Cornell Medical College, New York, NY, USA

Introduction

Quantitative T2 mapping has emerged as a promising tool for several diagnostic MRI applications, including the evaluation of orthopedic and neuromuscular pathology. Traditionally, T2 mapping has been constrained by long acquisition times and low spatial resolution, thereby requiring a separate acquisition added to routine scans. However, T2 mapping has seen renewed attention with the introduction of techniques for accelerating T2 mapping, such as GRAPPATINI[1] [1], which combines two acceleration techniques:

1) acceleration in *k*-space sampling using generalized autocalibrating partially parallel acquisition (GRAPPA) [2] and
2) acceleration in echo sampling using model-based accelerated relaxometry by iterative non-linear inversion (MARTINI) [3] (Fig. 1).

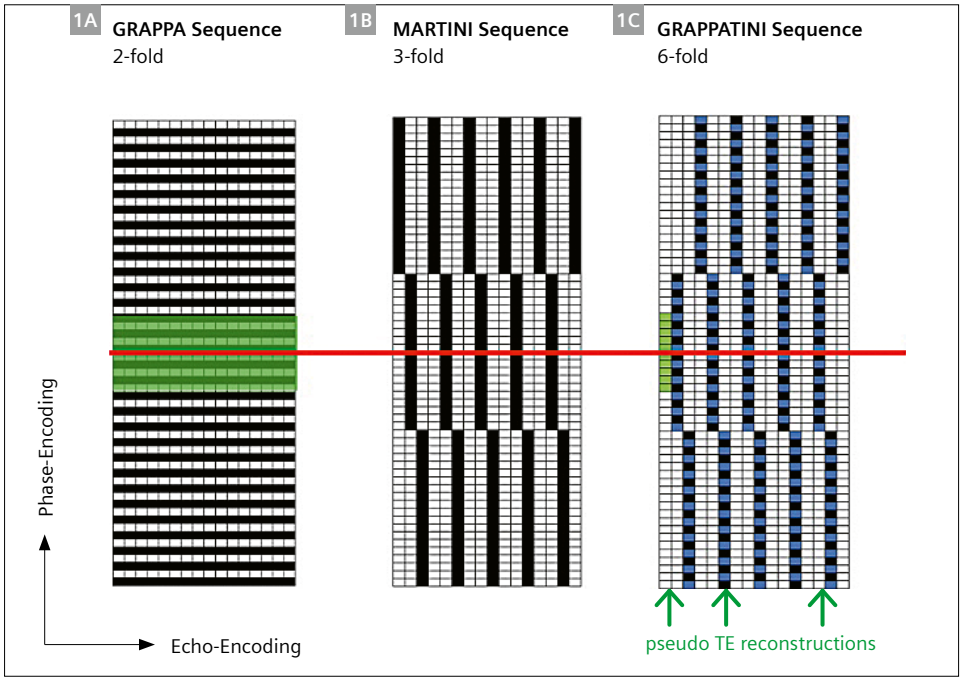

1 **(1A)** Standard, 2-fold GRAPPA compared to **(1B)** MARTINI and **(1C)** GRAPPATINI sampling patterns. The black squares indicate sampled *k*-space points in a 60 × 16 phase/echo-encoding matrix. The red line indicates the *k*-space center with zero phase encoding. The green samples in the GRAPPA and GRAPPATINI patterns indicate *k*-space points used for calibration. The blue squares indicate unsampled *k*-space points that are reconstructed using the GRAPPA method. Pseudo-TE reconstructions can be performed at arbitrary echo times (green arrows).

[1] *Work in progress. The application is currently under development and is not for sale in the U.S. and in other countries. Its future availability cannot be ensured.*

This hybrid acceleration method enables rapid T2 quantification while simultaneously producing synthetic T2-weighted images that can be used for diagnostic interpretation (Fig. 2).

Here, we share our initial clinical experiences of applying GRAPPATINI to neuromuscular and orthopedic imaging. This report includes key results from a recently published study applying GRAPPATINI to the lower extremity for assessment of foot drop [4], as well as additional examples for other conditions and anatomical regions. All subjects participating in studies involving the GRAPPATINI research sequence provided written informed consent under an institutional review board (IRB) approved protocol.

GRAPPATINI in neuromuscular imaging: peripheral nerve and muscle

Foot drop is a neurological condition frequently attributed to entrapment of the common peroneal nerve (CPN) as it courses through a fibro-osseous tunnel of the fibular neck at the knee [5]. In a recent study published in the *Journal of Magnetic Resonance Imaging* (JMRI) [4], we prospectively recruited 27 patients with suspected foot drop undergoing 3T magnetic resonance neurography (MRN) of the distal thigh and knee region and added a fat-suppressed GRAPPATINI sequence to routine, clinical sequences [5]. Specifically, the conventional T2-weighted (T2w) Dixon-fat-suppressed turbo spin echo (TSE) sequence was used to evaluate the distal sciatic nerve and its common peroneal and tibial nerve branches, and to detect active muscle denervation, primarily in the anterior tibialis that controls

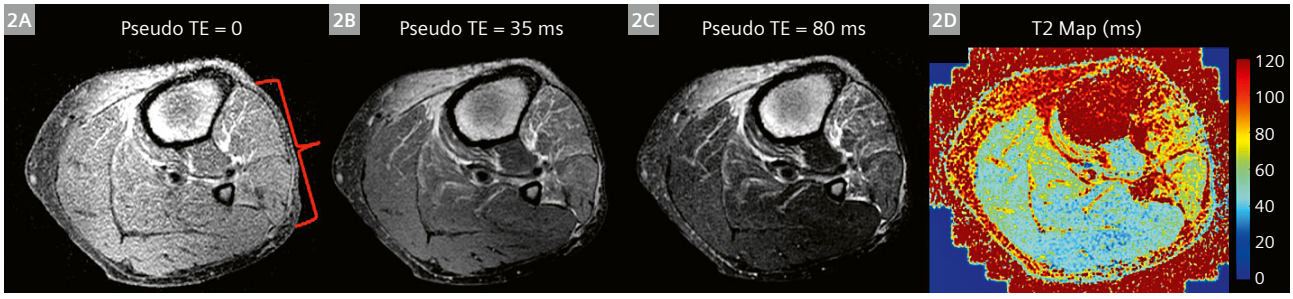

2 62-year-old male with prior total knee arthroplasty (TKA) and foot drop. Axial GRAPPATINI 3T imaging performed with chemical saturation fat suppression on the left calf region just distal to the TKA, demonstrates increased muscle signal in the anterior compartment with increased pseudo-echo times (TE) **(2A, 2B** and **2C)**, and elevated quantitative T2 values **(2D)**, corresponding to muscle edema related to active muscle denervation.

Parameter	T2w Dixon TSE	GRAPPATINI
Sequence type	T2w-TSE with Dixon fat suppression	Model-based T2 mapping (GRAPPATINI)
Scan orientation	Axial	Axial
TR (ms)	5000–11070	3000–9980
TE (ms)	80	10, 20, ..., 100
GRAPPA factor	2	2
MARTINI factor	–	3
Scan time (min)	3:00–7:00	3:09–6:49
FOV (cm)	14–15	14–15
Matrix	320 × 256	322 × 373
Slice thickness (mm)	3–3.5	3–3.5
Slices	48–92	22–50
Readout bandwidth (Hz/pixel)	240–425	243–354

Table 1: Pulse sequence parameters for T2w Dixon TSE and GRAPPATINI imaging techniques in neuromuscular imaging for foot drop assessment at 3T.

foot dorsiflexion. The GRAPPATINI sequence was added in the sections imaged with T2w-Dixon-TSE, and synthetic images were generated at TE = 80 ms for qualitative comparison (Table 1). The GRAPPATINI sequence provided high-resolution, synthetic T2-weighted images and quantitative T2 maps within a scan time of 3–6 minutes (variable depending on longitudinal coverage and slice thickness). Qualitative image assessments, including fascicular nerve architecture, muscle visualization, and diagnostic confidence, were found by three readers to be comparable to conventional T2w-Dixon imaging.

Importantly, GRAPPATINI also enabled quantitative T2 measurements of the common peroneal and tibial nerves (Fig. 2), as well as affected and unaffected lower extremity muscles (Fig. 3). Elevated T2 values in injured nerves and denervated muscle provide a quantitative depiction of pathology [6, 7]; for example, elevated T2 values in muscle denervation have been found to correlate better with electromyography results as compared to qualitative T2-weighted imaging [8]. In our study, a statistically significant T2 elevation was observed in denervated compared to non-denervated muscles (e.g., tibialis anterior:

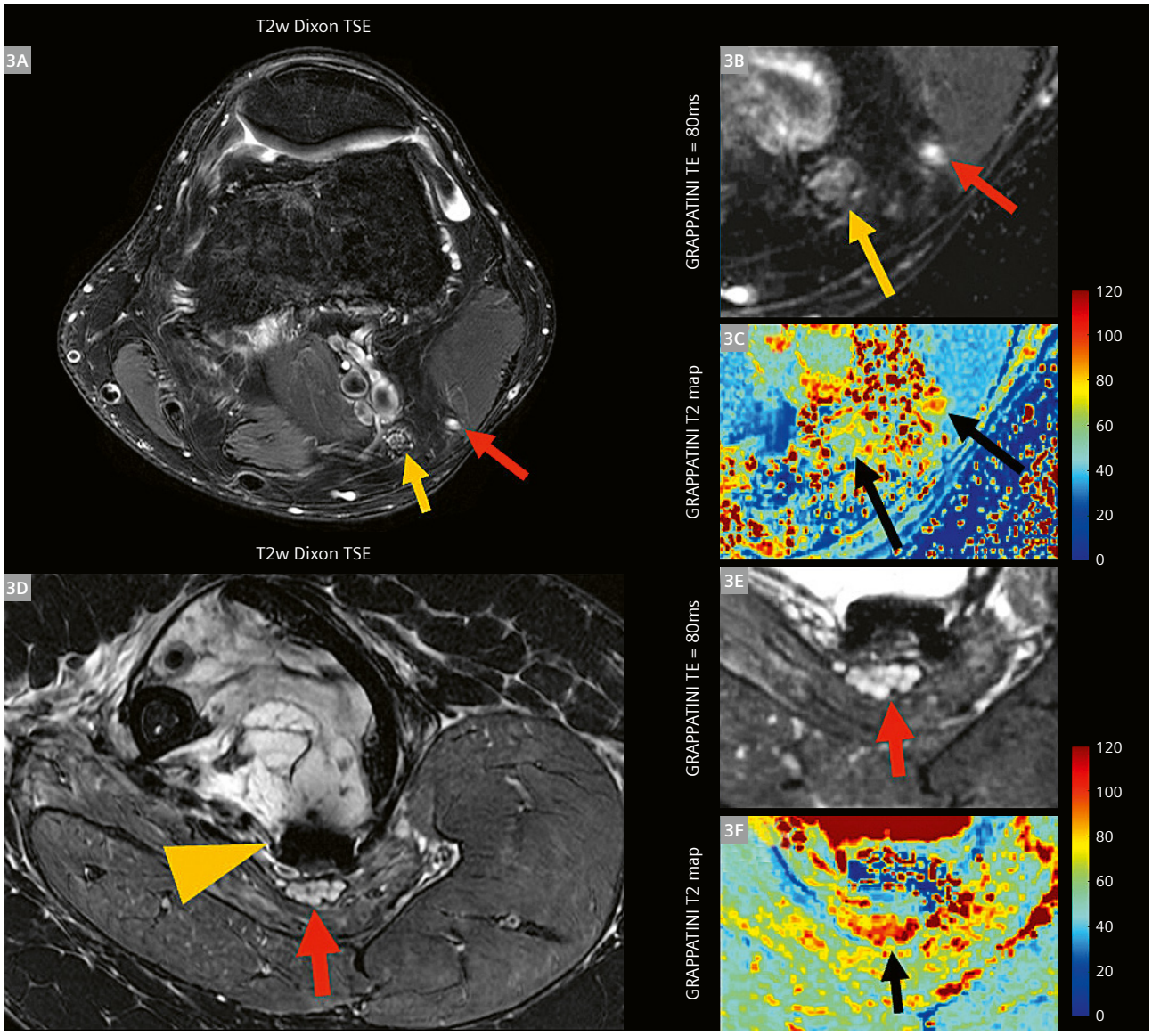

3 Two examples in the lower extremity at 3T. A 56-year-old male with left foot drop (3A–3C). **(3A)** Conventional T2-weighted Dixon TSE images demonstrate hyperintensity of the common peroneal nerve (red arrow) relative to the normal tibial nerve (yellow arrow). Fat-suppressed GRAPPATINI synthetic T2-weighted (T2w) magnified image **(3B)** at TE = 80 ms demonstrates signal hyperintensity corresponding to elevated T2 values **(3C)**. A 19-year-old male with synovial sarcoma post partial tibial resection, screw fixation, and radiotherapy (3D–3F). Conventional imaging **(3D)** and GRAPPATINI TE = 80 ms **(3E)** demonstrate a hyperintense, enlarged tibial nerve (red arrow) posterior to the fixation hardware (yellow arrowhead). T2 mapping shows corresponding high T2 of the tibial nerve (**3F**, arrow).

72.6 ms vs. 46.6 ms, p = 0.002), supporting the utility of GRAPPATINI T2 maps to identify neuromuscular pathology and possibly quantify denervation severity.

GRAPPATINI may also be readily applied to other anatomical regions, e.g., the brachial plexus, for evaluation of peripheral neuropathy such as Parsonage-Turner syndrome (PTS). This condition, also known as neuralgic amyotrophy, commonly involves hourglass-like constrictions of different nerves in the upper extremities and results in severe muscle denervation in the motor distribution of these nerves [6] (Figs. 4 and 5).

GRAPPATINI in orthopedics: intervertebral disc and cartilage

We further explored GRAPPATINI's potential in the spine. T2 mapping has been previously employed to quantify microstructural changes of the degenerated lumbar intervertebral disc, with decreased T2 corresponding with qualitative severity using the Pfirrmann grading scale [9]. A relatively quick 3-minute GRAPPATINI sequence can be similarly acquired to quantify T2 disc values, with pseudo-images generated at longer echo times considered

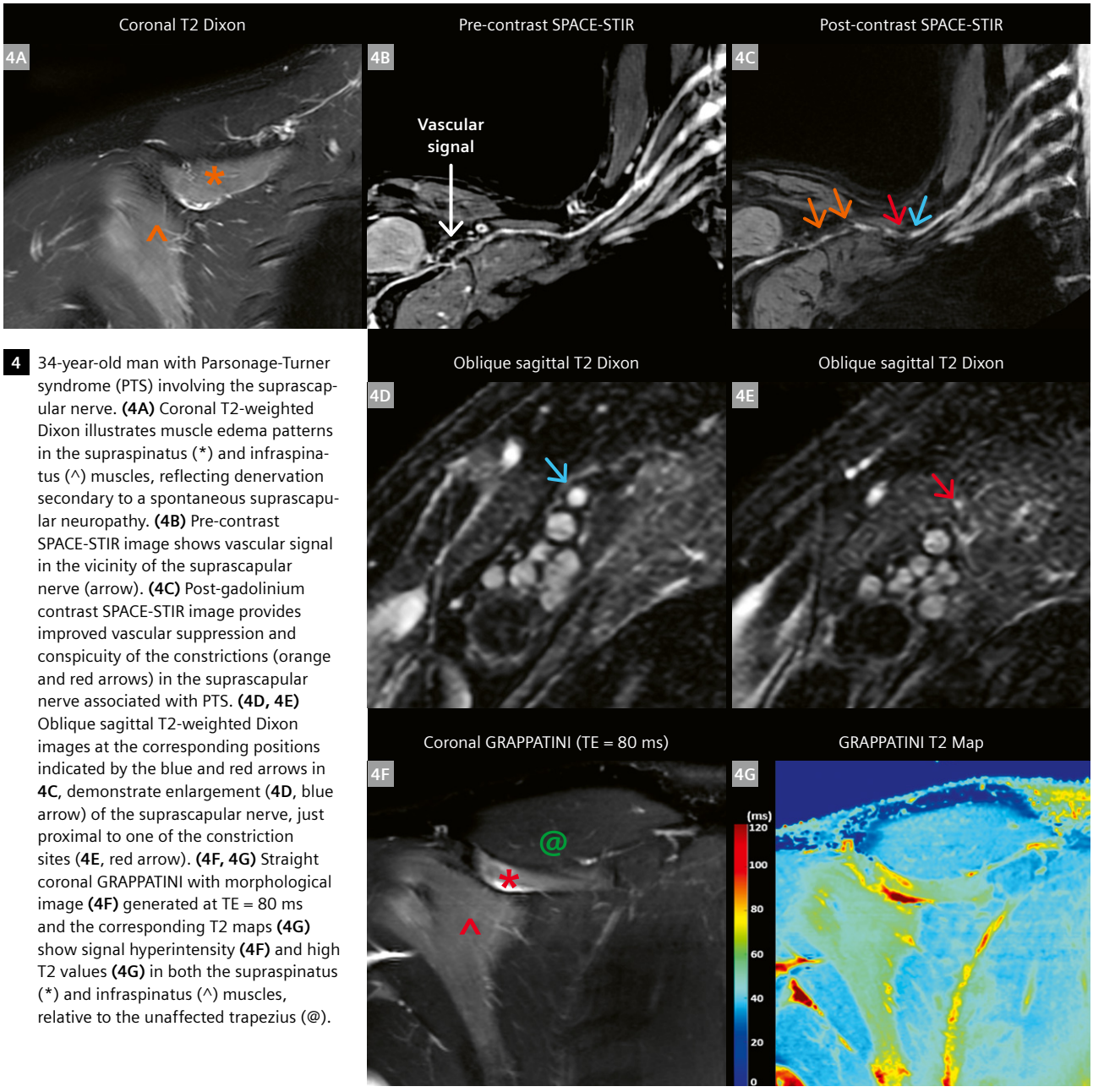

4 34-year-old man with Parsonage-Turner syndrome (PTS) involving the suprascapular nerve. **(4A)** Coronal T2-weighted Dixon illustrates muscle edema patterns in the supraspinatus (*) and infraspinatus (^) muscles, reflecting denervation secondary to a spontaneous suprascapular neuropathy. **(4B)** Pre-contrast SPACE-STIR image shows vascular signal in the vicinity of the suprascapular nerve (arrow). **(4C)** Post-gadolinium contrast SPACE-STIR image provides improved vascular suppression and conspicuity of the constrictions (orange and red arrows) in the suprascapular nerve associated with PTS. **(4D, 4E)** Oblique sagittal T2-weighted Dixon images at the corresponding positions indicated by the blue and red arrows in **4C**, demonstrate enlargement (**4D**, blue arrow) of the suprascapular nerve, just proximal to one of the constriction sites (**4E**, red arrow). **(4F, 4G)** Straight coronal GRAPPATINI with morphological image **(4F)** generated at TE = 80 ms and the corresponding T2 maps **(4G)** show signal hyperintensity **(4F)** and high T2 values **(4G)** in both the supraspinatus (*) and infraspinatus (^) muscles, relative to the unaffected trapezius (@).

in lieu of a separate, standard sagittal T2-TSE acquisition (Fig. 6). The addition of T2 mapping may potentially be beneficial for assessing early changes in disc microstructure to help guide non-surgical management of low back pain and training regimens in high-performance athletes.

Another potential application of GRAPPATINI is cartilage evaluation. Quantitative T2 mapping is a valuable tool for assessing cartilage and meniscus integrity and matrix composition, offering noninvasive insight into early degenerative changes before morphological defects manifest [10, 11]. In a series of 9 patients (4 females, 5 males, mean [range] age = 45 [27–72]) undergoing clinical knee MRI for cartilage and meniscal evaluation, a non-fat-suppressed GRAPPATINI sequence was added with a focus to obtain high-resolution, multiplanar T2 mapping at accelerated scan times and compare T2 values to those obtained using a conventional T2-mapping sequence (MapIt) (Table 2, Fig. 7). The GRAPPATINI technique not only provided high-resolution, synthetic proton-density-weighted and T2-weighted images, but also excellent agreement with standard T2 mapping (Table 3). While we did not explore the potential for qualitative evaluation in this study, the GRAPPATINI sequence can provide a synthetic image at a similar echo time as our conventional proton-density-weighted TSE sequence.

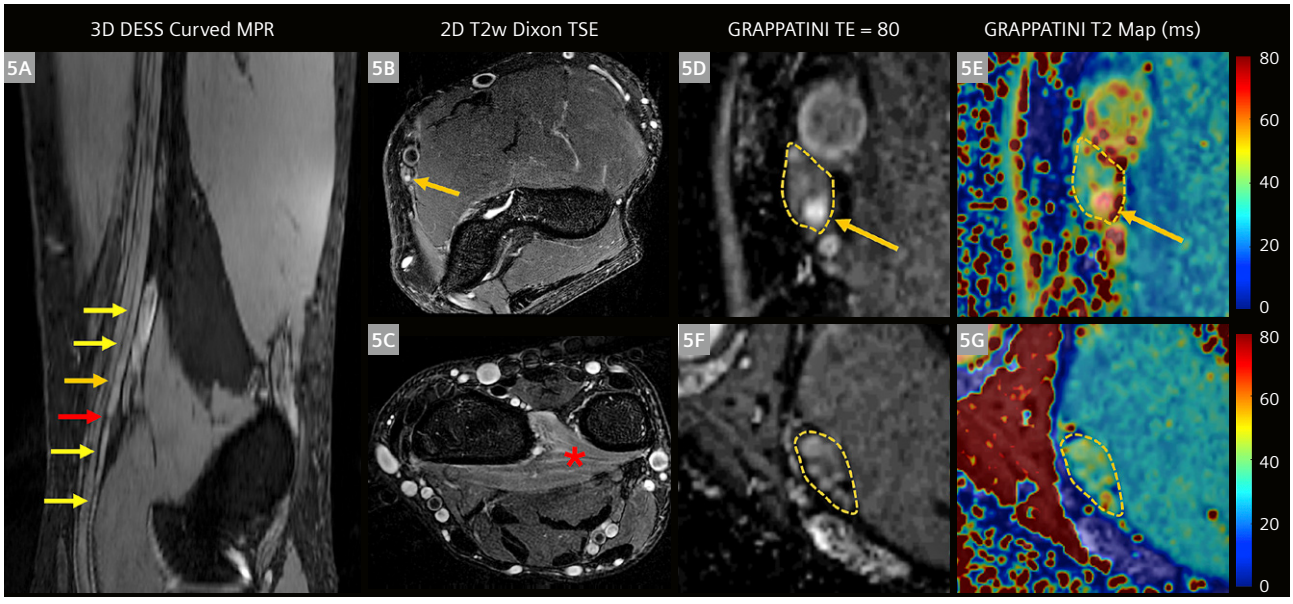

5 Arm and forearm 3T MRI exams (MAGNETOM Vida) in a 33-year-old male subject with left anterior interosseous nerve (AIN) syndrome. **(5A)** Curved maximum projection reconstruction (MPR) from a 3D double echo steady state (DESS) sequence demonstrates enlargement of the AIN bundle of the median nerve (yellow arrows), and a focal constriction (red arrow) characteristic of Parsonage-Turner syndrome and resulting in denervation of the pronator quadratus muscle (**5C**, red *). **(5B)** Axial T2-weighted, fat-suppressed imaging proximal to the constriction (corresponding to the orange arrow location on 5A) demonstrates hyperintensity of the AIN bundle, seen also with hyperintensity and high T2 in GRAPPATINI **(5D, 5E)**. By comparison, expected signal intensity and T2 values were detected in the asymptomatic, ulnar nerve **(5F, 5G)**.

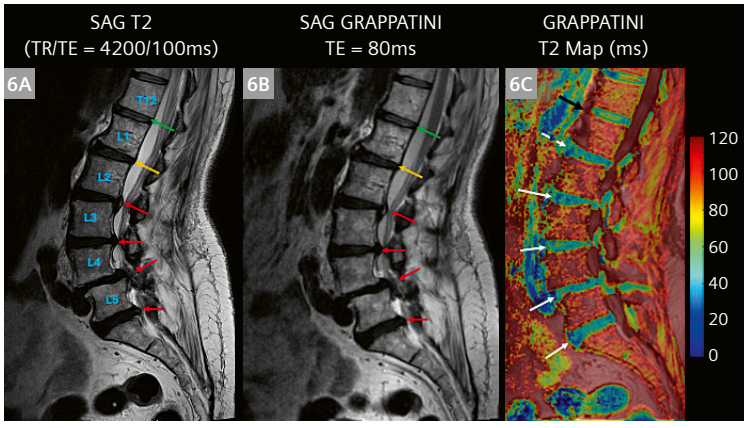

6 Lumbar spine 3T MRI (MAGNETOM Vida) in an 81-year-old female patient with chronic low back pain and claudication who is being considered for spinal fusion and decompression. Sagittal T2 TSE **(6A)** and GRAPPATINI pseudo-TE = 80 ms images **(6B)** demonstrate disc bulges and moderate-to-severe central narrowing from L2–3 to L5–S1 (red arrows), but no disc bulge at T12–L1 (green arrow) or at L1–2 (yellow arrow). Despite the absence of a disc bulge at L1–2, the intervertebral disc at this level demonstrates degeneration, manifest as a low T2 value (T2 = 49.9 ms, dashed arrow) similar to those measured from the L2–3 to L5–S1 discs (T2 = 46.7–50.7 ms, solid white arrows). Compare with the more normal T2 value at T12–L1 (61.9 ms, black arrow) **(6C)**.

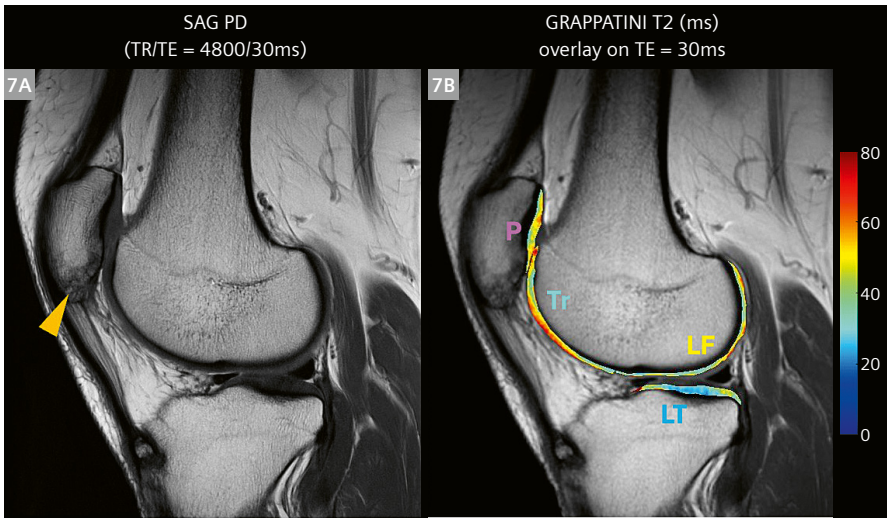

7 MRI at 3T (MAGNETOM Vida) in a 34-year-old female subject with chronic right knee pain demonstrates normal-appearing cartilage on the sagittal proton-density-weighted image **(7A)**. GRAPPATINI demonstrates inhomogeneity and higher mean T2 values of cartilage overlying the patella (P, T2 = 46.3 ms) and trochlea (Tr, T2 = 51.0 ms) **(7B)**, as compared to the lateral tibial and femoral cartilage (LT, LF, T2 = 35.9–42.6 ms), suggesting early chondral degeneration. Enthesopathic changes (yellow arrowhead, 7A), unrelated to chondral wear, are noted at the patellar tendon origin.

Parameter	PD	MapIt	GRAPPATINI
Sequence type	Proton-density-weighted TSE	Standard T2 mapping (multi-echo spin echo)	Model-based accelerated T2 mapping
Scan orientation	Sagittal	Sagittal	Sagittal
TR (ms)	3500–6000	2500	3500
TE (ms)	25–28	10, 20, ..., 80	10, 20, ..., 100
Echo train length	12	8	10
GRAPPA factor	2	2	2
MARTINI factor	–	–	3
Nominal scan time (min)	5:00	5:00	2:30
FOV (cm)	15–19	15–19	15–19
Matrix	512 × 400	336 × 236	336 × 236
Slice thickness (mm)	3.5	4.0	4.0
Readout bandwidth (Hz/pixel)	315	354	354

Table 2: MRI sequence parameters for proton-density-weighted (PD) TSE, MapIt, and GRAPPATINI for 3T knee imaging.

Metric	MapIt	GRAPPATINI	p-value
Mean patellar cartilage T2 (ms)	55.9	51.1	0.48
Mean trochlear cartilage T2 (ms)	71.1	61.8	0.028*
Mean medial femoral cartilage T2 (ms)	65.5	61.7	0.26
Mean medial tibial cartilage T2 (ms)	55.4	60.1	0.65
Mean lateral femoral cartilage T2 (ms)	52.7	51.2	0.65
Mean lateral tibial cartilage T2 (ms)	37.1	42.7	0.13
Scan time (min)	4:10	1:52	< 0.001*

Table 3: T2 values and scan times: MapIt vs. GRAPPATINI in nine knee MRI subjects.

Discussion

GRAPPATINI offers the potential to streamline neuromuscular and orthopedic clinical and research investigations via novel schemes for accelerating T2-mapping acquisition and reconstructions. The dual functionality of T2 mapping and output of synthetic magnitude images for qualitative evaluation is particularly valuable in clinical scenarios otherwise requiring relatively time-intensive, multiplanar, multi-contrast protocols for comprehensive evaluation of a particular condition, and where both qualitative assessment and objective biomarker quantiication may help guide care.

While we observed excellent performance in the examples provided here, further work will be needed to improve GRAPPATINI image reconstruction and to standardize acquisition parameters across anatomical regions and patient populations. This may include a more comprehensive study to determine the quantitative accuracy of GRAPPATINI in various phantom studies, as well as the scan-rescan reproducibility of GRAPPATINI-generated T2 maps. Future studies may explore integration with deep-learning-based reconstruction methods or expand GRAPPATINI to other pulse sequences.

Conclusion

The GRAPPATINI technique represents a valuable addition to the MRI toolbox, enabling fast, efficient, and multiparametric evaluation of musculoskeletal and neuromuscular pathology. We anticipate that ongoing refinement of GRAPPATINI protocols will continue to expand its role in clinical MRI, especially as the demand grows for efficient, quantitative imaging solutions that do not compromise image quality or diagnostic confidence.

Contact

Ek T. Tan, Ph.D.
Co-Director of the MRI Lab
Department of Radiology and Imaging
Hospital for Special Surgery
535 East 70th Street
New York, NY 10021
USA
tane@hss.edu

Darryl B. Sneag, M.D.
Director of MRI Research and
MR Neurography
Department of Radiology and Imaging
Hospital for Special Surgery
535 East 70th Street
New York, NY 10021
USA
sneagd@hss.edu

Acknowledgments

The authors thank Tom Hilbert, Ph.D. and Xiaoying Cai, Ph.D. from Siemens Healthineers for their invaluable technical support.

References

1 Hilbert T, Sumpf TJ, Weiland E, Frahm J, Thiran JP, Meuli R, et al. Accelerated T2 mapping combining parallel MRI and model-based reconstruction: GRAPPATINI. J Magn Reson Imaging. 2018;48(2):359–368.
2 Griswold MA, Jakob PM, Heidemann RM, Nittka M, Jellus V, Wang J, et al. Generalized autocalibrating partially parallel acquisitions (GRAPPA). Magn Reson Med. 2002;47(6):1202–10.
3 Sumpf TJ, Petrovic A, Uecker M, Knoll F, Frahm J. Fast T2 Mapping with Improved Accuracy Using Undersampled Spin-Echo MRI and Model-Based Reconstructions with a Generating Function. IEEE Trans Med Imaging. 2014;33(12):2213–22.
4 Lu AZ, Lin Y, Hilbert T, Igbinoba Z, Shakoor D, Cai X, et al. Feasibility of Qualitative Evaluation and Quantitative T2 Mapping of Peripheral Nerves and Muscles Using GRAPPATINI. J Magn Reson Imaging. 2025. doi: 10.1002/jmri.29803.
5 Bendszus M, Wessig C, Reiners K, Bartsch AJ, Solymosi L, Koltzenberg M. MR imaging in the differential diagnosis of neurogenic foot drop. AJNR Am J Neuroradiol. 2003;24(7):1283–9.
6 Sneag DB, Urban C, Li TY, Colucci PG, Pedrick EG, Nimura CA, et al. Hourglass-like constrictions on MRI are common in electromyography-confirmed cases of neuralgic amyotrophy (Parsonage-Turner syndrome): A tertiary referral center experience. Muscle Nerve. 2024;70(1):42–51.
7 Argentieri EC, Tan ET, Whang JS, Queler SC, Feinberg JH, Lin B, et al. Quantitative T2- mapping magnetic resonance imaging for assessment of muscle motor unit recruitment patterns. Muscle Nerve. 2021;63(5):703–709.
8 Tan ET, Serrano KC, Bhatti P, Pishgar F, Vanderbeek AM, Milani CJ, et al. Quantitative MRI Differentiates Electromyography Severity Grades of Denervated Muscle in Neuropathy of the Brachial Plexus. J Magn Reson Imaging. 2022;56(4):1104–1115.
9 Stefanou DE, Velonakis G, Karavasilis E, Argyropoulos G, Kelekis A, Kelekis N, et al. T2 mapping of lumbar intervertebral disc: quantitative evaluation of degeneration in relation to Pfirrmann grading system and a template for intervertebral disc segmentation. Hippokratia. 2023;27(3):75–81.
10 Eijgenraam SM, Bovendeert FAT, Verschueren J, van Tiel J, Bastiaansen-Jenniskens YM, Wesdorp MA, et al. T2 mapping of the meniscus is a biomarker for early osteoarthritis. Eur Radiol. 2019;29(10):5664–5672.
11 Baum T, Joseph GB, Karampinos DC, Jungmann PM, Link TM, Bauer JS. Cartilage and meniscal T2 relaxation time as non-invasive biomarker for knee osteoarthritis and cartilage repair procedures. Osteoarthritis Cartilage. 2013;21(10):1474–84.

Exploring the Potential of Low-Field Musculoskeletal MRI at 0.55T: Preliminary Results in Patients with Large Metal Implants

Hanns-Christian Breit, M.D.[1]; Jan Vosshenrich, M.D.[1]; Martin Clauss, M.D.[2,3]; Markus M. Obmann, M.D.[1]; Michael Bach, Ph.D.[1]; Dorothee Harder, M.D.[1]; Ricardo Donners, M.D.[1]

[1]Department of Radiology, University Hospital Basel, University of Basel, Switzerland
[2]Center for Musculoskeletal Infections, University Hospital Basel, University of Basel, Switzerland
[3]Department for Orthopedics and Trauma Surgery, University Hospital Basel, University of Basel, Switzerland

Introduction

Low-field MRI scanners are currently experiencing a renaissance, thanks to technical innovations in gradient construction, coil design, and AI-based reconstruction methods [1]. Advantages over the 1.5T and 3T scanners used predominantly in clinical routine include lower acquisition and maintenance costs, and higher patient comfort [2, 3]. Potential advantages of low-field MR imaging include clinical scenarios where imaging using scanners with higher field strengths encounters technical limitations. This is especially the case when imaging patients with metal implants[1] where susceptibility artifacts are expected to be substantially less severe at 0.55T [4, 5]. This may be of particular interest in clinical routine, given an aging global population with an associated higher prevalence of metal implants, e.g., following joint replacement surgery [6]. This patient population has been shown to benefit from MR imaging [7].

The aim of this report is to provide a perspective on the possibilities and potential advantages of using a new-generation 0.55T low-field MRI system in imaging patients with large metal implants.

Materials and methods

Patient population

Three patients underwent complementary MR imaging at 0.55T in addition to their regular clinical imaging work-up.

MRI scanners

Low-field MR imaging was performed using a 0.55T MAGNETOM Free.Max scanner (Siemens Shenzhen Magnetic Resonance Ltd., Shenzhen, China, gradient amplitude 26 mT/m, slew rate 45 T/m/s, 80 cm bore). A six-channel flex coil was used for the examination of the knee and the upper limb.

The 1.5T examinations were performed using a MAGNETOM Avanto Fit system (Siemens Healthcare, Erlangen, Germany, gradient amplitude 45 mT/m, slew rate 200 T/m/s, 60 cm bore). The 3T examinations were performed on a MAGNETOM Skyra system (Siemens Healthcare, Erlangen, Germany, gradient amplitude 45 mT/m, slew rate 200 T/m/s, 70 cm bore).

[1]*The MRI restrictions (if any) of the metal implant must be considered prior to patient undergoing MRI exam. MR imaging of patients with metallic implants brings specific risks. However, certain implants are approved by the governing regulatory bodies to be MR conditionally safe. For such implants, the previously mentioned warning may not be applicable. Please contact the implant manufacturer for the specific conditional information. The conditions for MR safety are the responsibility of the implant manufacturer, not of Siemens Healthineers.*

Case 1

A 59-year-old patient with several prior surgical procedures of the thoracic spine, including multi-level decompression and spinal fusion, presented with back pain refractory to medication. MR imaging of the thoracic spine was requested for the assessment of the spinal canal prior to epidural catheter placement. Routine imaging was performed at 1.5T, followed by a supplemental MR examination at 0.55T.

Due to severe susceptibility artifacts, the spinal canal was not assessable at 1.5T, neither on sagittal or axial T2-weighted sequences, nor on the T1-weighted sequence in the sagittal plane. At 0.55T, visibility and assessability of the spinal canal was substantially improved. Artifact superimposition was only minor, allowing for conclusive evaluation. Contraindications for epidural pain catheter placement could therefore be ruled out at 0.55T. Representative slices from 1.5T and 0.55T imaging are shown in Figures 1 and 2.

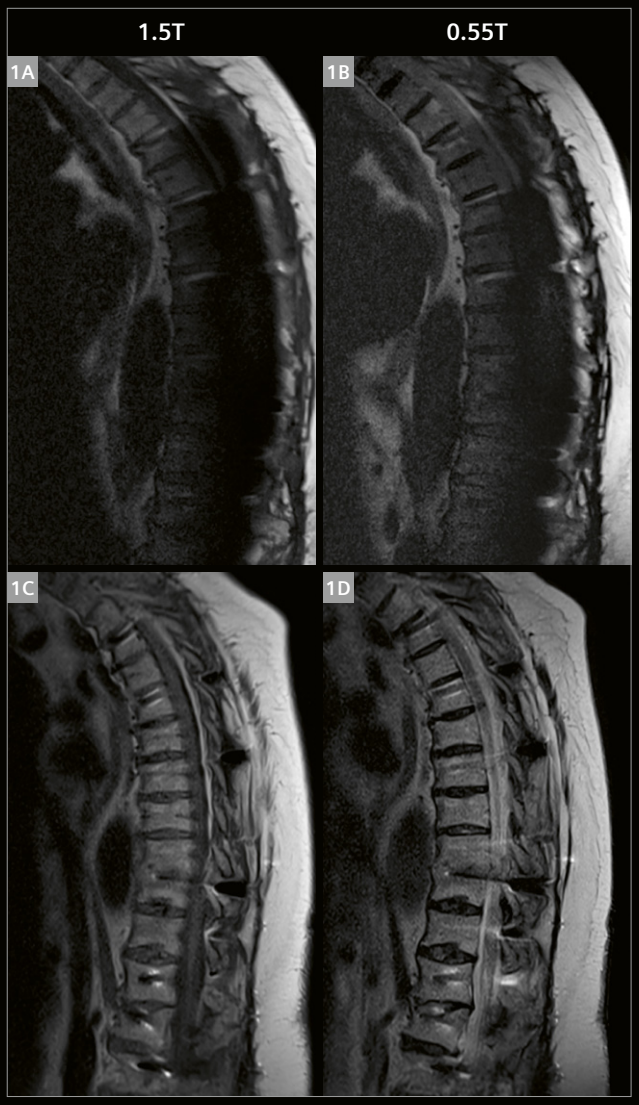

1 Preoperative imaging in a 59-year-old patient with multiple prior surgical procedures of the spine, prior to epidural pain catheter placement. Due to susceptibility artifact superimposition, the spinal canal was not assessable at 1.5T, neither in T2-weighted **(1A)** nor T1-weighted **(1C)** sequences. Artifact severity was substantially lower at 0.55T, allowing for assessment with high diagnostic confidence **(1B, 1D)**.

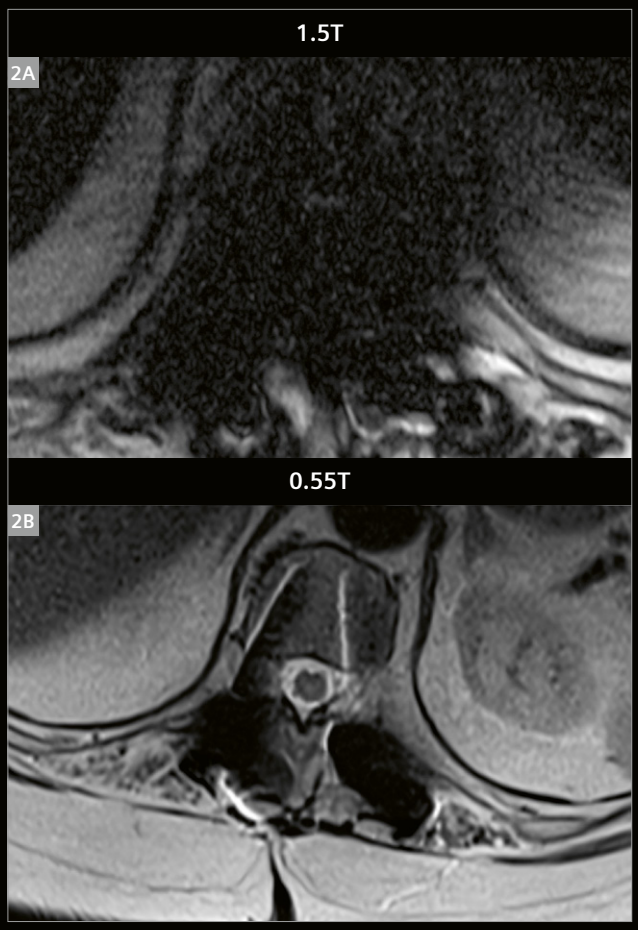

2 Similar to the sagittal images shown in Figure 1, the evaluation of the spinal canal was also only possible using the axial T2-weighted images acquired at 0.55T **(2B)**; while 1.5T did not allow for assessment due to artifact superimposition **(2A)**.

Case 2

A 59-year-old female patient presented with persistent knee pain five years after total knee arthroplasty. Given unremarkable radiographic examinations without signs of loosening, SPECT/CT and supplemental MR imaging at 0.55T were performed.

Radiography did not show signs of implant loosening or other postoperative complications (Fig. 3A). In contrast, MR imaging at 0.55T clearly depicted edema-equivalent signal changes adjacent to the tibial implant component in the lateral tibial plateau, and to a lesser extent also in the medial tibial plateau, indicative of implant loosening. Findings were consistent with the results from SPECT/CT imaging, which showed increased tracer uptake in the aforementioned locations. This was interpreted as implant loosening by a board-certified nuclear medicine physician (Figs. 3B, C).

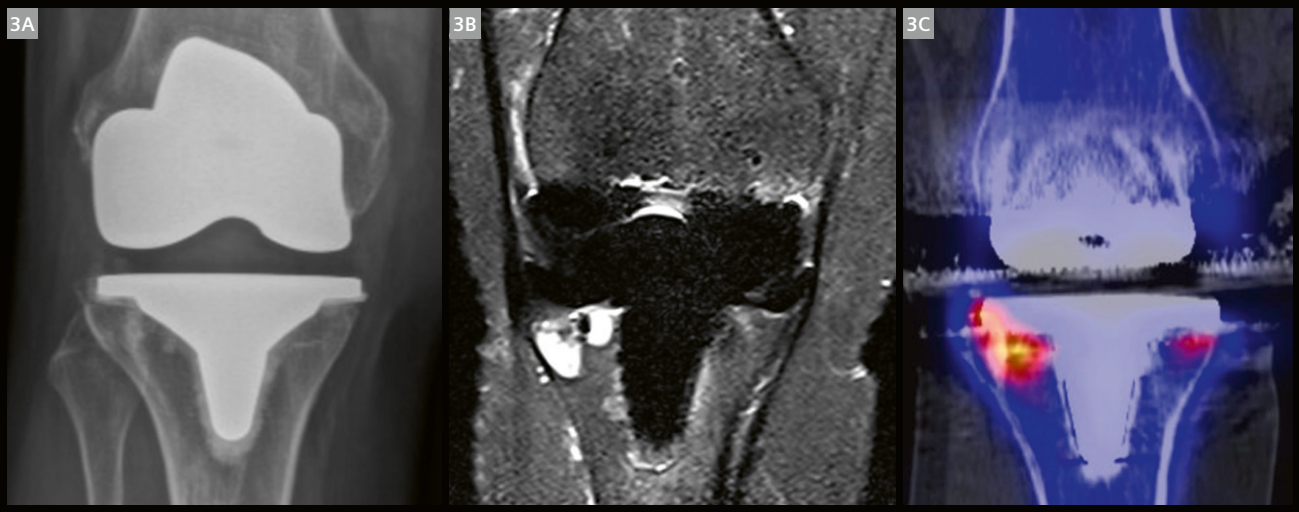

3 A 59-year-old female patient with persistent knee pain five years after total knee replacement. In contrast to conventional radiography **(3A)**, both 0.55T MR imaging **(3B)** and SPECT/CT imaging **(3C)** demonstrated implant loosening of the tibial implant component. The 0.55T MRI also allowed for assessment of ligamentous structures around the knee.

Case 3

A 39-year-old patient presented for routine follow-up imaging after resection of an osteosarcoma of the proximal left humerus and placement of a tumor prosthesis two years ago. Preoperative imaging was first performed at 3T. Follow-up imaging after surgery was performed at 1.5T and 0.55T.

The patient underwent regular postoperative follow-up imaging at 1.5T and supplemental imaging at 0.55T following osteosarcoma resection and tumor prosthesis implantation in the proximal left humerus. Preoperative imaging was performed at 3T (Figs. 4A, B). Comparing the follow-up MRI examinations, especially the soft tissues immediately adjacent to the tumor prosthesis shaft can be delineated clearly better at 0.55T (Fig. 3D) than at 1.5T (Fig. 3C) in the axial T2-weighted fat-suppressed sequences. In the scenario of patients undergoing follow-up imaging after bone tumor resection, potential local tumor recurrence close to the stem can be diagnosed or ruled out with greater confidence at low-field MRI, thanks to better delineation of adjacent structures due to fewer susceptibility artifacts.

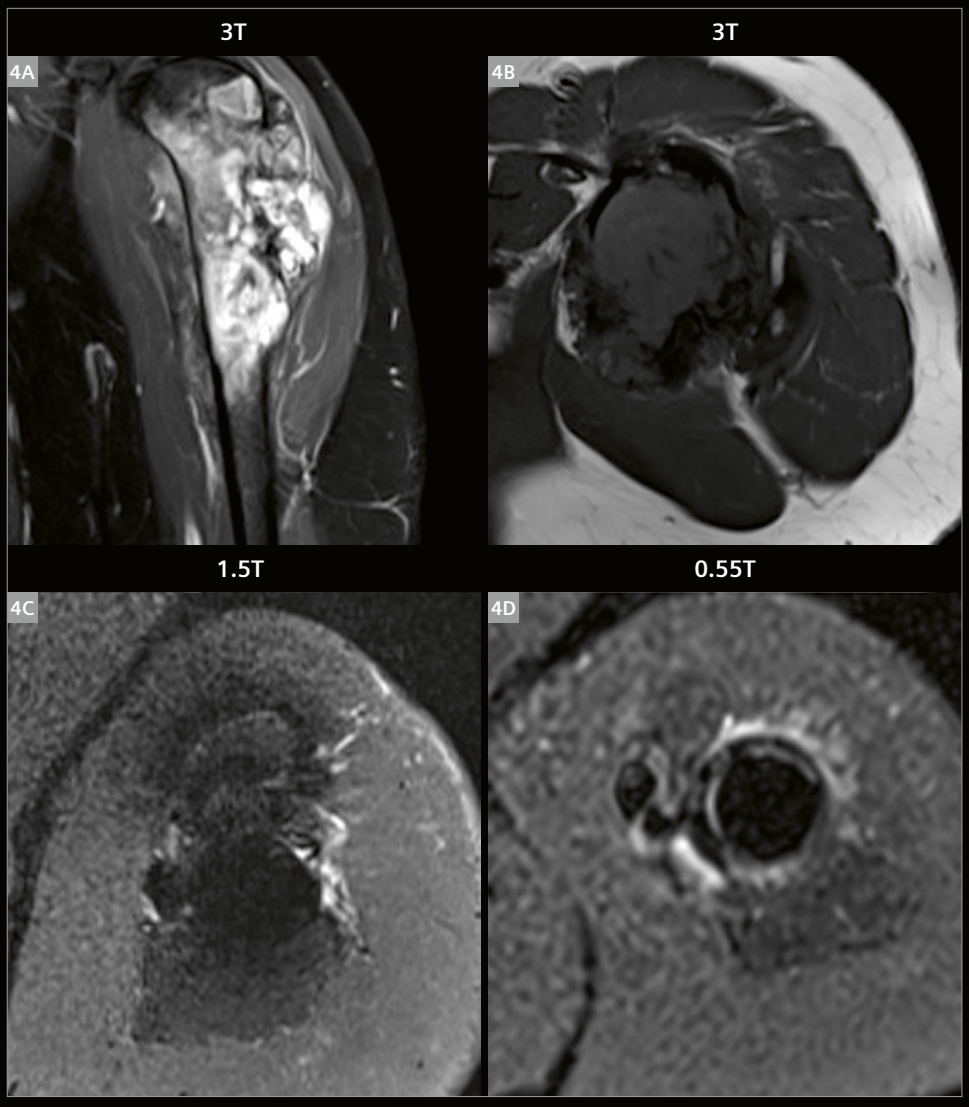

4 A 39-year-old patient who was diagnosed with osteosarcoma of the proximal humerus at 3T **(4A, 4B)**. Following tumor resection and tumor prosthesis implantation, follow-up imaging to assess for local tumor recurrence with axial T2-weighted fat-suppressed sequences is improved at 0.55T **(4D)** compared to 1.5T **(4C)**, with better delineation of the soft tissue structures immediately adjacent to the shaft.

Discussion

In order to achieve the best image quality, the acquisition protocol for handling metal implant imaging must be carefully optimized, regardless of the field strength. In the cases reported here, we employed our optimized clinical protocols for all field strengths used for the image acquisitions. Certain protocol features could contribute to more robust acquisition despite of the metal, while others can correct the resulting artifacts. Metal artifact correction methods, however, are often SAR intensive and result in longer acquisition times. By imaging at 0.55T one can also reduce the concern associated with increased SAR, while often being able to get good clinical results by employing a high-bandwidth protocol.

This brief case series emphasizes the potential of low-field MR imaging at 0.55T in patients with large metal implants. This is in accordance with recently published literature that outlines, for example, the advantages of low-field MR imaging over imaging at higher field strengths in patients with total hip arthroplasty [8]. Our initial experiences as demonstrated in this case series also suggest diagnostic benefits of 0.55T MR imaging in patient groups with other types of large metal implants, such as extensive thoracic or thoracolumbar spondylodesis. Reducing metal-implant-related susceptibility artifacts allows for improved assessment of structures and soft tissues immediately adjacent to the implants, which is of particular importance for detecting local recurrence following tumor resections. Additionally, low-field MR imaging may be helpful in the detection of implant loosening and could complement SPECT/CT imaging by providing details on soft-tissue structures around the knee prior to revising total knee replacements.

In conclusion, it appears to be worth conducting dedicated studies to asses potential applications and opportunities in metal implant imaging – especially in cases of large metal implants – to establish a role for 0.55T low-field MR imaging in clinical routine.

References

1 Runge VM, Heverhagen JT. Advocating the Development of Next-Generation, Advanced-Design Low-Field Magnetic Resonance Systems. Invest Radiol. 2020;55(12):747–753.
2 Vosshenrich J, Breit HC, Bach M, Merkle EM. Ökonomische Aspekte der Niederfeld-Magnetresonanztomographie : Anschaffung, Installation und Unterhaltskosten von 0,55 T-Geräten [Economic aspects of low-field magnetic resonance imaging: Acquisition, installation, and maintenance costs of 0.55 T systems]. Radiologe. 2022;62(5):400–404. German. Epub Mar 29
3 Rusche T, Vosshenrich J, Winkel DJ, Donners R, Segeroth M, Bach M, et al. More Space, Less Noise—New-generation Low-Field Magnetic Resonance Imaging Systems Can Improve Patient Comfort: A Prospective 0.55 T–1.5 T-Scanner Comparison. J Clin Med. 2022;11(22):6705.
4 Farahani K, Sinha U, Sinha S, Chiu LC, Lufkin RB. Effect of field strength on susceptibility artifacts in magnetic resonance imaging. Comput Med Imaging Graph. 1990;14(6):409–413.
5 Bernstein MA, Huston III J, Ward HA. Imaging artifacts at 3.0T. J Magn Reson Imaging. 2006;24(4):735–746.
6 Abdelaal MS, Restrepo C, Sharkey PF. Global Perspectives on Arthroplasty of Hip and Knee Joints. Orthop Clin North Am. 2020;51(2):169–176.
7 Jungmann PM, Agten CA, Pfirrmann CW, Sutter R. Advances in MRI around metal. J Magn Reson Imaging. 2017;46(4):972–991.
8 Khodarahmi I, Brinkmann IM, Lin DJ, Bruno M, Johnson PM, Knoll F, et al. New-generation low-field magnetic resonance imaging of hip arthroplasty implants using slice encoding for metal artifact correction: first in vitro experience at 0.55 T and comparison with 1.5 T. Invest Radiol. 2022;57(8):517–526.

Contact

Hanns-Christian Breit, M.D.
University Hospital Basel
Department of Radiology
Spitalstrasse 21
4031 Basel
Switzerland
Tel.: +41 61 328 56 33
hanns-christian.breit@usb.ch

StarVIBE for Bone Imaging

Eddie Song BS, RT(R)(MR)(MRSO)

Clinical Education Specialist at Siemens Healthineers, Durham, NC, USA

Abstract

Three-dimensional bony morphology assessment is an important part of diagnostic imaging. Computed tomography (CT) has been a leading modality in this field due to its high resolution and relatively fast scan times. However, CT imaging comes at the cost of ionizing radiation, which may not be an option for some patients. Magnetic resonance imaging (MRI) is another modality of choice and is free of ionizing radiation. However, bone morphology is not depicted in as much detail as in CT imaging, due to the extremely short T2 relaxation times [1]. Recently, ultra-short-TE and zero-TE sequences have begun to fill this gap. However, these sequences may not be readily available at all facilities. When choices are limited, another option for 3D bone imaging is the StarVIBE sequence.

Benefits of StarVIBE

StarVIBE is a sequence primarily designed for free-breathing body and pediatric imaging [2]. However, it also has several benefits in 3D bone imaging. Although StarVIBE does not have the very short echo times (TEs) of ultra-short-TE and zero-TE sequences, its repetition time (TR) and TE are still relatively short compared to other pulse sequences. This characteristic of volume interpolated breath-hold examination (VIBE) makes it a suitable candidate for 3D bone imaging. According to several studies, when compared to CT imaging, 3D MRI with VIBE in lumbar imaging showed fracture sensitivity, specificity, and accuracy of 97.7%, 92.3%, and 95.7%, respectively [1].

StarVIBE is robust against motion due to its stack-of-stars trajectory [1]. StarVIBE is a modified version of VIBE that uses radial sampling for in-plane imaging, and Cartesian sampling for through-plane imaging. The center of *k*-space is sampled multiple times due to the radial trajectory, making StarVIBE relatively motion-insensitive. Certain situations and body parts can benefit from motion-insensitive imaging, where StarVIBE becomes advantageous. Additionally, the radial trajectory of StarVIBE requires no phase oversampling, as a radial readout gradient is used inplane. This makes StarVIBE appealing for imaging any body part without aliasing artifacts. However, dedicated protocol modifications are necessary to optimize it for bone imaging.

Modifications for bone imaging

There are several protocols for StarVIBE within the software package from Siemens Healthineers, if availalbe. It is easier to begin with the version that has a smaller field of view and thinner slice thickness. Selecting StarVIBE under the head region is a good starting point (Fig. 1). It already has a 1.5 mm slice thickness and a 0.9 × 0.9 mm pixel dimension.

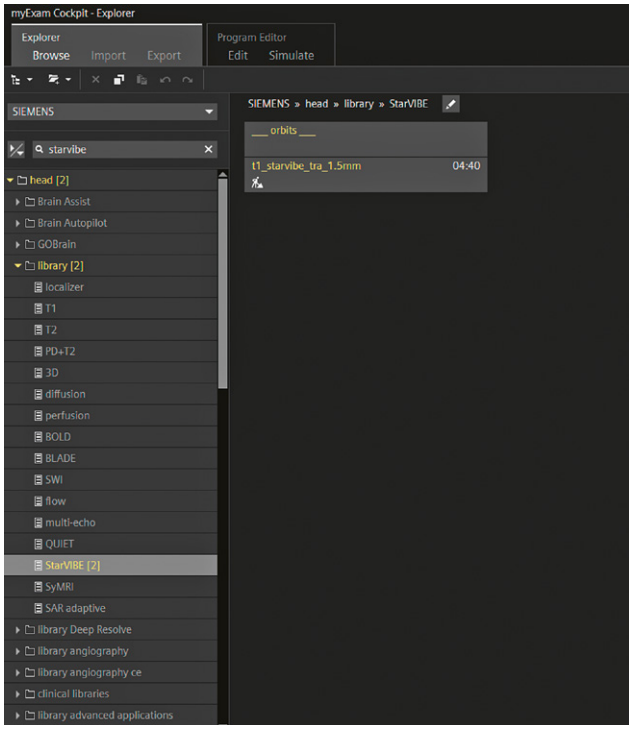

1 StarVibe sequence in the protocol tree from Siemens Healthineers.

The first modification is to turn off the fat saturation pulse and reduce the flip angle to 3° for 1.5T field strengths, and 2° for 3T field strengths (Fig. 2).

The sequence also needs to be optimized to achieve the shortest in-phase TE based on magnetic field strength. The shortest in-phase TE can be entered manually, or automatically selected by choosing the In Phase option under Part 1 of the Sequence tab (Fig. 3).

The shortest in-phase TEs are close to 4.7 ms on 1.5T scanners from Siemens Healthineers, and 2.4 ms on 3T scanners from Siemens Healthineers. Changes to the flip angle and TE help minimize T1 differences between soft tissue, chemical misregistration, and T2 signal loss, while maintaining optimal bone contrast [1]. The higher magnetic field strength of 3T allows for a smaller flip angle, reducing T1 soft tissue contrast due to its innately higher signal intensity.

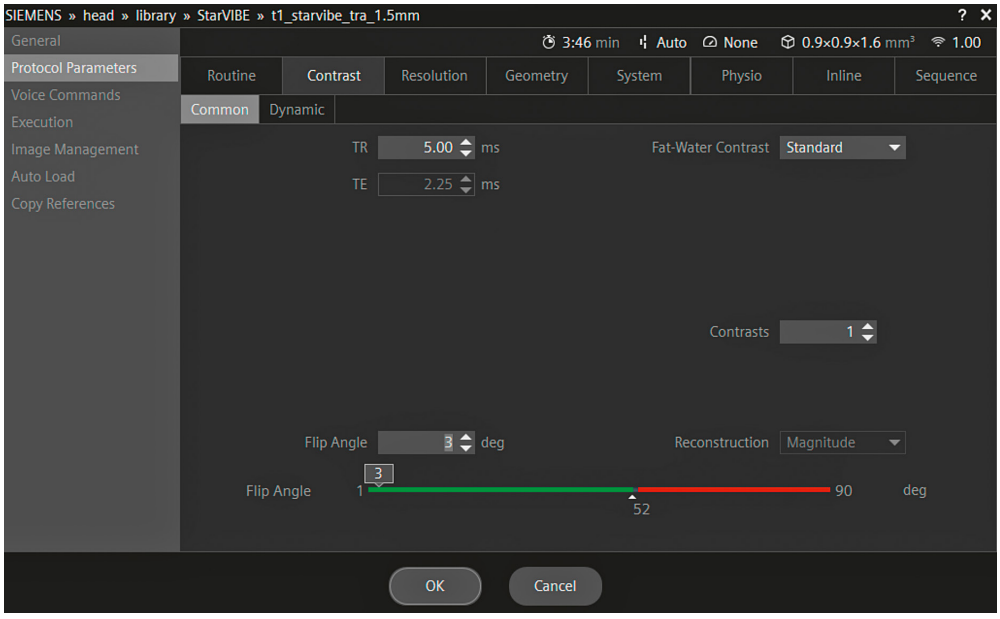

2 Turning off the fat saturation pulse and reducing the flip angle.

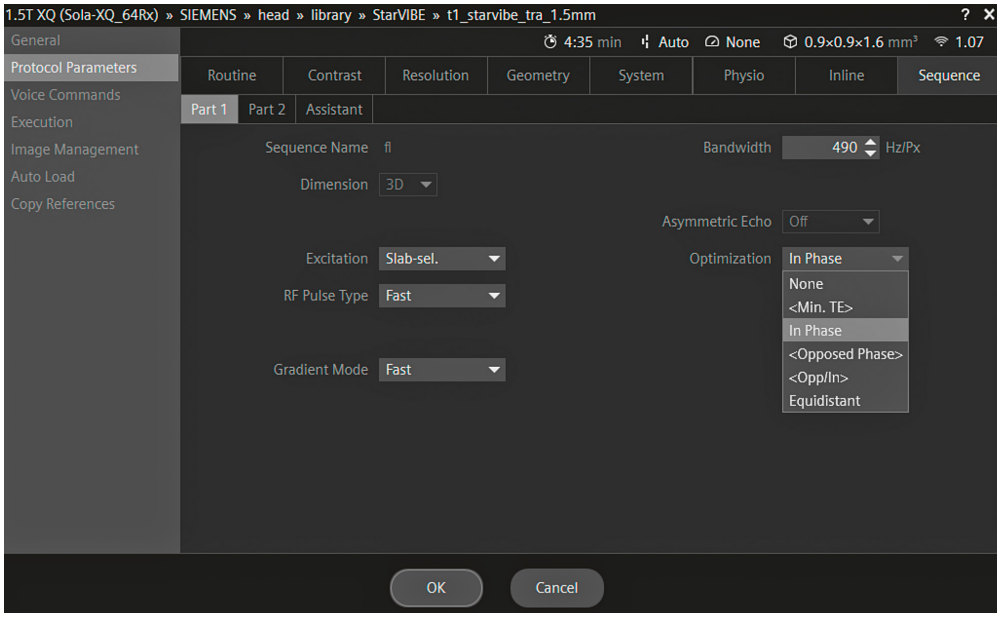

3 Selecting the In Phase option under Part 1 of the Sequence tab.

Ideally, the image should be isotropic to enable optimal reconstruction in any plane after the scan. Due to signal-to-noise-ratio limitations, a 1 × 1 × 1 mm voxel size is a good target for 1.5T. For 3T, it may be possible to reduce the voxel size to 0.8 × 0.8 × 0.8 mm. During this adjustment, the field of view may be limited. If the field of view needs to be reduced, the base matrix may need to be decreased first, due to gradient limitations. Slice resolution can be set to 75%–80% to interpolate and save scan time. Slice thickness should be adjusted to maintain an isotropic voxel size. If the user interface does not allow the desired thinner slice thickness, this can be solved by increasing the number of slices per slab to cover the body part of interest. An increase in slices should provide extra signal in 3D volume acquisition; however, the scan time may increase due to additional slice acquisition. Longer scan times can be balanced by decreasing the average to one. Once the desired voxel size is achieved, radial views should be optimized.

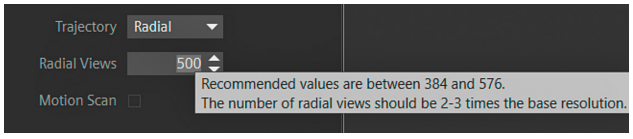

4 Recommended values for the number of radial spokes are displayed on the tooltip when you hover over the Radial Views parameter.

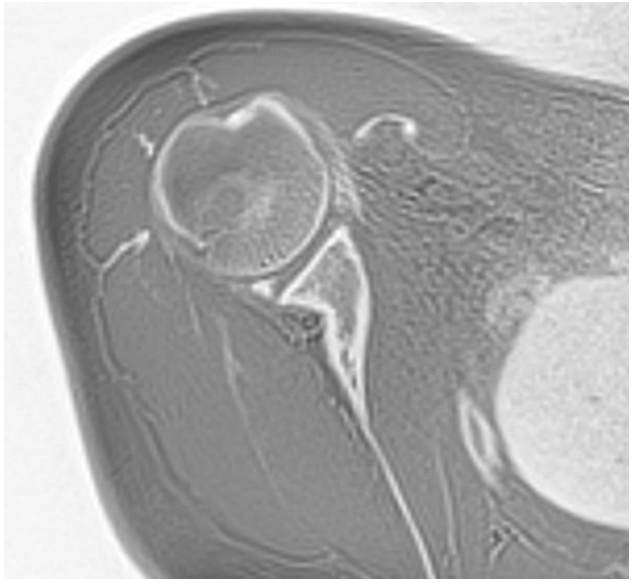

5 Modified StarVIBE for the bone imaging of a shoulder with inverted greyscale.

Radial views determine how many radial spokes are used in the radial sampling scheme of StarVIBE [2]. Recommended values for the number of radial spokes are displayed on the tooltip when you hover over the Radial Views parameter (Fig. 4). The range of recommended values can change depending on what base resolution is set. An optimal number of radial spokes allows for proper overlap in the center of *k*-space, thereby reducing motion artifacts. The correct radial views can also reduce streak artifacts. Therefore, bone imaging in motion-prone body regions may require a higher number of radial views than in relatively stationary body regions. Scan time is another factor to consider, as more radial views will require longer scan times.

Once the image is acquired, the grayscale can be inverted in View&GO by pressing F10 on the keyboard. Alternatively, radiologists can easily invert it from the PAC. This grayscale inversion provides a CT-like 3D bone imaging appearance (Figs. 5 and 6). The isotropic acquisition of StarVIBE bone imaging should allow the user to reconstruct it in any plane to evaluate the region of interest.

6 Modified StarVIBE for the bone imaging of an ankle with inverted greyscale.

Conclusion

MRI is a safe way to evaluate bone morphology. The isometric StarVIBE low TE sequence was designed to enhance osseous cortical and trabecular detail.

Like CT, it allows for a single sequence to be reformatted into multiple planes. This sequence offers numerous potential clinical applications, particularly in cases where a CT scan would traditionally be required alongside an MRI. Proper modification of StarVIBE enables flexible, optimal, and sensitive bone imaging.

References

1 Chong LR, Lee K, Sim FY. 3D MRI with CT-like bone contrast – An overview of current approaches and practical clinical implementation. Eur J Radiol. 2021;143:109915.
2 Chandarana H, Block TK, Rosenkrantz AB, Lim RP, Kim D, Mossa DJ, et al. Free-Breathing radial 3D Fat-Suppressed T1-Weighted gradient echo sequence: a viable alternative for contrast-enhanced liver imaging in patients unable to suspend respiration. Invest Radiol. [Internet]. 2011;46(10):648–53.

Contact

Eddie Song BS, RT(R)(MR)(MRSO)
Clinical Education Specialist
at Siemens Healthineers
109 Tuftin Drive
Durham, NC 27703
USA
eddie.song@siemens-healthineers.com

Pictorial Essay: Clinical Application of StarVIBE for Bone Imaging

Erin Moran, M.D.

Associate Professor of Radiology, Duke University, Durham, NC, USA

Over the last decade, the attempt to produce MR images that provide bony detail comparable to CT has resulted in multiple different techniques including various VIBE sequences, UTE/ZTE sequences, and synthetic CT. The StarVIBE sequence for bone imaging shares many of the benefits of those techniques. It is isometric and provides high-resolution images that are reformattable. The images also provide excellent cortical and trabecular detail in bony structures, as well as excellent visualization of soft tissue mineralization. The sequence also stands up well when dealing with metal[1] artifact and is comparable to metal reduction sequences in its ability to reduce metal artifact. Additionally, there is no loss of signal when relevant anatomy is distant from the isocenter, which is particularly useful when imaging joints such as the shoulder and the hip.

These images provide some examples of our initial experience using this sequence at Duke.

[1] *The MRI restrictions (if any) of the metal implant must be considered prior to patient undergoing MRI exam. MR imaging of patients with metallic implants brings specific risks. However, certain implants are approved by the governing regulatory bodies to be MR conditionally safe. For such implants, the previously mentioned warning may not be applicable. Please contact the implant manufacturer for the specific conditional information. The conditions for MR safety are the responsibility of the implant manufacturer, not of Siemens Healthineers.*

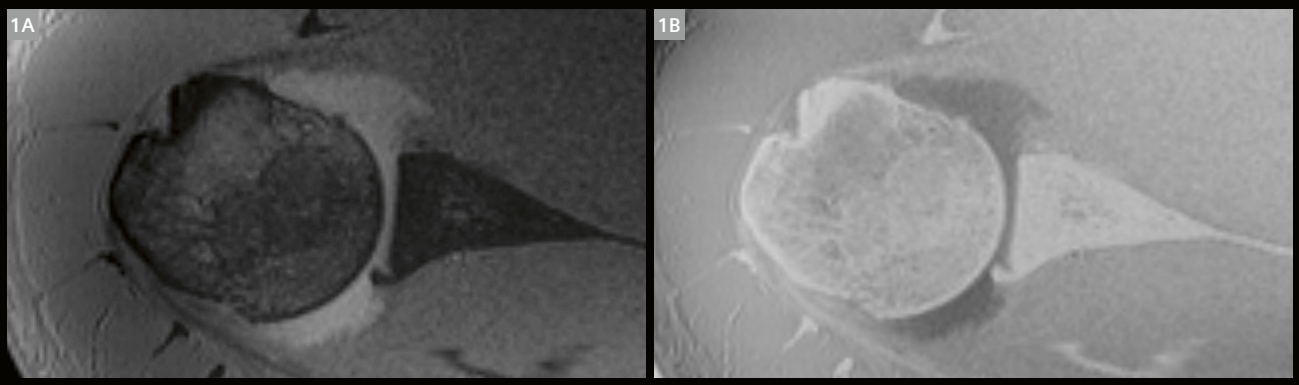

1 A modified StarVIBE axial sequence from an MR arthrogram in the original **(1A)** and in the inverted **(1B)** form shows bone loss in the anterior glenoid in a patient with recurrent dislocations.

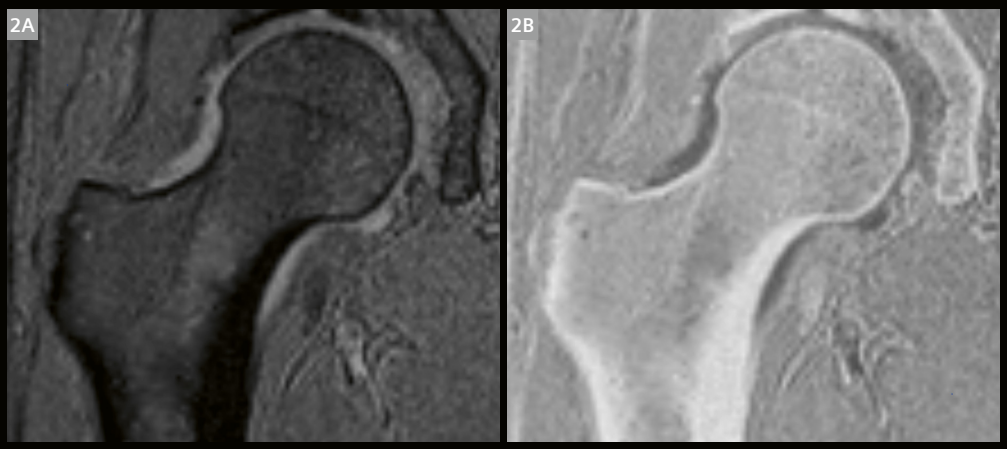

2 A modified StarVIBE coronal sequence from a hip arthrogram in a patient with prior surgery shows the post-surgical changes to the bone following a femoral osteochondroplasty.

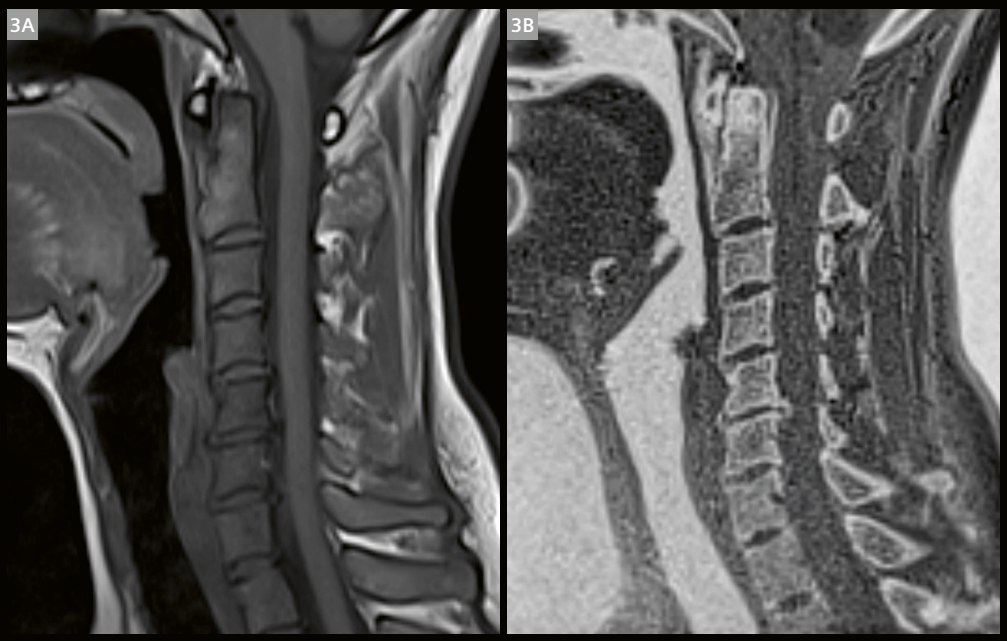

3 A modified StarVIBE sagittal sequence and sagittal T1 TSE. The posterior osteophytes at the level of C5–C6 are more clearly visualized on the StarVIBE sequence.

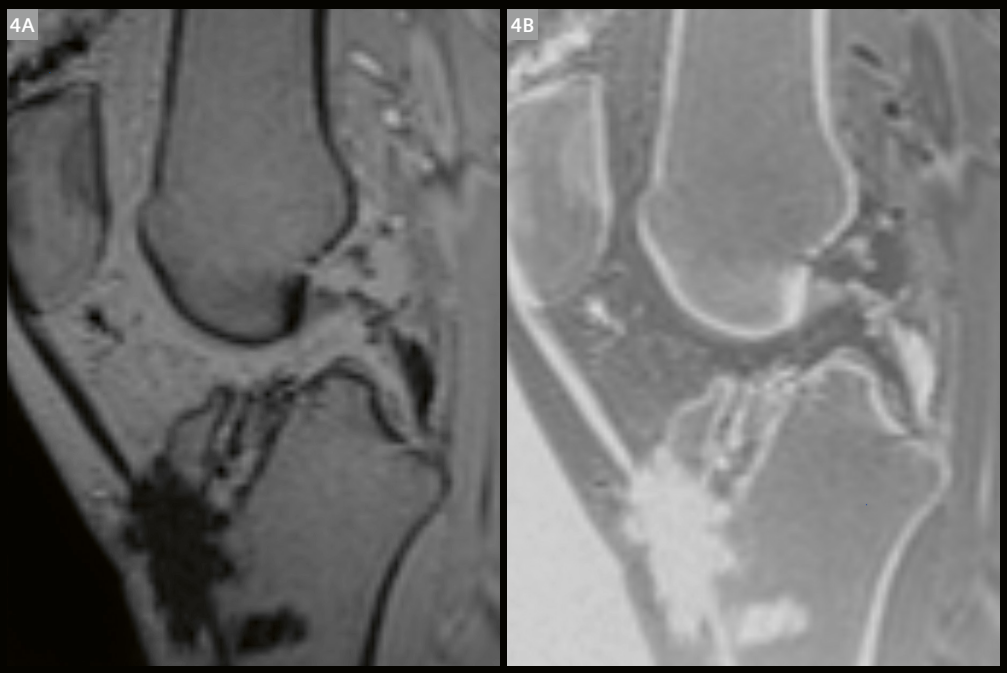

4 Modified StarVIBE sagittal images in a patient with a prior ACL reconstruction. The sequence delineates the bony detail of the tibial tunnel on par with CT in preoperative assessment for revision ACL reconstruction.

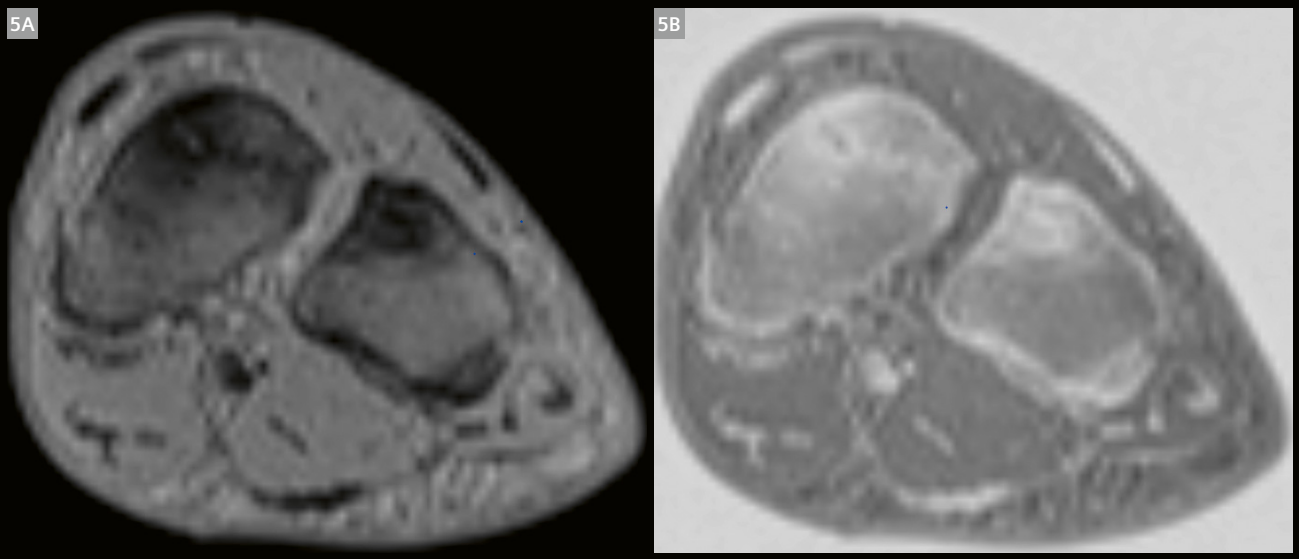

5 A modified StarVIBE coronal image from a midfoot MRI in a patient with suspected navicular stress reaction. On STIR sequences (not shown), bone marrow edema was present throughout the navicular, consistent with stress reaction. On the StarVIBE coronal sequence, linear signal is present within the navicular, consistent with a developing stress fracture.

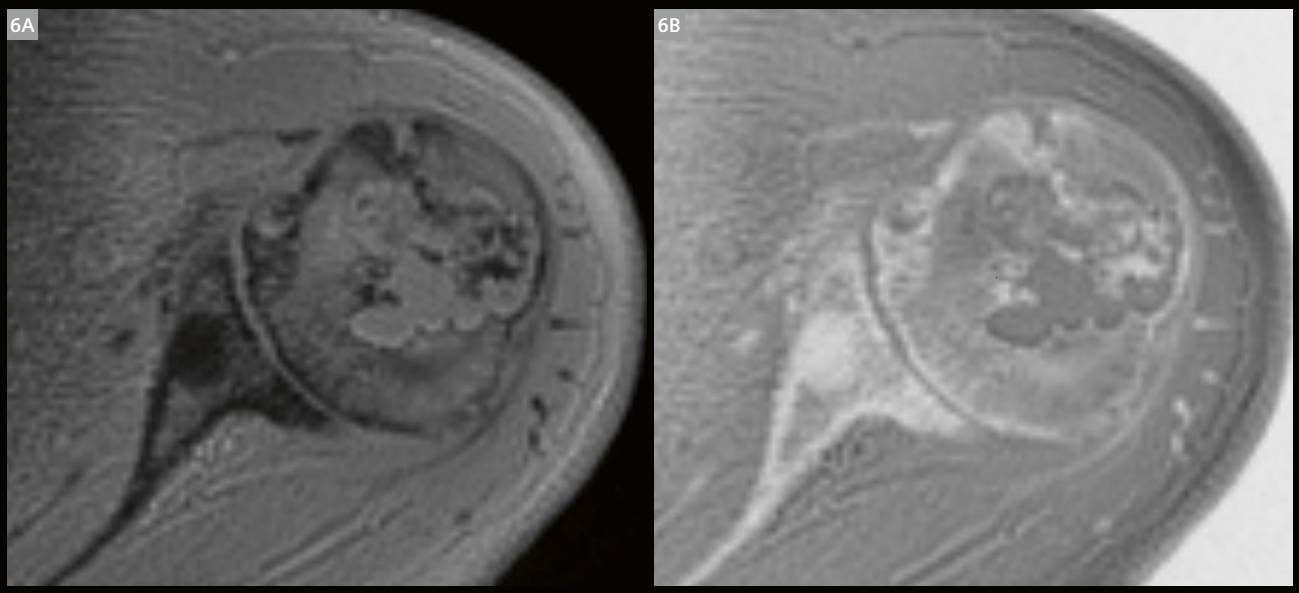

6 A modified StarVIBE axial image of the left shoulder in a patient with a chondroid lesion in the humeral head. The margins of the lesions, as well as the chondroid mineralization, are clearly delineated.

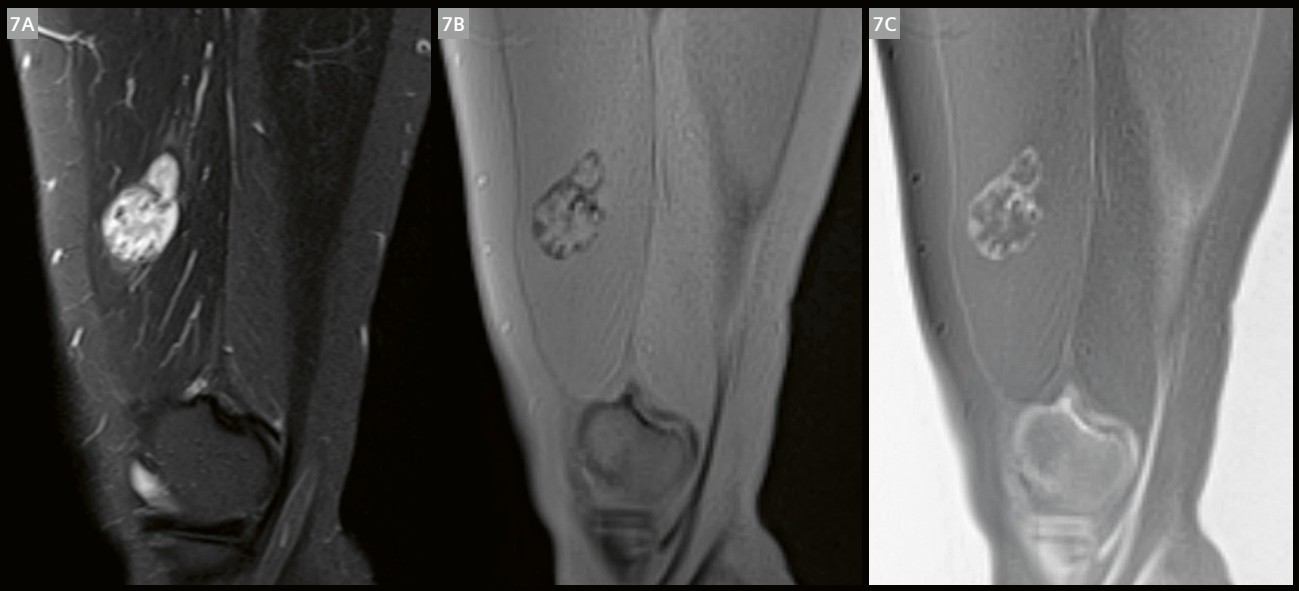

7 A sagittal STIR image and StarVIBE sagittal images of the right thigh in a patient with myositis ossificans. The peripheral rim of mineralization demonstrated on the modified StarVIBE sequences allows the diagnosis to be made on the MRI without the need for additional imaging.

Contact

Erin Moran, M.D.
Associate Professor of Radiology,
Duke University
Box 3808 DUMC
Durham, NC 27710
USA
Tel.: +1 (919) 684-2711
erin.moran@duke.edu

Meet Siemens Healthineers

Siemens Healthineers: Our brand name embodies the pioneering spirit and engineering expertise that is unique in the healthcare industry. The people working for Siemens Healthineers are totally committed to the company they work for, and are passionate about their technology. In this section we introduce you to colleagues from all over the world – people who put their hearts into what they do.

Corinna Berkel

My story begins in West Berlin, where the Berlin Wall served as a daily reminder of what it means to live with limits – and the importance of moving beyond them. That mindset carried into my career, which I began as a radiology technologist at the Charité in Berlin, and progressed through roles in clinical practice and software applications. In 2011, I joined Siemens Healthineers as an MR applications specialist, later relocating to Singapore to support MR imaging across the ASEAN region. Today, as global clinical marketing manager for musculoskeletal imaging, I help to bring our imaging solutions to users and patients around the world.

How did you first come into contact with MRI?
I first came into contact with MRI during my time as a CT technologist in a private radiology practice. When they installed a MAGENTOM scanner, I was curious but didn't realize how impactful it would be. As I observed the scans and learned about the technology, I became fascinated by its ability to provide detailed images in different planes and tissue contrasts. It opened up a whole new world of diagnostic possibilities. That initial fascination quickly evolved into a strong professional passion, and from that point on, I knew MRI was where I wanted to focus my energy and grow my skills.

What do you find motivating about your job?
MR is constantly evolving, and right now we're at a particularly exciting point with breakthroughs in AI, deep learning, and quantification. I see my role as bridging the gap between advanced technology and everyday clinical needs. What motivates me is helping to turn our developments into something truly relevant and beneficial for the daily work of healthcare providers: Whether it's better image quality or more streamlined workflows, that's when innovation really makes an impact.

What are the biggest challenges in your job?
We work in a dynamic environment where success depends on thoughtful planning, collaboration, and the ability to adapt quickly. Aligning multiple priorities and stakeholders takes effort, but it's also where the best ideas emerge. The impact of a marketing campaign may take time to reveal itself, but we always focus our efforts on ensuring that our work leads to meaningful outcomes and creates value for healthcare professionals.

What are the most important developments in healthcare?
From my perspective, one of the most exciting developments in healthcare is the rise of digital technologies. I'm also particularly impressed by how AI is beginning to support more personalized care, from diagnostics to treatment planning. As someone involved in medical imaging, it's inspiring to see how imaging technologies continue to evolve, enabling earlier and more accurate diagnoses. And I think it's equally important that healthcare is starting to look at its environmental footprint: Sustainability efforts are becoming an essential part of how we move forward as an industry.

What would you do if you could spend a month doing whatever you wanted?
If I had a month to do whatever I wanted, I'd focus on learning and discovery. I've always wanted to learn to play the piano, so I'd finally dedicate time to that. I also love traveling and exploring new places – Australia, for instance, is still on my list. I'd love to visit and experience the unique culture, the culinary scene, and the incredible nature.

Gregor Körzdörfer, Ph.D.

Born and raised in Erlangen, Germany, Gregor Körzdörfer pursued studies in physics at Friedrich-Alexander-Universität Erlangen-Nürnberg (FAU). His master's thesis, which focused on developing tools for sequence development and optimization, marked the beginning of his deep involvement in MRI. Gregor continued his education with a Ph.D. at FAU, working on MR fingerprinting in close collaboration with Siemens Healthineers. He then became an Application Developer in the predevelopment team, before transitioning to the role of Scientific Collaboration Manager for MRI in New York, USA. Upon returning, he reconnected with his roots in MRI and became head of the musculoskeletal predevelopment team.

How did you first come into contact with MRI?
I feel fortunate to have never needed an MRI myself so far. However, growing up in Germany and following sports such as soccer, I often heard about players needing MRIs to assess their injuries. Additionally, seeing teammates and friends get injured brought MRI further into my awareness. My first direct encounter with MRI was when I accompanied my little sister to her MRI exam while I was studying physics. At that time, I couldn't explain the process to her accurately, but the experience piqued my interest. Later, when I started working as a student in the MR predevelopment department at Siemens Healthineers, I became completely hooked on the technology and its potential. The field of MRI research offers a lot of freedom to try new things and think creatively, all while making a significant impact.

What do you find motivating about your job?
My job is motivating because it has a clear purpose. Everything we do, in collaboration with our technical and clinical partners, advances medicine. The opportunity to make a tangible difference in healthcare drives me every day. I am passionate about developing new technologies and methods that improve diagnostic accuracy and enable more efficient patient care. Working with a team of talented and passionate colleagues from diverse backgrounds around the globe constantly inspires me to push the boundaries of what is possible in medical imaging. Knowing that our work can lead to faster, better diagnoses and treatments for patients, while also making radiology more efficient, is incredibly fulfilling.

What are the biggest challenges in your job?
One of the biggest challenges in my job is ensuring that we develop reliable solutions that truly benefit clinicians. Aligning the goals of technical advancements with the practical needs of clinicians can be challenging, but it is a crucial aspect of my work. Developing new MRI techniques requires carefully weighing many factors, and the development process involves rigorous testing and validation to ensure that they are useful and effective for radiology departments and practices.

What are the most important developments in healthcare?
In my opinion, one of the most important developments in healthcare is the integration of artificial intelligence with medical imaging. AI has the potential to revolutionize the way diseases are diagnosed and treated by providing faster, more accurate, and more personalized insights. In MRI, AI can enhance image reconstruction, automate complex workflows, and improve diagnostic accuracy. These advancements lead to more efficient and effective patient care and ultimately improve patient outcomes.

What would you do if you could spend a month doing whatever you wanted?
If I could spend a month doing whatever I wanted, I would combine work and leisure by traveling the world. Although a month is a short time, I would hope to visit many interesting places and plan time to stop at hospitals and university research departments. I would love to learn about exciting developments in both technical and clinical areas and gain a deeper understanding of the patient journey and the need for improvements. Traveling to different places and learning about different cultures and perspectives is something I truly enjoy, and it would be fantastic to combine that with a focus on MRI. So far, I have had the pleasure of learning from inspiring people all over the world.

The entire editorial staff at Castlereagh Imaging, Edgecliff, NSW, Australia and at Siemens Healthineers extends their appreciation to all the radiologists, technologists, physicists, experts, and scholars who donate their time and energy – without payment – in order to share their expertise with the readers of MAGNETOM Flash.

MAGNETOM Flash – Imprint

Publisher:
Siemens Healthineers AG
Magnetic Resonance,
Karl-Schall-Str. 6, D-91052 Erlangen, Germany

Editor-in-chief:
Antje Hellwich
antje.hellwich@siemens-healthineers.com

Guest Editor:
Dr James Linklater OAM
MB BS (Hons), B Med Sci, DDU (1), FRANZCR
Musculoskeletal Radiologist and CEO, Castlereagh Imaging and Illawarra Radiology Group, Australia

Editorial Board:
Kera Westphal, Ph.D.; Kathrin El Nemer, M.D.; Wellesley Were; Katie Grant, Ph.D.; Gregor Körzdörfer, Ph.D.

Review Board:
Corinna Berkel; André Fischer, Ph.D.; Daniel Fischer; Christian Schuster, Ph.D.; Aurélien Stalder, Ph.D.; Gregor Thörmer, Ph.D.

Copy Editing:
Sheila Regan, Jen Metcalf, UNIWORKS,
www.uni-works.org
(with special thanks to Kylie Martin)

Layout:
Agentur Baumgärtner,
Friedrichstr. 4, D-90762 Fürth, Germany,
www.agentur-baumgaertner.com

PrePress and Image Editing, Production:
Clemens Ulrich, Paul Linssen,
Siemens Healthineers AG

Printer:
Schmidl & Rotaplan Druck GmbH,
Hofer Str. 1, D-93057 Regensburg, Germany

MAGNETOM Flash includes reports in the English language on magnetic resonance: diagnostic and therapeutic methods and their application as well as results and experience gained with corresponding systems and solutions. It introduces from case to case new principles and procedures and discusses their clinical potential. The statements and views of the authors in the individual contributions do not necessarily reflect the opinion of the publisher.

The information presented in these articles and case reports is for illustration only and is not intended to be relied upon by the reader for instruction as to the practice of medicine. Any health care practitioner reading this information is reminded that they must use their own learning, training and expertise in dealing with their individual patients. This material does not substitute for that duty and is not intended by Siemens Healthcare to be used for any purpose in that regard. The drugs and doses mentioned herein are consistent with the approval labeling for uses and/or indications of the drug. The treating physician bears the sole responsibility for the diagnosis and treatment of patients, including drugs and doses prescribed in connection with such use. The Operating Instructions must always be strictly followed when operating the MR system. The sources for the technical data are the corresponding data sheets. Results may vary.

We welcome your questions and comments about the editorial content of MAGNETOM Flash. Please contact us at magnetomworld.team@siemens-healthineers.com

Manuscripts as well as suggestions, proposals and information are always welcome; they are carefully examined and submitted to the editorial board for attention. MAGNETOM Flash is not responsible for loss, damage, or any other injury to unsolicited manuscripts or other materials. We reserve the right to edit for clarity, accuracy, and space. Include your name, address, and phone number and send to the editors, address above.

MAGNETOM Flash is also available online:

www.siemens-healthineers.com/magnetom-world

Not for distribution in the US

On account of certain regional limitations of sales rights and service availability, we cannot guarantee that all products included in this brochure are available through the Siemens Healthineers sales organization worldwide. Availability and packaging may vary by country and is subject to change without prior notice. Some/All of the features and products described herein may not be available in the United States.

The information in this document contains general technical descriptions of specifications and options as well as standard and optional features which do not always have to be present in individual cases, and which may not be commercially available in all countries. Due to regulatory reasons their future availability cannot be guaranteed. Please contact your local Siemens organization for further details.

Siemens Healthineers reserves the right to modify the design, packaging, specifications, and options described herein without prior notice. Please contact your local Siemens Healthineers sales representative for the most current information.

Note: Any technical data contained in this document may vary within defined tolerances. Original images always lose a certain amount of detail when reproduced.

Siemens Healthineers Headquarters
Siemens Healthineers AG
Siemensstr. 3
91301 Forchheim, Germany
Phone: +49 9191 180
siemens-healthineers.com

Published by Siemens Healthineers AG · Order No. A91MR-1000-162M-7600 · Printed in Germany · 16229 072025 ·